Master's thesis

Micromachines swimming in viscoelastic fluids

(邦題):粘弾性体中を遊泳するマイクロマシン (英文)

Supervisor: Associate Professor Shigeyuki Komura

Department of Chemistry, Graduate School of Tokyo Metropolitan University

Student ID: 16880336

Name: Kento Yasuda

Date: January 9, 2018

Abstract

Summary of Master Dissertation
(Master Program (Science))

16880336 Kento YASUDA

Micromachines swimming in viscoelastic fluids
（邦題）：粘弾性体中を遊泳するマイクロマシン（英文）

Microswimmers are tiny machines that swim in a fluid, such as sperm cells or motile bacteria, and they are expected to be applied to microfluidics and microsystems. By transforming chemical energy into mechanical work, microswimmers change their shape and move in viscous environments. Over the length scale of microswimmers, the fluid forces acting on them are governed by the effect of viscous dissipation. According to Purcell's scallop theorem, time-reversal body motion cannot be used for locomotion in a Newtonian fluid. As one of the simplest models exhibiting broken time-reversal symmetry, Najafi and Golestanian proposed a three-sphere swimmer, in which three in-line spheres are linked by two arms of varying length.

First, we discuss the locomotion of a three-sphere microswimmer in a viscoelastic medium and propose a new type of active microrheology. We derive a relation that connects the average swimming velocity and the frequency-dependent viscosity of the surrounding medium. In this relation, the viscous contribution can exist only when the time-reversal symmetry is broken, whereas the elastic contribution

is present only when the structural symmetry of the swimmer is broken. Purcell's scallop theorem breaks down for a three-sphere swimmer in a viscoelastic medium.

Next, we discuss the dynamics of a generalized three-sphere microswimmer in which the spheres are connected by two elastic springs. The natural length of each spring is assumed to undergo a prescribed cyclic change. We analytically obtain the average swimming velocity as a function of the frequency of cyclic change in the natural length. In the low-frequency region, the swimming velocity increases with frequency, and its expression reduces to that of the original three-sphere model by Najafi and Golestanian. Conversely, in the high-frequency region, the average velocity decreases with increasing frequency. Such behavior originates from the intrinsic spring relaxation dynamics of an elastic swimmer moving in a viscous fluid.

Finally, we discuss the directional motion of an elastic three-sphere micromachine in which the spheres are in equilibrium with independent heat baths having different temperatures. Even in the absence of prescribed motion of the springs, such a micromachine can gain a net motion due purely to thermal fluctuations. A relation connecting the average velocity and the temperatures of the spheres is analytically obtained. This velocity can also be expressed in terms of average heat flows in the steady state. Our model suggests a new mechanism for locomotion of micromachines in nonequilibrium biological systems.

Contents

iii

Chapter 1

Introduction

1.1 Quantitative understanding of non-equilibrium phenomena

Many physical phenomena are investigated by using methods of equilibrium statistical physics. Equilibrium statistical physics, however, cannot deal with biological phenomena which are governed by non-equilibrium processes. Therefore, the establishment of non-equilibrium statistical physics is an important issue.

Recently, violation of the fluctuation dissipation theorem (FDT) has been used to quantitatively characterize non-equilibrium phenomena. FDT is the relation which connects fluctuations and dissipations in equilibrium systems. It is considered that the violation of FDT can be quantitatively measured in order to characterize non-equilibrium properties. Microrheology (MR) [1.1, 1.2] can be used to observe the FDT violation. MR is one of the most useful techniques for measuring the rheological properties of soft matter. There are two different methods; passive microrheology and active microrheology. In active microrheology, a probe particle in the sample medium is actively pulled in order to measure mechanical responses. In passive microrheology, the mechanical properties of a medium can be extracted from the Brownian motion of probe particle. Because active MR and passive MR are related to dissipation and fluctuation, respectively, we can

estimate the violation of FDT by compering these two quantities.

Living cells have been attracting much interests as typical non-equilibrium systems. In living cells, active proteins generate mechanical energy from chemical energy due to ATP, and biopolymers such as cytoskeletons show complex mechanical responses. Since both aspects of non-equilibrium phenomena and rheology coexist in living cells, they are ideal systems to analyze out-of-equilibrium properties with the use of MR. An experiment using MR in living cells or membranes of red blood cells show the breakdown of FDT. Guo *et al.* introduced small particles into cancer cells, and measured mechanical response and self-diffusion [1.3]. As a result, the mean squared displacement (MSD) shows a dependence on ATP concentration. Furthermore, MSD shows anomalous diffusion, which indicates that MSD is not proportional to time. As a result of response and MSD, the breakdown of FDT in living cells has been confirmed and they further estimated the degree of FDT violation. On the other hand, Turlier *et al.* measured response and fluctuations of RBCs [1.4]. As a result, the violation of FDT has been found in the low-frequency regime for RBCs in the presence of ATP.

On the other hand, how to consider non-equilibrium and viscoelastic effects in the theoretical framework of MR remains to be investigated. My research aim is to quantitively understand non-equilibrium systems such as living cells. In this thesis, I have investigated self-diffusion and membrane fluctuations in non-equilibrium systems [1.5–1.9].

1.2   Non equilibrium behaviors of micromachines

The challenge to estimate non-equilibrium properties of external environment from self-diffusion and membrane fluctuations in living cells has started only recently. Non-equilibrium behaviors of micromachines, which exhibit internal non-equilibrium processes, have attracted much interests. Micromachines correspond to tiny objects which can extract energy from ATP through chemical reactions and make functions by varying their conformations. Examples are enzymes and

motor proteins in living cells or microorganism such as bacteria or sperm.

Recently, it was reported that self diffusion of single molecule enzymes is enhanced by the addition of substrate [1.10–1.12], and this problem has been discussed actively in the community. Several possibilities to explain the diffusion enhancement have been proposed such as thermophoresis, collective heating, stochastic swimming [1.13–1.15]. However this problem has not yet been resolved. Theoretical work to explain the diffusion enhancement is now being intensively discussed, and how to relate non-equilibrium phenomena and self-diffusion of micromachines needs to be investigated in detail. If this relations is established, we can estimate internal non-equilibrium properties from the measurement of the dynamics of micromachines.

Swimming motion is an essential function for micromachines. Swimming is the result of the net displacement by performing a body deformation. For example, microorganisms such as bacteria are active enough to migrate in the fluid and there is a mechanism to gain net displacements. Motor proteins in cells exhibit material transport, and it is necessary to gain net displacements. Swimming motions are studied both experimentally and theoretically as an essential problem of non-equilibrium systems [1.16, 1.17]. Scallop theorem is a theorem that describes the basic mechanism of swimming micromachines [1.18]. This theorem was proposed in 1977 by Purcell, but has been proven only recently [1.19].

1.3   Scallop theorems

Scallop theorem states the essential mechanism for swimming by using body deformation of a micromachine. According to this theorem, swimmers in Newtonian fluids can not attain any directed motion with a reciprocal motion, i.e., a time-reversal motion. This means that a tiny scallop cannot swim by performing simple open and close motions. We note that a time reversal motion cannot make a closed area in the phase space of deformations (see the right figure in Fig.1.1), while a non-reciprocal motion can make a closed area (see the left figure in Fig.1.1).
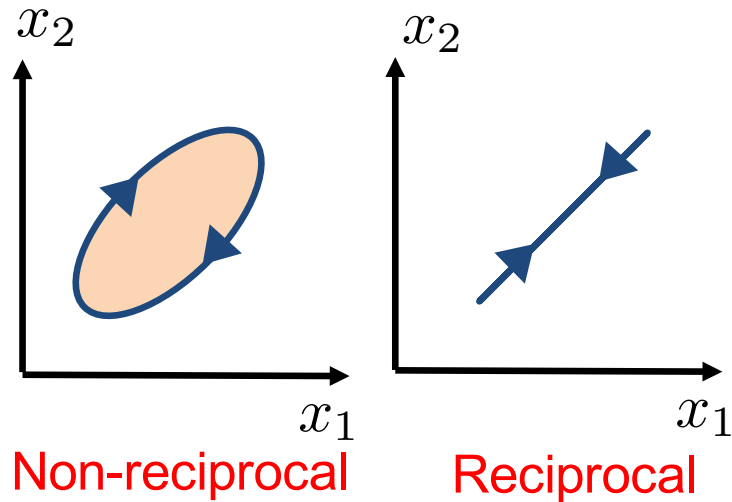
Figure 1.1: Left: non-reciplocal motion in space of freedom degree of motions. Right: reciplocal motion.

1.4 Three sphere swimmer

As one of the simplest models exhibiting broken time-reversal symmetry in a viscous fluid, Najafi and Golestanian proposed a three-sphere swimmer [1.20, 1.21], in which three in-line spheres are linked by two arms of varying length (see Fig.1.2). This model is suitable for analytical analysis because it is sufficient to consider only the translational motion, and the tensorial structure of the fluid motion can be neglected. Such a three-sphere swimmer has been experimentally realized by using ferromagnetic particles and by applying an oscillating magnetic field [1.22]. This model have attracted many interests, and many similar models have been proposed.

1.5 Aim of this thesis

In this thesis, I shall discuss various situations of three-sphere swimmers [1.23–1.25]. In the Sec. 2, we show three-sphere swimmers in viscoelastic medium. We discuss elastic swimmers in viscous fluid in Sec. 3. We also argue thermally-driven

4
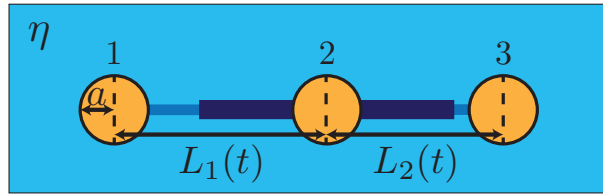
Figure 1.2: Najafi-Golestanian three-sphere swimmer model. Three identical spheres of radius a are connected by arms of lengths $L_1(t)$ and $L_2(t)$ and undergo time-dependent cyclic motion. The swimmer is embedded in a viscous fluid characterized by a shear viscosity η.

elastic swimmers in Sec. 4.

On the other hand, we investigate anomalous diffusion in living cell in Sec. 5. Finally, we will discuss membrane fluctuations in non-equilibrium system in Secs. 6 and 7.

Bibliography

[1.1] T. M. Squires and T. G. Mason, Annu. Rev. Fluid Mech. **42**, 413 (2010).

[1.2] D. T. N. Chen, Q. Wen, P. A. Janmey, J. C. Crocker, and A. G. Yodh, Annu. Rev. Condens. Matter Phys. **1**, 301 (2010).

[1.3] M. Guo, A. J. Ehrlicher, M. H. Jensen, M. Renz, J. R. Moore, R. D. Goldman, J. Lippincott-Schwartz, F. C. MacKintosh, and D. A. Weitz, Cell **158**, 822 (2014).

[1.4] H. Turlier, D. A. Fedosov, B. Audoly, T. Auth, N. S. Gov, C. Sykes, J.-F. Joanny, G. Gompper, and T. Betz, Nat. Phys. **12**, 513 (2016).

[1.5] K. Yasuda, R. Okamoto, S. Komura, and A. S. Mikhailov, EPL **117**, 38001 (2017).

[1.6] K. Yasuda, R. Okamoto, and S. Komura, Phys. Rev. E **95**, 032417 (2017).

[1.7] Y. Hosaka, K. Yasuda, R. Okamoto, and S. Komura, Phys. Rev. E **95**, 052407 (10pp) (2017).

[1.8] K. Yasuda, S. Komura, and R. Okamoto, Phys. Rev. E **93**, 052407 (2016).

[1.9] S. Komura, K. Yasuda, and R. Okamoto, J. Phys.: Condens. Matter **27**, 432001 (2015).

[1.10] H. S. Muddana, S. Sengupta, T. E. Mallouk, A. Sen, and P. J. Butler, J. Am. Chem. Soc. **132**, 2110 (2010).

[1.11] S. Sengupta, K. K. Dey, H. S. Muddana, T. Tabouillot, M. E. Ibele, P. J. Butler, and A. Sen, J. Am. Chem. Soc. **135**, 1406 (2013).

[1.12] C. Riedel, R. Gabizon, C. A. M. Wilson, K. Hamadani, K. Tsekourasl, S. Marqusee, S. Presse, and C. Bustamante, Nature (London) **517**, 227 (2015).

[1.13] R. Golestanian, Phys. Rev. Lett. **115**, 108102 (2015).

[1.14] P. Illien, X. Zhao, K. K. Dey, P. J. Butler, A. Sen, and R. Golestanian, Nano Lett. **17**, 4415 (2017).

[1.15] P. Illien, T. Adeleke-Larodo, and R. Golestanian, EPL **119**, 40002 (2017).

[1.16] T. Qiu, T. -C. Lee, A. G. Mark, K. I. Morozov, R. Munster, O. Mierka, S. Turek, A. M. Leshansky, and P. Fischer, Nat. Commun. **5**, 5119 (2014).

[1.17] K. Ishimoto, H. Gadelha, E. A. Gaffney, D. J. Smith and J. Kirkman-Brown, Phys. Rev. Lett. **118**, 124501 (2017).

[1.18] E. M. Purcell, Am. J. Phys. **45**, 3 (1977).

[1.19] K. Ishimoto and M. Yamada, SIAM J. Appl. Math. **72**, 1686 (2012).

[1.20] A. Najafi and R. Golestanian, Phys. Rev. E **69**, 062901 (2004).

[1.21] R. Golestanian and A. Ajdari, Phys. Rev. E **77**, 036308 (2008).

[1.22] G. Grosjean, M. Hubert, G. Lagubeau, and N. Vandewalle, Phys. Rev. E **94**, 021101(R) (2016).

[1.23] K. Yasuda, R. Okamoto, and S. Komura, J. Phys. Soc. Jpn. **86**, 043801 (2017).

[1.24] K. Yasuda, Y. Hosaka, M. Kuroda, R. Okamoto, and S. Komura, J. Phys. Soc. Jpn. **86**, 093801 (2017).

[1.25] Y. Hosaka, K. Yasuda, I. Sou, R. Okamoto, and S. Komura, J. Phys. Soc. Jpn. **86**, 113801 (2017).

Chapter 2

Swimmer-microrheology

We discuss the locomotion of a three-sphere microswimmer in a viscoelastic medium and propose a new type of active microrheology. We derive a relation that connects the average swimming velocity and the frequency-dependent viscosity of the surrounding medium. In this relation, the viscous contribution can exist only when the time-reversal symmetry is broken, whereas the elastic contribution is present only when the structural symmetry of the swimmer is broken. Purcell's scallop theorem breaks down for a three-sphere swimmer in a viscoelastic medium.

2.1   Introduction

Microrheology is one of the most useful techniques for measuring the rheological properties of soft matter and various biological materials including cells [2.1, 2.2]. There are two different methods: passive microrheology and active microrheology. In passive microrheology, both the local and bulk mechanical properties of a medium can be extracted from the Brownian motion of a probe particle [2.3, 2.4]. In this method, the generalized Stokes–Einstein relation (GSER) is used to analyze thermal diffusive motion. In active microrheology, on the other hand, the probe is actively pulled through the fluid with the aims of driving the medium out of equilibrium and measuring mechanical responses [2.5, 2.6]. Within linear

response theory, the generalized Stokes relation (GSR) is employed to obtain the frequency-dependent complex shear modulus.

In this Letter, we propose a new type of active microrheology using a microswimmer. Microswimmers are tiny machines that swim in a fluid such as sperm cells or motile bacteria, and are expected to be applied to microfluidics and microsystems [2.7]. As one of the simplest microswimmers, we consider the Najafi–Golestanian three-sphere swimmer model [2.8, 2.9], where three in-line spheres are linked by two arms of varying length (see Fig. 2.1). Recently, such a swimmer has been experimentally realized [2.10]. We investigate its motion in a general viscoelastic medium, and obtain a relation that connects the average swimming velocity and the frequency-dependent complex shear viscosity of the surrounding viscoelastic medium. We show explicitly that the absence of the time-reversal symmetry of the swimmer motion leads to the real part of the viscosity, whereas the absence of the structural symmetry of the swimmer is reflected in the imaginary part of the viscosity. Hence, we shall call the proposed method the "swimmer-microrheology". Our result also indicates that Purcell's scallop theorem [2.11, 2.12], which states that time-reversible body motion cannot be used for locomotion in a Newtonian fluid, breaks down for a three-sphere swimmer in viscoelastic media if the structural symmetry is violated.

2.2   Model

The general equation that describes the hydrodynamics of a low-Reynolds-number flow in a viscoelastic medium is given by the following generalized Stokes equation [2.13]:

$$0 = \int_{-\infty}^{t} \mathrm{d}t' \, \eta(t - t') \nabla^2 \mathbf{v}(\mathbf{r}, t') - \nabla p(\mathbf{r}, t). \tag{2.1}$$

Here $\eta(t)$ is the time-dependent shear viscosity, $\mathbf{v}$ is the velocity field, p is the pressure field, and $\mathbf{r}$ stands for a three-dimensional positional vector. The above equation is further subjected to the incompressibility condition, $\nabla \cdot \mathbf{v} = 0$. From

9

these equations, one can obtain a linear relation between the time-dependent force $F(t)$ acting on a hard sphere of radius a and its time-dependent velocity $V(t)$. In the Fourier domain, this relation can be represented as

$$V(\omega) = \frac{1}{6\pi\eta[\omega]a}F(\omega), \tag{2.2}$$

where we use a bilateral Fourier transform for $V(\omega) = \int_{-\infty}^{\infty} dt\, V(t)e^{-i\omega t}$ and $F(\omega)$, while we employ a unilateral one for $\eta[\omega] = \int_{0}^{\infty} dt\, \eta(t)e^{-i\omega t}$. Equation (2.2) is the GSR, which has been successfully used in active microrheology experiments [2.5], and its mathematical validity has also been discussed [2.6].

Next, we briefly explain the three-sphere model for a minimum swimmer introduced by Najafi and Golestanian [2.8, 2.9]. As schematically shown in Fig. 2.1, this model consists of three spheres of the same radius a that are connected by two arms of lengths $L_1(t)$ and $L_2(t)$, which undergo time-dependent motion. Their explicit time dependences will be given later. If we define the velocity of each sphere along the swimmer axis as $V_i(t)$ with $i = 1, 2, 3$, we have

$$\dot{L}_1(t) = V_2(t) - V_1(t), \tag{2.3}$$

$$\dot{L}_2(t) = V_3(t) - V_2(t), \tag{2.4}$$

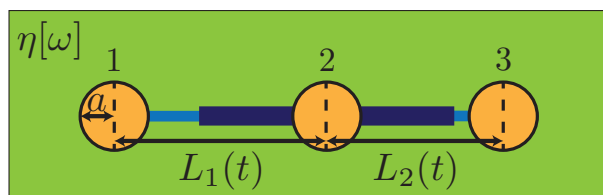where $\dot{L}_1$ and $\dot{L}_2$ indicate time derivatives.

Figure 2.1: Najafi–Golestanian three-sphere swimmer model. Three identical spheres of radius a are connected by arms of lengths $L_1(t)$ and $L_2(t)$ and undergo time-dependent cyclic motion. The swimmer is embedded in a viscoelastic medium characterized by a frequency-dependent complex shear viscosity $\eta[\omega]$.

Owing to the hydrodynamic effect, each sphere exerts a force F_i on the viscoelastic medium and experiences a force $-F_i$ from it. To relate the forces and the velocities in the frequency domain, we use the GSR in Eq. (2.2) and the Oseen tensor, in which the frequency-dependent viscosity $\eta[\omega]$ is used instead of a constant one [2.3, 2.4]. Assuming that $a \ll L_1, L_2$, we can write [2.8, 2.9]

$$V_1(\omega) = \frac{F_1(\omega)}{6\pi\eta[\omega]a} + \frac{1}{4\pi\eta[\omega]}\frac{F_2(\omega) * L_1^{-1}(\omega)}{2\pi} + \frac{1}{4\pi\eta[\omega]}\frac{F_3(\omega) * (L_1 + L_2)^{-1}(\omega)}{2\pi},$$

(2.5)

$$V_2(\omega) = \frac{1}{4\pi\eta[\omega]}\frac{F_1(\omega) * L_1^{-1}(\omega)}{2\pi} + \frac{F_2(\omega)}{6\pi\eta[\omega]a} + \frac{1}{4\pi\eta[\omega]}\frac{F_3(\omega) * L_2^{-1}(\omega)}{2\pi}, \quad (2.6)$$

$$V_3(\omega) = \frac{1}{4\pi\eta[\omega]}\frac{F_1(\omega) * (L_1 + L_2)^{-1}(\omega)}{2\pi} + \frac{1}{4\pi\eta[\omega]}\frac{F_2(\omega) * L_2^{-1}(\omega)}{2\pi} + \frac{F_3(\omega)}{6\pi\eta[\omega]a},$$

(2.7)

where we have used bilateral Fourier transforms such as $L_1^{-1}(\omega) = \int_{-\infty}^{\infty} dt\, [L_1(t)]^{-1} e^{-i\omega t}$. Furthermore, the convolution of two functions is generally defined by $g_1(\omega) * g_2(\omega) = \int_{-\infty}^{\infty} d\omega'\, g_1(\omega - \omega')g_2(\omega')$ in the above equations.

As in the original study, we are interested in the autonomous net locomotion of the swimmer, and there are no external forces acting on the spheres. If the inertia of the surrounding fluid can be neglected, we have the following force balance condition:

$$F_1(t) + F_2(t) + F_3(t) = 0. \quad (2.8)$$

Since Eqs. (2.5)–(2.7) involve convolutions in the frequency domain, we cannot solve these equations for arbitrary $L_1(t)$ and $L_2(t)$. Here we assume that the two arms undergo the following periodic motion:

$$L_1(t) = \ell + d_1 \cos(\Omega t), \quad (2.9)$$

$$L_2(t) = \ell + d_2 \cos(\Omega t - \phi). \quad (2.10)$$

In the above, ℓ is the constant length, d_1 and d_2 are the amplitudes of the oscillatory

motion, Ω is the common arm frequency, and ϕ is the mismatch in the phases between the two arms. In the following analysis, we generally assume that $d_1, d_2 \ll \ell$. The *time-reversal symmetry* of the arm motion is present when $\phi = 0$ and π. Furthermore, we characterize the *structural symmetry* of the swimmer by d_1 and d_2, i.e., the structure is symmetric when $d_1 = d_2$, while it is asymmetric when $d_1 \neq d_2$.

2.3 Results

Since the arm frequency is Ω, we assume that the velocities and the forces of the three spheres can generally be written as

$$V_i(\omega) = V_{i,0}\,\delta(\omega) + \sum_{n=1}^{\infty} \left[V_{i,n}\,\delta(\omega + n\Omega) + V_{i,-n}\,\delta(\omega - n\Omega) \right], \qquad (2.11)$$

$$F_i(\omega) = F_{i,0}\,\delta(\omega) + \sum_{n=1}^{\infty} \left[F_{i,n}\,\delta(\omega + n\Omega) + F_{i,-n}\,\delta(\omega - n\Omega) \right], \qquad (2.12)$$

where $i = 1, 2, 3$ for the three spheres. Substituting Eqs. (2.11) and (2.12) into the six coupled Eqs. (2.3)–(2.8), we obtain a matrix equation with infinite dimensions.

Under the conditions $d_1, d_2 \ll \ell$ and $a \ll \ell$, we are allowed to consider only $n = -1, 0, 1$ and we further use the approximation $F_{i,\pm 2} \approx 0$. Then we can solve for the six unknown functions $V_i(\omega)$ and $F_i(\omega)$, and also calculate the total swimming velocity $V = (V_1 + V_2 + V_3)/3$. Up to the lowest order terms in a, the average swimming velocity over one cycle of motion becomes [see also Appendix 2.A]

$$\overline{V} \approx \frac{7 d_1 d_2 a\Omega}{24\ell^2} \frac{\eta'[\Omega]}{\eta_0} \sin\phi - \frac{5(d_1^2 - d_2^2)a\Omega}{48\ell^2} \frac{\eta''[\Omega]}{\eta_0}, \qquad (2.13)$$

where $\eta'[\Omega]$ and $\eta''[\Omega]$ are the real and imaginary parts of the complex shear viscosity, respectively, and $\eta_0 = \eta[\Omega \to 0]$ is the constant zero-frequency viscosity.

The first term in Eq. (2.13) can be regarded as the viscous contribution and is present only if the time-reversal symmetry of the swimmer motion is broken,

Table 2.1: Locomotion of a three-sphere swimmer in a viscoelastic medium and the relevant rheological information.

medium	viscous				viscoelastic			
time-reversal symmetry	Y		N		Y		N	
structural symmetry	Y	N	Y	N	Y	N	Y	N
swimmer motion	N	N	Y	Y	N	Y	Y	Y
rheological information	$-$	$-$	N	N	$-$	η''	η'	η', η''

i.e., $\phi \neq 0, \pi$. The second term, on the other hand, corresponds to the elastic contribution, and exists only when the structural symmetry of the swimmer is broken, i.e., $d_1 \neq d_2$. If we are able to control d_1, d_2, and Ω of the swimmer, we can first obtain $\eta'[\Omega]$ by measuring $\overline{V}$ as a function of Ω by setting $d_1 = d_2$. Then we make a difference between d_1 and d_2 to examine the change in $\overline{V}$, which then yields $\eta''[\Omega]$. The corresponding complex shear modulus is simply obtained by $G[\Omega] = i\Omega\eta[\Omega]$. This is a new type of active microrheology that we propose in this Letter.

For a purely Newtonian fluid, namely, for a medium characterized by a constant viscosity, the second term in Eq. (2.13) vanishes, and the first term coincides with the expression obtained by Golestanian and Ajdari [2.9]. It should be noted here, however, that the velocity $\overline{V}$ in this case no longer depends on the constant viscosity (because $\eta'[\Omega]/\eta_0 = 1$) and we cannot measure it from $\overline{V}$. Equation (2.13) also implies that the swimmer cannot move in a purely elastic medium, for which we have $\eta_0 \to \infty$. Importantly, owing to the presence of the second term, Purcell's scallop theorem breaks down for a three-sphere swimmer in a viscoelastic medium. Namely, even if the time-reversal symmetry of the swimmer motion is not broken, i.e., $\phi = 0, \pi$, the present swimmer can still move in a viscoelastic medium due to the second term as long as its structural symmetry is broken, i.e., $d_1 \neq d_2$. On the basis of Eq. (2.13), we have summarized in Table I the motion of a three-sphere swimmer in a viscoelastic medium and the relevant rheological information.

To further illustrate our result, we first assume that the surrounding viscoelastic medium is described by a simple Maxwell model. In this case, the frequency-

dependent viscosity can be written as

$$\eta[\omega] = \eta_0 \frac{1 - i\omega\tau_M}{1 + \omega^2\tau_M^2}, \tag{2.14}$$

where τ_M is the characteristic time scale. Within this model, the medium behaves as a viscous fluid for $\omega\tau_M \ll 1$, while it becomes elastic for $\omega\tau_M \gg 1$. Using Eq. (2.14), we can easily obtain the average swimming velocity in Eq. (2.13) as

$$\overline{V} = \frac{7d_1 d_2 a\Omega}{24\ell^2} \frac{1}{1 + \Omega^2\tau_M^2} \sin\phi + \frac{5(d_1^2 - d_2^2)a\Omega}{48\ell^2} \frac{\Omega\tau_M}{1 + \Omega^2\tau_M^2}. \tag{2.15}$$

The first viscous term increases as $\overline{V} \sim \Omega$ for $\Omega\tau_M \ll 1$, while it decreases as $\overline{V} \sim \Omega^{-1}$ for $\Omega\tau_M \gg 1$. This is a unique feature of the viscoelasticity [2.7, 2.14, 2.15], but such a reduction occurs simply because the medium responds elastically in the high-frequency regime. On the other hand, the second elastic term increases as $\overline{V} \sim \Omega^2$ for $\Omega\tau_M \ll 1$, and it approaches a constant for $\Omega\tau_M \gg 1$. In Fig. 2.2(a), we plot the average swimming velocity $\overline{V}$ as a function of the dimensionless arm frequency $\Omega\tau_M$ when $\phi = \pi/2$ and $d_1 = d_2$. This plot corresponds to the first term in Eq. (2.15). As a reference, the behavior of $\overline{V} \sim \Omega$ for a purely viscous fluid is also plotted. Figure 2.2(b) is a similar plot when $\phi = 0$ and $d_1 \neq d_2$, and corresponds to the second term in Eq. (2.15).

As a different example, we next consider the case in which the viscoelastic medium is described by a power-law model such that [2.13, 2.16, 2.17]

$$\eta[\omega] = G_0(i\omega)^{\alpha-1}, \tag{2.16}$$

where the exponent can take values of $0 \leq \alpha \leq 1$. With this expression, the complex shear modulus also exhibits a power-law behavior, $G[\omega] = G_0(i\omega)^{\alpha}$. The limits of $\alpha = 0$ and 1 correspond to the purely elastic and the purely viscous cases, respectively. In the case of a power-law fluid, the average swimming velocity can

14

be obtained from Eqs. (2.13) and (2.16) as

$$\overline{V} = \frac{7d_1 d_2 a}{24\ell^2 \tau_{\mathrm{p}}} (\Omega\tau_{\mathrm{p}})^\alpha \sin(\pi\alpha/2) \sin\phi + \frac{5(d_1^2 - d_2^2)a}{48\ell^2 \tau_{\mathrm{p}}} (\Omega\tau_{\mathrm{p}})^\alpha \cos(\pi\alpha/2), \qquad (2.17)$$

where $\tau_{\mathrm{p}} = (\eta_0/G_0)^{1/(1-\alpha)}$. Here we have assumed that the medium behaves as a purely viscous fluid in the low-frequency limit characterized by a finite viscosity η_0. According to the above expression, the swimming velocity scales as $\overline{V} \sim \Omega^\alpha$ in both the first and second terms. For the purely viscous case of $\alpha = 1$, the first term reduces to the result by Golestanian and Ajdari [2.9], while the second term vanishes. For the purely elastic case of $\alpha = 0$, on the other hand, the first term vanishes and the second term remains, although the latter no longer depends on the arm frequency Ω. In Figs. 2.2(a) and 2.2(b), we have also plotted the average velocity $\overline{V}$ as a function of $\Omega\tau_{\mathrm{p}}$ when $\alpha = 1/2$. In both of these plots, the scaling behavior $\overline{V} \sim \Omega^{1/2}$ is seen.

2.4 Conclusion

Lauga considered the axisymmetric squirming motion of a sphere (squirmer) embedded in an Oldroyd-B fluid, which represents a typical polymeric fluid [2.18]. He reported that the scallop theorem in a viscoelastic fluid breaks down if the squirmer has fore-aft asymmetry in its surface velocity distribution. For a time-reversal deformation given by a simple sinusoidal gait, he showed that the average swimming velocity is given by $\overline{V} \sim \Omega\mathrm{De}/(1 + \mathrm{De}^2)$, where the Deborah number is given by $\mathrm{De} = \Omega\tau_{\mathrm{O}}$ with a characteristic relaxation time τ_{O} in the Oldroyd-B model. Such a frequency dependence of the swimming velocity is identical to the second term of Eq. (2.15) obtained for a Maxwell fluid, although Eq. (2.13) is more general. On the other hand, our result is different from that by Curtis and Gaffney [2.19], because they showed that the swimming velocity in a viscoelastic medium is the same as that in a Newtonian fluid.

To summarize, we have proposed a new active microrheology using the Najafi–

Golestanian three-sphere swimmer. The frequency dependence of the average swimming speed provides us with the complex shear viscosity of the surrounding viscoelastic medium. Here the viscous contribution can exist only when the time-reversal symmetry of the swimmer is broken, whereas the elastic contribution is present only if its structural symmetry is broken.

Even though the argument in this Letter is restricted to the artificial three-sphere swimmer, we expect that our basic concept can still be applied to more complex biological processes such as the motion of bacteria, flagellated cellular swimming, and the beating of cilia. Since most of these phenomena take place in a viscoelastic environment, we hope that the concept of our new active microrheology will be used in the future to reveal their mechanical and dynamical properties.

Appendix 2.A   Derivation of Eq. (2.13)

In this appendix, we show the detailed derivation of Eq. (2.13). Substituting Eqs. (2.9) and (2.11) into Eq. (2.3), we obtain

$$V_{2,0} - V_{1,0} = 0, \tag{2.18}$$

$$V_{2,1} - V_{1,1} = -i\pi d_1 \Omega, \tag{2.19}$$

$$V_{2,-1} - V_{1,-1} = i\pi d_1 \Omega, \tag{2.20}$$

$$V_{2,n} - V_{1,n} = 0 \quad \text{for } |n| \geq 2. \tag{2.21}$$

Similarly, substituting Eqs. (2.10) and (2.11) into Eq. (2.4), we obtain

$$V_{3,0} - V_{2,0} = 0, \tag{2.22}$$

$$V_{3,1} - V_{2,1} = \pi d_2 \Phi_2 \Omega, \tag{2.23}$$

$$V_{3,-1} - V_{2,-1} = \pi d_2 \Phi_1 \Omega, \tag{2.24}$$

$$V_{3,n} - V_{2,n} = 0 \quad \text{for } |n| \geq 2, \tag{2.25}$$

where we have used the following notations

$$\Phi_1 = i\cos\phi + \sin\phi, \tag{2.26}$$

$$\Phi_2 = -i\cos\phi + \sin\phi. \tag{2.27}$$

Next we expand Eqs. (2.5), (2.6) and (2.7) in terms of the small quantities d_1/ℓ and d_2/ℓ while keeping only the lowest order terms. Substituting Eqs. (2.11) and (2.12) into these three equations, we obtain

$$V_{1,n} \approx \frac{F_{1,n}}{6\pi\eta[-n\Omega]a} + \frac{1}{4\pi\eta[-n\Omega]\ell}\left(F_{2,n} - \frac{d_1 F_{2,n+1}}{2\ell} - \frac{d_1 F_{2,n-1}}{2\ell}\right)$$
$$+ \frac{1}{4\pi\eta[-n\Omega]\ell}\left(\frac{F_{3,n}}{2} - \frac{d_1 F_{3,n+1}}{8\ell} - \frac{d_1 F_{3,n-1}}{8\ell} + \frac{id_2\Phi_1 F_{3,n+1}}{8\ell} - \frac{id_2\Phi_2 F_{3,n-1}}{8\ell}\right), \tag{2.28}$$

$$V_{2,n} \approx \frac{1}{4\pi\eta[-n\Omega]\ell}\left(F_{1,n} - \frac{d_1 F_{1,n+1}}{2\ell} - \frac{d_1 F_{1,n-1}}{2\ell}\right) + \frac{F_{2,n}}{6\pi\eta[-n\Omega]a}$$
$$+ \frac{1}{4\pi\eta[-n\Omega]\ell}\left(F_{3,n} + \frac{id_2\Phi_1 F_{3,n+1}}{2\ell} - \frac{id_2\Phi_2 F_{3,n-1}}{2\ell}\right), \tag{2.29}$$

$$V_{3,n} \approx \frac{1}{4\pi\eta[-n\Omega]\ell}\left(\frac{F_{1,n}}{2} - \frac{d_1 F_{1,n+1}}{8\ell} - \frac{d_1 F_{1,n-1}}{8\ell} + \frac{id_2\Phi_1 F_{1,n+1}}{8\ell} - \frac{id_2\Phi_2 F_{1,n-1}}{8\ell}\right)$$
$$+ \frac{1}{4\pi\eta[-n\Omega]\ell}\left(F_{2,n} + \frac{id_2\Phi_1 F_{2,n+1}}{2\ell} - \frac{id_2\Phi_2 F_{2,n-1}}{2\ell}\right) + \frac{F_{3,n}}{6\pi\eta[-n\Omega]a}. \tag{2.30}$$

Note that the couplings between different n-modes are involved in these equations. Finally, substituting Eq. (2.12) into Eq. (2.8), we obtain

$$F_{1,n} + F_{2,n} + F_{3,n} = 0. \tag{2.31}$$

The above set of equations constitute a matrix equation with infinite dimensions and cannot be solved in general. Under the assumption of $a \ll \ell$, however, we are allowed to consider only $n = -1, 0, 1$ and further approximate as $F_{i,\pm 2} \approx 0$. The justification of the latter approximation is also seen by solving Eqs. (2.21), (2.25), (2.28), (2.29), (2.30) and (2.31) for $n = \pm 2$ and taking the limit of $a \ll \ell$.

Hence the above set of equations can be solved for 18 unknowns, i.e., $V_{i,n}$ and $F_{i,n}$ for $i = 1, 2, 3$ and $n = -1, 0, 1$.

The velocity of each sphere is simply obtained by the inverse Fourier transform, $V_i(t) = (2\pi)^{-1} \int_{-\infty}^{\infty} d\omega \, V_i(\omega) e^{i\omega t}$. The average swimming velocity over one cycle of motion is then calculated by

$$\overline{V} = \frac{\Omega}{2\pi} \int_0^{2\pi/\Omega} dt \, [V_1(t) + V_2(t) + V_3(t)]/3. \tag{2.32}$$

Up to the lowest order terms in a, we finally obtain Eq. (2.13). In order to obtain more accurate higher order terms in a, one needs to take into account the higher order n-modes ($|n| \geq 2$).

Bibliography

[2.1] T. M. Squires and T. G. Mason, Annu. Rev. Fluid Mech. **42**, 413 (2010).

[2.2] D. T. N. Chen, Q. Wen, P. A. Janmey, J. C. Crocker, and A. G. Yodh, Annu. Rev. Condens. Matter Phys. **1**, 301 (2010).

[2.3] T. G. Mason and D. A. Weitz, Phys. Rev. Lett. **74**, 1250 (1995).

[2.4] T. G. Mason, Rheol. Acta **39**, 371 (2000).

[2.5] F. Gittes, B. Schnurr, P. D. Olmsted, F. C. MacKintosh, and C. F. Schmidt, Phys. Rev. Lett. **79**, 3286 (1997).

[2.6] B. Schnurr, F. Gittes, F. C. MacKintosh, and C. F. Schmidt, Macromolecules **30**, 7781 (1997).

[2.7] E. Lauga and T. R. Powers, Rep. Prog. Phys. **72** 096601 (2009).

[2.8] A. Najafi and R. Golestanian, Phys. Rev. E **69**, 062901 (2004).

[2.9] R. Golestanian and A. Ajdari, Phys. Rev. E **77**, 036308 (2008).

[2.10] G. Grosjean, M. Hubert, G. Lagubeau, and N. Vandewalle, Phys. Rev. E **94**, 021101(R) (2016).

[2.11] E. M. Purcell, Am. J. Phys. **45**, 3 (1977).

[2.12] E. Lauga, Soft Matter **7**, 3060 (2011).

[2.13] R. Granek, Soft Matter **7**, 5281 (2011).

[2.14] H. C. Fu, T. R. Powers, and C. W. Wolgemuth, Phys. Rev. Lett. **99**, 258101 (2007).

[2.15] H. C. Fu, C. W. Wolgemuth, and T. R. Powers, Phys. Fluids **21**, 033102 (2009).

[2.16] S. Komura, S. Ramachandran, and K. Seki, EPL **97**, 68007 (2012).

[2.17] S. Komura, K. Yasuda, and R. Okamoto, J. Phys.: Condens. Matter **27**, 432001 (2015).

[2.18] E. Lauga, EPL **86**, 64001 (2009).

[2.19] M. P. Curtis and E. A. Gaffney, Phys. Rev. E **87**, 043006 (2013).
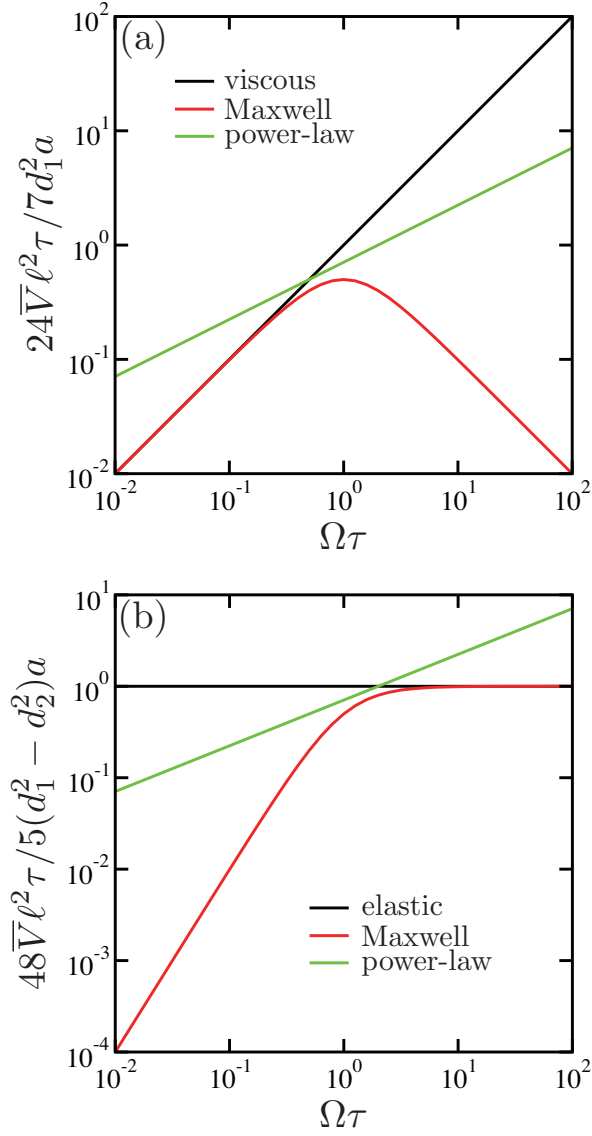
Figure 2.2: Average swimming velocity $\overline{V}$ as a function of $\Omega\tau$, where Ω is the arm frequency and τ represents either τ_{M} for a Maxwell fluid (red lines) or τ_{p} for a power-law fluid (green lines). In the power-law model, we choose $\alpha = 1/2$. (a) Viscous contribution by setting $\phi = \pi/2$ and $d_1 = d_2$. Here $\overline{V}$ is scaled by $7d_1^2a/(24\ell^2\tau)$. The case for a viscous fluid is plotted by the black line. (b) Elastic contribution by setting $\phi = 0$ and $d_1 \neq d_2$. Here $\overline{V}$ is scaled by $5(d_1^2 - d_2^2)a/(48\ell^2\tau)$. The case for an elastic medium is plotted by the black line.

Chapter 3

Elastic three-sphere microswimmer in a viscous fluid

We discuss the dynamics of a generalized three-sphere microswimmer in which the spheres are connected by two elastic springs. The natural length of each spring is assumed to undergo a prescribed cyclic change. We analytically obtain the average swimming velocity as a function of the frequency of cyclic change in the natural length. In the low-frequency region, the swimming velocity increases with frequency, and its expression reduces to that of the original three-sphere model by Najafi and Golestanian. Conversely, in the high-frequency region, the average velocity decreases with increasing frequency. Such behavior originates from the intrinsic spring relaxation dynamics of an elastic swimmer moving in a viscous fluid.

3.1 Introduction

Microswimmers are tiny machines that swim in a fluid, such as sperm cells or motile bacteria, and they are expected to be applied to microfluidics and microsystems [3.1]. By transforming chemical energy into mechanical work, microswimmers change their shape and move in viscous environments. Over the length scale of

21

microswimmers, the fluid forces acting on them are governed by the effect of viscous dissipation. According to Purcell's scallop theorem [3.2], time-reversal body motion cannot be used for locomotion in a Newtonian fluid [3.3]. As one of the simplest models exhibiting broken time-reversal symmetry, Najafi and Golestanian proposed a three-sphere swimmer [3.4, 3.5], in which three in-line spheres are linked by two arms of varying length. This model is suitable for analytical analysis because it is sufficient to consider only the translational motion, and the tensorial structure of the fluid motion can be neglected. Recently, such a swimmer has been experimentally realized by using ferromagnetic particles at an air-water interface and by applying an oscillating magnetic field [3.6].

The original Najafi–Golestanian model has been further extended to various situations, such as the case when one of the spheres has a larger radius [3.7] or when three spheres are arranged in a triangular configuration [3.8]. Montino and DeSimone considered the case in which one arm is periodically actuated while the other is replaced by a passive elastic spring [3.9]. It was shown that such a swimmer exhibits a delayed mechanical response of the passive spring with respect to the active arm. More recently, they analyzed the motion of a three-sphere swimmer with arms having active viscoelastic properties mimicking muscular contraction [3.10]. Recently, Nasouri *et al.* discussed the motion of an elastic two-sphere swimmer, in which one of the sphere is a neo-Hookean solid [3.11].

Another approach for extending the Najafi–Golestanian model is to consider the arm motions as occurring stochastically [3.12, 3.13], rather than assuming a prescribed sequence of deformations [3.4, 3.5]. In these models, the configuration space of a swimmer generally consists of a finite number of distinct states. A similar idea was employed by Sakaue *et al.*, who discussed the propulsion of molecular machines or active proteins in the presence of hydrodynamic interactions [3.14]. Later, Huang *et al.* considered a modified three-sphere swimmer in a two-dimensional viscous fluid [3.15]. In their model, the spheres are connected by two springs, the lengths of which are assumed to depend on the discrete states that are cyclically switched. As a result, the dynamics of a swimmer consists of

the spring relaxation processes, which follow after each switching event.

In this letter, we discuss a generalized three-sphere swimmer in which the spheres are simply connected by two harmonic springs. The main difference between this model and the previous models is that the natural length of each spring depends on time and is assumed to undergo a prescribed cyclic change. Whereas the arms in the Najafi–Golestanian model undergo a prescribed motion regardless of the force exerted by the fluid, the sphere motion in our model is determined by the natural spring lengths representing internal states of a swimmer and also by the force exerted by the fluid. In this sense, our model is more realistic to study the locomotion of active microswimmers. We analytically obtain the average swimming velocity as a function of the frequency of cyclic change in the natural length. In order to better illustrate our result, we first explain the case in which the two spring constants are identical and the two oscillation amplitudes of the natural lengths are the same. Then, we shall discuss a general case in which these quantities are different and the phase mismatch between the natural lengths is arbitrary.

The introduction of harmonic springs between the spheres leads to an intrinsic time scale of an elastic swimmer that characterizes its internal relaxation dynamics. When the frequency of cyclic change in the natural lengths is smaller than this characteristic time, the swimming velocity increases with frequency, as in the previous works [3.5]. In the high-frequency region, on the other hand, the motion of spheres cannot follow the change in the natural length, and the average swimming velocity decreases with increasing frequency. Such a situation resembles the dynamics of the Najafi–Golestanian three-sphere swimmer in a viscoelastic medium [3.16]. We also show that, owing to the elasticity that has been introduced, the proposed micromachine can swim even if the change in the natural lengths is reciprocal as long as its structural symmetry is violated. Although the considered swimmer appears to be somewhat trivial, it can be regarded as a generic model for microswimmers or protein machines since the behaviors of the previous models can be deduced from our model by taking different limits.

3.2 Model

We generalize the Najafi–Golestanian three-sphere swimmer model to take into account the elasticity in the sphere motion. As schematically shown in Fig. 3.1, the present model consists of three hard spheres of the same radius a connected by two harmonic springs A and B with spring constants K_A and K_B, respectively. We assume that the natural lengths of these springs, denoted by $\ell_A(t)$ and $\ell_B(t)$, undergo cyclic time-dependent change. Their explicit time dependences will be specified later. The total energy of an elastic swimmer is then given by

$$E = \frac{K_A}{2}(x_2 - x_1 - \ell_A)^2 + \frac{K_B}{2}(x_3 - x_2 - \ell_B)^2, \qquad (3.1)$$

where $x_i(t)$ $(i = 1, 2, 3)$ are the positions of the three spheres in a one-dimensional coordinate system. We also assume $x_1 < x_2 < x_3$ without loss of generality. Owing to the hydrodynamic interaction, each sphere exerts a force on the viscous fluid of shear viscosity η and experiences an opposite force from it. In general, the surrounding medium can be viscoelastic [3.16], but such an effect is not considered in this letter.

Denoting the velocity of each sphere by $\dot{x}_i$, we can write the equations of motion of the three spheres as

$$
\begin{aligned}
\dot{x}_1 = {} & \frac{K_A}{6\pi\eta a}(x_2 - x_1 - \ell_A) - \frac{K_A}{4\pi\eta}\frac{(x_2 - x_1 - \ell_A)}{x_2 - x_1} \\
& + \frac{K_B}{4\pi\eta}\frac{(x_3 - x_2 - \ell_B)}{x_2 - x_1} - \frac{K_B}{4\pi\eta}\frac{(x_3 - x_2 - \ell_B)}{x_3 - x_1},
\end{aligned} \qquad (3.2)
$$

$$
\begin{aligned}
\dot{x}_2 = {} & \frac{K_A}{4\pi\eta}\frac{(x_2 - x_1 - \ell_A)}{x_2 - x_1} - \frac{K_A}{6\pi\eta a}(x_2 - x_1 - \ell_A) \\
& + \frac{K_B}{6\pi\eta a}(x_3 - x_2 - \ell_B) - \frac{K_B}{4\pi\eta}\frac{(x_3 - x_2 - \ell_B)}{x_3 - x_2},
\end{aligned} \qquad (3.3)
$$

$$
\begin{aligned}
\dot{x}_3 = {} & \frac{K_A}{4\pi\eta}\frac{(x_2 - x_1 - \ell_A)}{x_3 - x_1} - \frac{K_A}{4\pi\eta}\frac{(x_2 - x_1 - \ell_A)}{x_3 - x_2} \\
& + \frac{K_B}{4\pi\eta}\frac{(x_3 - x_2 - \ell_B)}{x_3 - x_2} - \frac{K_B}{6\pi\eta a}(x_3 - x_2 - \ell_B),
\end{aligned} \qquad (3.4)
$$

where we have used the Stokes' law for a sphere and the Oseen tensor in a three-dimensional viscous fluid. The swimming velocity of the whole object can be obtained by averaging the velocities of the three spheres:

$$V = \frac{1}{3}(\dot{x}_1 + \dot{x}_2 + \dot{x}_3). \tag{3.5}$$

One of the advantages of the present formulation is that the motion of the spheres is simply described by coupled ordinary differential equations. Moreover, the force-free condition for the whole system [3.4, 3.5] is automatically satisfied in the above equations.

Next, we assume that the two natural lengths of the springs undergo the following periodic changes:

$$\ell_{\mathrm{A}}(t) = \ell + d_{\mathrm{A}}\cos(\Omega t), \tag{3.6}$$

$$\ell_{\mathrm{B}}(t) = \ell + d_{\mathrm{B}}\cos(\Omega t - \phi). \tag{3.7}$$

In the above, ℓ is the common constant length, d_{A} and d_{B} are the amplitudes of the oscillatory change, Ω is the common frequency, and ϕ is the mismatch in phase between the two cyclic changes. The time-reversal symmetry of the spring dynamics exists only when $\phi = 0$ or π; otherwise, the time-reversal symmetry is broken. In the following analysis, we generally assume that $d_{\mathrm{A}}, d_{\mathrm{B}}, a \ll \ell$ and focus on the leading-order contribution. It is convenient to introduce a characteristic time scale $\tau = 6\pi\eta a/K_{\mathrm{A}}$. Then we use ℓ to scale all the relevant lengths (x_i, a, d_{A}, and d_{B}) and employ τ to scale the frequency, i.e., $\hat{\Omega} = \Omega\tau$. By further defining the ratio between the two spring constants as $\lambda = K_{\mathrm{B}}/K_{\mathrm{A}}$, the coupled Eqs. (3.2)–(3.4) can be made dimensionless.

3.3   Results

In order to discuss the essential outcome of the present model, we shall first consider the simplest symmetric case, i.e., $\lambda = 1$, $d_{\mathrm{A}} = d_{\mathrm{B}} = d$, and $\phi = \pi/2$. Hence,

Eq. (3.7) now reads $\ell_B(t) = \ell + d\sin(\Omega t)$. For our later calculation, it is useful to introduce the following spring lengths with respect to ℓ:

$$u_A = x_2 - x_1 - \ell, \qquad u_B = x_3 - x_2 - \ell. \tag{3.8}$$

Notice that these quantities are related to the sphere velocities in Eqs. (3.2)–(3.4) as

$$\dot{u}_A = \dot{x}_2 - \dot{x}_1, \qquad \dot{u}_B = \dot{x}_3 - \dot{x}_2. \tag{3.9}$$

Using Eqs. (3.2)–(3.4) and solving Eq. (3.9) in the frequency domain, we obtain the following expressions after inverse Fourier transform

$$u_A(t) \approx \frac{9 - 3\hat{\Omega} + 5\hat{\Omega}^2 + \hat{\Omega}^3}{9 + 10\hat{\Omega}^2 + \hat{\Omega}^4} d\cos(\Omega t) + \frac{6\hat{\Omega} - 4\hat{\Omega}^2 + 2\hat{\Omega}^3}{9 + 10\hat{\Omega}^2 + \hat{\Omega}^4} d\sin(\Omega t), \tag{3.10}$$

$$u_B(t) \approx -\frac{6\hat{\Omega} + 4\hat{\Omega}^2 + 2\hat{\Omega}^3}{9 + 10\hat{\Omega}^2 + \hat{\Omega}^4} d\cos(\Omega t) + \frac{9 + 3\hat{\Omega} + 5\hat{\Omega}^2 - \hat{\Omega}^3}{9 + 10\hat{\Omega}^2 + \hat{\Omega}^4} d\sin(\Omega t), \tag{3.11}$$

where we have used $a/\ell \ll 1$.

According to the calculation by Golestanian and Ajdari [3.5], the average swimming velocity of a three-sphere swimmer can generally be expressed up to the leading order in u_A/ℓ and u_B/ℓ as

$$\overline{V} = \frac{7a}{24\ell^2} \langle u_A \dot{u}_B - \dot{u}_A u_B \rangle, \tag{3.12}$$

where the averaging $\langle \cdots \rangle$ is performed by time integration in a full cycle. The above expression indicates that the average velocity is determined by the area enclosed by the orbit of periodic motion in the configuration space [3.5]. Using Eqs. (3.10) and (3.11) for an elastic microswimmer with $d/\ell, a/\ell \ll 1$, we obtain

26

the lowest-order contribution as

$$\overline{V} = \frac{7d^2 a}{24\ell^2 \tau} \frac{3\hat{\Omega}(3 + \hat{\Omega}^2)}{9 + 10\hat{\Omega}^2 + \hat{\Omega}^4}, \qquad (3.13)$$

which is an important result of this letter.

We first consider the small-frequency limit of $\hat{\Omega} \ll 1$. Physically, this limit corresponds to the case when the spring constant K_A is very large. We easily obtain

$$u_A(t) \approx d\cos(\Omega t), \qquad u_B(t) \approx d\sin(\Omega t), \qquad (3.14)$$

and

$$\overline{V} \approx \frac{7d^2 a \Omega}{24\ell^2}, \qquad (3.15)$$

which exactly coincides with the average velocity of the Najafi-Golestanian swimmer with identical spheres [3.4, 3.5]. This is reasonable because the two spring lengths u_A and u_B are in phase with their respective natural lengths ℓ_A and ℓ_B, as we can see from Eqs. (3.6), (3.7), and (3.14). Notice that the average velocity increases as $\overline{V} \sim \Omega$ in this limit, while it does not depend on the fluid viscosity η [3.4, 3.5].

In the opposite large-frequency limit of $\hat{\Omega} \gg 1$, on the other hand, we have

$$u_A(t) \approx \frac{\sqrt{5}d}{\Omega\tau} \cos[\Omega t - \arctan 2], \qquad (3.16)$$

$$u_B(t) \approx \frac{\sqrt{5}d}{\Omega\tau} \sin[\Omega t - (\pi - \arctan 2)], \qquad (3.17)$$

where $\arctan 2 \approx 1.107$ and

$$\overline{V} \approx \frac{21d^2 a}{24\ell^2 \Omega\tau^2}. \qquad (3.18)$$

We see here that u_A and u_B are out of phase with respect to the natural lengths

ℓ_A and ℓ_B, while the average velocity decreases as $\overline{V} \sim \Omega^{-1}$ when Ω is increased. When the spring constant K_A is small, it takes time for a spring to relax to its natural length, which leads to a delay in the mechanical response. The crossover frequency between the above two regimes is determined by $\hat{\Omega}^* \sim 1$. The general frequency dependence of Eq. (3.13) is shown in Fig. 3.2(a) for $\lambda = 1$ (black line). It shows a maximum around $\hat{\Omega} \sim 1$, as expected.

Recently, we investigated the motion of the Najafi-Golestanian three-sphere swimmer in a viscoelastic medium [3.16]. We derived a relation that connects the average swimming velocity and the frequency-dependent viscosity of the surrounding medium. In this relation, the viscous contribution can exist only when the time-reversal symmetry is broken, whereas the elastic contribution is present only when the structural symmetry of the swimmer is broken. In particular, we calculated the average swimming velocity when the surrounding viscoelastic medium is described by a simple Maxwell fluid with a characteristic time scale τ_M. It was shown that the viscous term increases as $\overline{V} \sim \Omega$ for $\Omega\tau_M \ll 1$, while it decreases as $\overline{V} \sim \Omega^{-1}$ for $\Omega\tau_M \gg 1$. This is a unique feature of a swimmer in a viscoelastic medium [3.16–3.18], and such a reduction occurs simply because the medium responds elastically in the high-frequency regime. We note that the frequency dependence of $\overline{V}$ for an elastic three-sphere swimmer, as obtained in Eqs. (3.13), is analogous to that for the Najafi-Golestanian swimmer in a viscoelastic Maxwell fluid. In other words, an elastic microswimmer in a viscous fluid exhibits "viscoelastic" effects as a whole.

Having discussed the simplest situation of the proposed elastic swimmer, we now show the result for a general case when $K_A \neq K_B$ (or $\lambda \neq 1$), $d_A \neq d_B$, and the phase mismatch ϕ in Eq. (3.7) is arbitrary. By repeating the same calculation

as before, the spring lengths in Eq. (3.8) now become

$$u_A(t) \approx \frac{1}{9\lambda^2 + 2(2 + \lambda + 2\lambda^2)\hat{\Omega}^2 + \hat{\Omega}^4}$$
$$\times \left\{ [9\lambda^2 + (4 + \lambda)\hat{\Omega}^2]d_A\cos(\Omega t) + 2(3\lambda^2 + \hat{\Omega}^2)\hat{\Omega}d_A\sin(\Omega t) \right.$$
$$\left. - 2\lambda(1 + \lambda)\hat{\Omega}^2 d_B\cos(\Omega t - \phi) - \lambda(-3\lambda + \hat{\Omega}^2)\hat{\Omega}d_B\sin(\Omega t - \phi) \right\}, \quad (3.19)$$

$$u_B(t) \approx \frac{1}{9\lambda^2 + 2(2 + \lambda + 2\lambda^2)\hat{\Omega}^2 + \hat{\Omega}^4}$$
$$\times \left\{ -2(1 + \lambda)\hat{\Omega}^2 d_A\cos(\Omega t) + (3\lambda - \hat{\Omega}^2)\hat{\Omega}d_A\sin(\Omega t) \right.$$
$$\left. + \lambda[9\lambda + (1 + 4\lambda)\hat{\Omega}^2]d_B\cos(\Omega t - \phi) + 2\lambda(3 + \hat{\Omega}^2)\hat{\Omega}d_B\sin(\Omega t - \phi) \right\},$$
$$(3.20)$$

respectively, where we have used $a/\ell \ll 1$. Using Eq. (3.12) again, we finally obtain the lowest-order general expression of the average velocity as

$$\overline{V} = \frac{7d_A d_B a}{24\ell^2\tau}F_1(\hat{\Omega}; \lambda)\sin\phi - \frac{7(\lambda - 1)d_A d_B a}{12\ell^2\tau}F_2(\hat{\Omega}; \lambda)\cos\phi + \frac{7(d_A^2 - d_B^2\lambda)a}{24\ell^2\tau}F_2(\hat{\Omega}; \lambda),$$
$$(3.21)$$

where the two scaling functions are defined by

$$F_1(\hat{\Omega}; \lambda) = \frac{3\lambda\hat{\Omega}(3\lambda + \hat{\Omega}^2)}{9\lambda^2 + 2(2 + \lambda + 2\lambda^2)\hat{\Omega}^2 + \hat{\Omega}^4}, \qquad (3.22)$$

$$F_2(\hat{\Omega}; \lambda) = \frac{3\lambda\hat{\Omega}^2}{9\lambda^2 + 2(2 + \lambda + 2\lambda^2)\hat{\Omega}^2 + \hat{\Omega}^4}. \qquad (3.23)$$

In Fig. 3.2, we plot the above scaling functions as functions of $\hat{\Omega}$ for $\lambda = 0.1$ and 10. Notice, however, that these two cases are essentially equivalent because we can always exchange the springs A and B, whereas we have defined the relaxation time τ by using K_A.

29

When $\lambda = 1$, $d_A = d_B$, and $\phi = \pi/2$, only the first term remains, and Eq. (3.21) reduces to Eq. (3.13), as expected. When $\lambda \neq 1$, on the other hand, the second term is present even if $\phi = 0$. The third term is also present when $d_A^2 \neq d_B^2 \lambda$, regardless of the phase mismatch ϕ. Notice that the first term represents the broken time-reversal symmetry for $\phi \neq 0$, whereas both the second and third terms reflect the structural asymmetry of an elastic three-sphere swimmer [3.16]. To be more precise, the second term is due to the difference between the relaxation times of the two springs, and the third term reflects the asymmetric changes of their natural lengths.

It is interesting to note that the frequency dependence of the second and third terms in Eq. (3.21), represented by $F_2(\hat{\Omega}, \lambda)$, is different from that of the first term, represented by $F_1(\hat{\Omega}, \lambda)$. According to Eq. (3.23), $\overline{V}$ due to the second and third terms increases as $\overline{V} \sim \Omega^2$ for $\hat{\Omega} \ll 1$, whereas it decreases as $\overline{V} \sim \Omega^{-2}$ for $\hat{\Omega} \gg 1$. In general, the overall swimming velocity depends on various structural parameters and exhibits a complex frequency dependence. For example, $F_1(\hat{\Omega}, \lambda)$ in Fig. 3.2(a) exhibits a non-monotonic frequency dependence (two maxima) for $\lambda = 0.1$ or 10 (namely, when $\lambda \neq 1$). On the other hand, an important common feature in all the terms in Eq. (3.21) is that $\overline{V}$ decreases for $\hat{\Omega} \geq 1$, which is characteristic of elastic swimmers.

We confirm again that Eq. (3.21) reduces to the result by Golestanian and Ajdari [3.5], i.e., $\overline{V} = 7 d_A d_B a \Omega \sin \phi / (24\ell^2)$, when the two spring constants are infinitely large, i.e., $K_A, K_B \to \infty$ and $\lambda = 1$. The third term in Eq. (3.21) vanishes even if $d_A \neq d_B$ because $\hat{\Omega} \to 0$ holds in this limit. In the modified three-sphere swimmer model considered by Montino and DeSimone, one of the two arms was replaced by a passive elastic spring [3.9]. Their model can be obtained from the present model simply by setting one of the spring constants to be infinitely large, say $K_A \to \infty$, and by regarding the natural length of the other spring as a constant, say $\ell_B = \ell$ (or $d_B = 0$). The continuous changes of the natural lengths introduced in Eqs. (3.6) and (3.7) are a straightforward generalization of cyclically switched discrete states considered in the previous studies [3.12–3.15]. We finally note that a

model similar to the present one was considered in Ref. [3.19], although that study focused only on the low-frequency region and did not discuss the entire frequency dependence. Using coupled Langevin equations, the authors of Ref. [3.19] mainly investigated the interplay between self-driven motion and diffusive behavior [3.19], which is also an important aspect of microswimmers.

3.4 Conclusion

To summarize, we have discussed the locomotion of a generalized three-sphere microswimmer in which the spheres are connected by two elastic springs and the natural length of each spring is assumed to undergo a prescribed cyclic change. As shown in Eqs. (3.13) and (3.21), we have analytically obtained the average swimming velocity $\overline{V}$ as a function of the frequency Ω of cyclic change in the natural length. In the low-frequency region, the swimming velocity increases with frequency and reduces to the original three-sphere model by Najafi and Golestanian [3.4, 3.5]. Conversely, in the high-frequency region, the velocity decreases with increasing frequency. This property reflects the intrinsic spring relaxation dynamics of an elastic swimmer in a viscous fluid.

Bibliography

[3.1] E. Lauga and T. R. Powers, Rep. Prog. Phys. **72** 096601 (2009).

[3.2] E. M. Purcell, Am. J. Phys. **45**, 3 (1977).

[3.3] E. Lauga, Soft Matter **7**, 3060 (2011).

[3.4] A. Najafi and R. Golestanian, Phys. Rev. E **69**, 062901 (2004).

[3.5] R. Golestanian and A. Ajdari, Phys. Rev. E **77**, 036308 (2008).

[3.6] G. Grosjean, M. Hubert, G. Lagubeau, and N. Vandewalle, Phys. Rev. E **94**, 021101(R) (2016).

[3.7] R. Golestanian, Eur. Phys. J. E **25**, 1 (2008).

[3.8] R. Ledesma-Aguilar, H. Löwen, and J. M. Yeomans, Eur. Phys. J. E **35**, 70 (2012).

[3.9] A. Montino and A. DeSimone, Eur. Phys. J. E **42**, 38 (2015).

[3.10] A. Montino and A. DeSimone, Acta Appl. Math. **149**, 53 (2017).

[3.11] B. Nasouri, A. Khot, and G. J. Elfring, Phys. Rev. Fluids **2**, 043101 (2017).

[3.12] R. Golestanian and A. Ajdari, Phys. Rev. Lett. **100**, 038101 (2008).

[3.13] R. Golestanian, Phys. Rev. Lett. **105**, 018103 (2010).

[3.14] T. Sakaue, R. Kapral, and A. S. Mikhailov, Eur. Phys. J. B **75**, 381 (2010).

[3.15] M.-J. Huang, H.-Y. Chen, and A. S. Mikhailov, Eur. Phys. J. E **119**, 35 (2012).

[3.16] K. Yasuda, R. Okamoto, and S. Komura, J. Phys. Soc. Jpn. **86**, 043801 (2017).

[3.17] E. Lauga, EPL **86**, 64001 (2009).

[3.18] M. P. Curtis and E. A. Gaffney, Phys. Rev. E **87**, 043006 (2013).

[3.19] J. Dunkel and I. M. Zaid, Phys. Rev. E **80**, 021903 (2009).

[3.20] J. Pande and A.-S. Smith, Soft Matter **11**, 2364 (2015).

[3.21] J. Pande, L. Merchant, T. Krüger, J. Harting, and A.-S. Smith, New J. Phys. **19**, 053024 (2017).
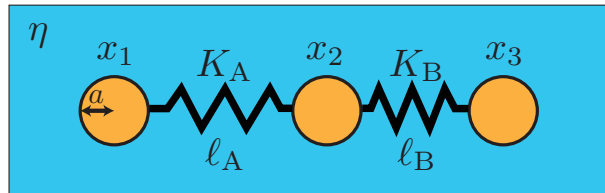
Figure 3.1: Elastic three-sphere microswimmer in a viscous fluid characterized by the shear viscosity η. Three identical spheres of radius a are connected by two harmonic springs with elastic constants K_A and K_B. The natural lengths of the springs, $\ell_A(t)$ and $\ell_B(t)$, depend on time and are assumed to undergo cyclic change [see Eqs. (3.6) and (3.7)]. The time-dependent positions of the spheres are denoted by $x_1(t)$, $x_2(t)$, and $x_3(t)$ in a one-dimensional coordinate system.
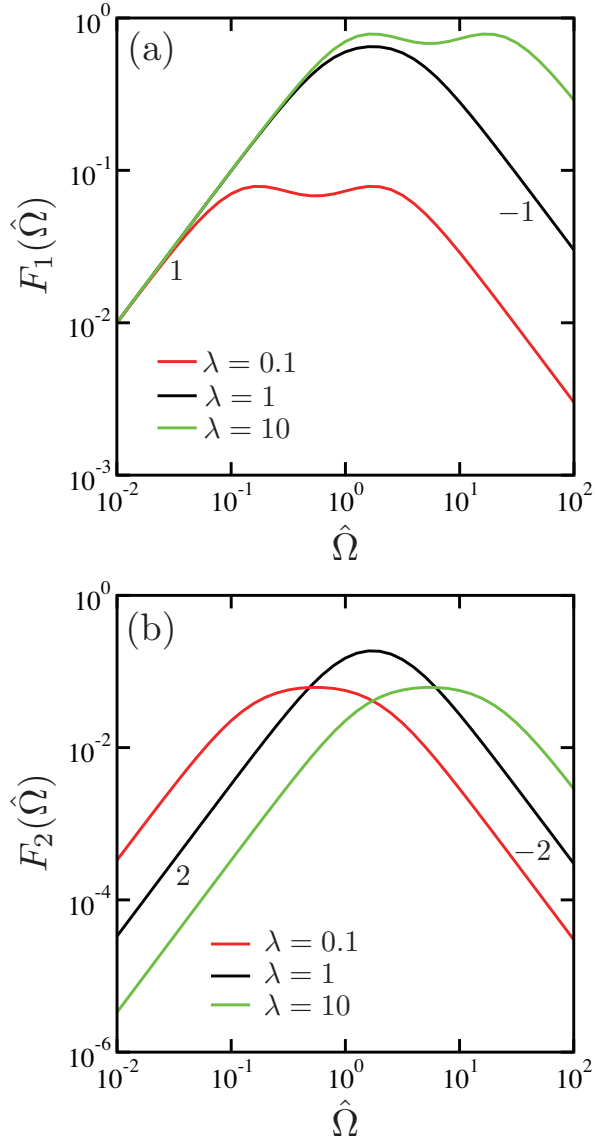
Figure 3.2: Plots of the scaling functions (a) $F_1(\hat{\Omega}; \lambda)$ and (b) $F_2(\hat{\Omega}; \lambda)$ defined in Eqs. (3.22) and (3.23), respectively, as functions of $\hat{\Omega} = \Omega\tau$ for $\lambda = K_{\mathrm{B}}/K_{\mathrm{A}} = 0.1, 1$, and 10. The numbers indicate the slope representing the exponent of the power-law behaviors.

Chapter 4

Thermally driven elastic micromachines

We discuss the directional motion of an elastic three-sphere micromachine in which the spheres are in equilibrium with independent heat baths having different temperatures. Even in the absence of prescribed motion of springs, such a micromachine can gain net motion purely because of thermal fluctuations. A relation connecting the average velocity and the temperatures of the spheres is analytically obtained. This velocity can also be expressed in terms of the average heat flows in the steady state. Our model suggests a new mechanism for the locomotion of micromachines in nonequilibrium biological systems.

4.1   Introduction

Microswimmers are tiny machines that swim in a fluid, such as sperm cells or motile bacteria, and are expected to be applied to microfluidics and microsystems [4.1]. By transforming chemical energy into mechanical work, these objects change their shape and move in viscous environments. Over the length scale of micromachines, the fluid forces acting on them are governed by viscous dissipation. According to Purcell's scallop theorem [4.2], time-reversal body motion cannot be

used for locomotion in a Newtonian fluid. As one of the simplest models exhibiting broken time-reversal symmetry, Najafi and Golestanian proposed a three-sphere swimmer [4.3, 4.4], in which three in-line spheres are linked by two arms of varying length. Recently, Pande *et al.* and the present authors independently proposed a generalized three-sphere microswimmer in which the spheres are connected by two elastic springs [4.5, 4.6].

In the previous three-sphere microswimmer models, either the arm lengths or the natural lengths of the springs were assumed to undergo prescribed cyclic motions [4.3–4.6]. Such active motions can lead to net locomotion if the swimming strokes are nonreciprocal. From a practical point of view, however, it is not a simple task to implement these motions at micron length scales. Another approach for extending the Najafi–Golestanian model is to consider the arm motions as occurring stochastically [4.7–4.10]. Although proteins or enzymes are naturally designed to include such sophisticated molecular mechanisms, it is still a substantial challenge to construct them artificially. It should also be noted that thermal agitations due to surrounding fluids become more significant at these small scales.

In this letter, by using an elastic three-sphere micromachine [4.5, 4.6], we suggest a new mechanism for locomotion that is purely induced by thermal fluctuations. To highlight this effect, we do not consider any prescribed motion of the natural lengths [4.6]. On the other hand, the key assumption in our model is that the three spheres are in equilibrium with independent heat baths having different temperatures. In this case, heat transfer occurs from a hotter sphere to a colder one, driving the whole system out of equilibrium. We show that a combination of heat transfer and hydrodynamic interactions among the spheres can lead to directional locomotion in the steady state. We analytically obtain the expression for the average velocity in terms of the sphere temperatures. Our finding is further confirmed by numerical simulations. Since our model has a similarity to a class of thermal ratchet models that have been intensively studied before [4.11–4.13], the suggested mechanism is relevant to nonequilibrium dynamics of proteins and enzymes in biological systems.

4.2 Model

As schematically shown in Fig. 4.1, we consider a three-sphere micromachine and take into account the elasticity in the internal spring motions [4.5, 4.6]. This model consists of three hard spheres of radius a connected by two harmonic springs A and B with spring constants K_A and K_B, respectively. The natural length of the springs, ℓ, is assumed to be constant. The total energy is given by

$$E = \frac{K_A}{2}(x_2 - x_1 - \ell)^2 + \frac{K_B}{2}(x_3 - x_2 - \ell)^2, \tag{4.1}$$

where $x_i(t)$ $(i = 1, 2, 3)$ are the positions of the three spheres in a one-dimensional coordinate system and we assume $x_1 < x_2 < x_3$ without loss of generality. Owing to the hydrodynamic interactions, each sphere exerts a force on the viscous fluid of shear viscosity η and experiences an opposite force from it. In general, the surrounding medium can be viscoelastic [4.14], but such an effect is not included in this letter.

We consider a situation in which the three spheres are in equilibrium with independent heat baths at temperatures T_i. When these temperatures are different, the system is driven out of equilibrium because a heat flux is generated from a hotter sphere to a colder one. Denoting the velocity of each sphere by $\dot{x}_i$, we can

write the equations of motion of the three spheres as

$$\dot{x}_1 = \frac{K_A}{6\pi\eta a}(x_2 - x_1 - \ell) - \frac{K_A}{4\pi\eta}\frac{(x_2 - x_1 - \ell)}{x_2 - x_1}$$
$$+ \frac{K_B}{4\pi\eta}\frac{(x_3 - x_2 - \ell)}{x_2 - x_1} - \frac{K_B}{4\pi\eta}\frac{(x_3 - x_2 - \ell)}{x_3 - x_1} + \xi_1, \quad (4.2)$$

$$\dot{x}_2 = \frac{K_A}{4\pi\eta}\frac{(x_2 - x_1 - \ell)}{x_2 - x_1} - \frac{K_A}{6\pi\eta a}(x_2 - x_1 - \ell)$$
$$+ \frac{K_B}{6\pi\eta a}(x_3 - x_2 - \ell) - \frac{K_B}{4\pi\eta}\frac{(x_3 - x_2 - \ell)}{x_3 - x_2} + \xi_2, \quad (4.3)$$

$$\dot{x}_3 = \frac{K_A}{4\pi\eta}\frac{(x_2 - x_1 - \ell)}{x_3 - x_1} - \frac{K_A}{4\pi\eta}\frac{(x_2 - x_1 - \ell)}{x_3 - x_2}$$
$$+ \frac{K_B}{4\pi\eta}\frac{(x_3 - x_2 - \ell)}{x_3 - x_2} - \frac{K_B}{6\pi\eta a}(x_3 - x_2 - \ell) + \xi_3, \quad (4.4)$$

where we have used the Stokes' law for a sphere and the Oseen tensor in a three-dimensional viscous fluid.

Furthermore, the white-noise sources $\xi_i(t)$ have zero mean, $\langle \xi_i(t) \rangle = 0$, and their correlations satisfy [4.15]

$$\langle \xi_i(t)\xi_j(t') \rangle = 2D_{ij}\delta(t - t'), \quad (4.5)$$

where D_{ij} is the mutual diffusion coefficient. When $i = j$, D_{ii} is simply given by the Stokes–Einstein relation, i.e.,

$$D_{ii} = \frac{k_B T_i}{6\pi\eta a}, \quad (4.6)$$

where k_B is the Boltzmann constant. When $i \neq j$, on the other hand, we assume the following general relation:

$$D_{ij} = \frac{k_B \Theta(T_i, T_j)}{4\pi\eta|x_i - x_j|}, \quad (4.7)$$

where $\Theta(T_i, T_j)$ is a function of T_i and T_j. For example, the relevant effective temperature can be the mobility-weighted average [4.16], which in the present

case is given by $\Theta(T_i, T_j) = (T_i + T_j)/2$ because all the spheres have the same size. However, its explicit functional form is not needed here, and it only needs to satisfy an appropriate fluctuation dissipation theorem in thermal equilibrium, i.e., $T_i = T_j$. This is because we only consider the limit of $a \ll \ell$ in the present study.

It is convenient to introduce a characteristic time scale given by $\tau = 6\pi\eta a/K_A$. We further define the ratio between the two spring constants as $\lambda = K_B/K_A$. We shall denote the two spring extensions by

$$u_A(t) = x_2 - x_1 - \ell, \qquad u_B(t) = x_3 - x_2 - \ell. \tag{4.8}$$

Notice that these quantities are related to the sphere velocities in Eqs. (4.2)–(4.4) as $\dot{u}_A = \dot{x}_2 - \dot{x}_1$ and $\dot{u}_B = \dot{x}_3 - \dot{x}_2$, respectively. In the following analysis, we generally assume that $u_A, u_B \ll \ell$ as well as $a \ll \ell$, and focus only on the leading-order contribution.

4.3 Results

To present the essential outcome of the model, we first consider the simplest symmetric case, i.e., $K_A = K_B$ ($\lambda = 1$). We introduce the bilateral Fourier transform for any function $f(t)$ as $f(\omega) = \int_{-\infty}^{\infty} dt\, f(t)e^{-i\omega t}$ and the inverse transform as $f(t) = \int_{-\infty}^{\infty} (d\omega/2\pi)\, f(\omega)e^{i\omega t}$. Solving the time derivative of Eq. (4.8) with the aid of Eqs. (4.2)–(4.4) in the frequency domain, we obtain

$$u_A(\omega) \approx \frac{(2 + i\omega\tau)\xi_1(\omega) - (1 + i\omega\tau)\xi_2(\omega) - \xi_3(\omega)}{-3 - 4i\omega\tau + (\omega\tau)^2}\tau + \mathcal{O}(a), \tag{4.9}$$

$$u_B(\omega) \approx \frac{\xi_1(\omega) + (1 + i\omega\tau)\xi_2(\omega) - (2 + i\omega\tau)\xi_3(\omega)}{-3 - 4i\omega\tau + (\omega\tau)^2}\tau + \mathcal{O}(a), \tag{4.10}$$

where $\mathcal{O}(a)$ indicates the terms of the order of a.

The velocity of a three-sphere micromachine is generally given by $V(t) = (\dot{x}_1 +$

$\dot{x}_2 + \dot{x}_3)/3$, which now becomes

$$V(t) \approx \frac{a}{4\ell\tau}\left(u_{\mathrm{B}} - u_{\mathrm{A}} + \frac{u_{\mathrm{B}}^2}{2\ell} - \frac{u_{\mathrm{A}}^2}{2\ell}\right)$$
$$+ \frac{1}{3}(\xi_1 + \xi_2 + \xi_3) + \mathcal{O}(u_{\mathrm{A}}^3, u_{\mathrm{B}}^3). \tag{4.11}$$

By taking its statistical average, we further obtain

$$\langle V(t) \rangle \approx \frac{a}{8\ell^2\tau}\langle u_{\mathrm{B}}^2(t) - u_{\mathrm{A}}^2(t) \rangle + \mathcal{O}(a^2, u_{\mathrm{A}}^3, u_{\mathrm{B}}^3), \tag{4.12}$$

where we have used $\langle u_{\mathrm{A}}(t) \rangle = \langle u_{\mathrm{B}}(t) \rangle = 0$ in the lowest-order of a. In the Fourier domain, Eq. (4.12) can be written in terms of convolution as

$$\langle V(\omega) \rangle \approx \frac{a}{8\ell^2\tau} \int_{-\infty}^{\infty} \frac{d\omega'}{2\pi} \langle u_{\mathrm{B}}(\omega - \omega')u_{\mathrm{B}}(\omega') - u_{\mathrm{A}}(\omega - \omega')u_{\mathrm{A}}(\omega') \rangle + \mathcal{O}(a^2, u_{\mathrm{A}}^3, u_{\mathrm{B}}^3). \tag{4.13}$$

Next, we substitute Eqs. (4.9) and (4.10) into Eq. (4.13) and use the relation $\langle \xi_i(\omega)\xi_j(\omega') \rangle = (2\pi)(2D_{ij})\delta(\omega + \omega')$, as directly obtained from Eq. (4.5). After some calculation, we have

$$\langle V(\omega) \rangle = \frac{a\tau}{4\ell^2}(D_{33} - D_{11})\frac{2\pi i}{4i\tau - \omega\tau^2}\delta(\omega). \tag{4.14}$$

Notice that the cross correlations for $i \neq j$ can be neglected here because these are higher-order contributions of $\mathcal{O}(a^2)$. Transforming back to the time domain, we obtain the average velocity as

$$\langle V \rangle = \frac{ak_{\mathrm{B}}(T_3 - T_1)}{16\tau K_{\mathrm{A}}\ell^2} = \frac{k_{\mathrm{B}}(T_3 - T_1)}{96\pi\eta\ell^2}, \tag{4.15}$$

where we have used Eq. (4.6).

The above expression is an important result of this letter and deserves further discussion. The average velocity is proportional to the temperature difference $T_3 - T_1$. Since we have assumed $x_1 < x_2 < x_3$, the swimming direction is from a

40

colder sphere to a hotter one, i.e., $\langle V \rangle > 0$ when $T_3 > T_1$ and vice versa. It is also remarkable that Eq. (4.15) does not depend on the temperature T_2 of the middle sphere. Hence $\langle V \rangle = 0$ when $T_1 = T_3$ even though T_1 and T_3 can be different from T_2. However, the presence of the middle sphere is essential for directional locomotion because the hydrodynamic interactions among the three spheres are responsible for it. Notice that a two-sphere micromachine cannot move even if the temperatures are different. This is because, if we keep only the first two terms in Eqs. (4.2) and (4.3) plus the noise terms ξ_1 and ξ_2 for the two spheres, we can immediately see that $\langle \dot{x}_1 + \dot{x}_2 \rangle = \langle \xi_1 \rangle + \langle \xi_2 \rangle = 0$.

Having discussed the simplest symmetric case, we now present the result for general asymmetric cases when $K_A \neq K_B$ ($\lambda \neq 1$). By repeating the same calculation as before, the two spring extensions in Eq. (4.8) now become

$$u_A(\omega) \approx \frac{(2\lambda + i\omega\tau)\xi_1(\omega) - (\lambda + i\omega\tau)\xi_2(\omega) - \lambda\xi_3(\omega)}{-3\lambda - 2(1 + \lambda)i\omega\tau + (\omega\tau)^2}\tau + \mathcal{O}(a), \qquad (4.16)$$

$$u_B(\omega) \approx \frac{\xi_1(\omega) + (1 + i\omega\tau)\xi_2(\omega) - (2 + i\omega\tau)\xi_3(\omega)}{-3\lambda - 2(1 + \lambda)i\omega\tau + (\omega\tau)^2}\tau + \mathcal{O}(a). \qquad (4.17)$$

Then, the average velocity is

$$\langle V(t) \rangle \approx \frac{a}{8\ell^2\tau}\langle \lambda u_B^2(t) - u_A^2(t) + 3(1 - \lambda)u_A(t)u_B(t) \rangle + \mathcal{O}(a^2, u_A^3, u_B^3). \qquad (4.18)$$

The substitution of Eqs. (4.16) and (4.17) into the Fourier-transformed expression of Eq. (4.18) yields the average velocity $\langle V(\omega) \rangle$ similar to Eq. (4.14). By performing the inverse Fourier transform, we finally obtain the general expression for the average velocity:

$$\langle V \rangle = \frac{k_B}{144\pi\eta\ell^2(1 + \lambda)}[(2 - 5\lambda)T_1 - (7 - 7\lambda)T_2 + (5 - 2\lambda)T_3]. \qquad (4.19)$$

When $\lambda = 1$, Eq. (4.19) reduces to Eq. (4.15), as expected. When the three temperatures are identical, i.e., $T_1 = T_2 = T_3$, one can also show that the velocity vanishes, $\langle V \rangle = 0$. This indicates that an elastic three-sphere micromachine can

attain a finite velocity owing to the temperature difference among the spheres, rather than its structural asymmetry.

To confirm our analytical prediction, we performed numerical simulations of the coupled stochastic equations in Eqs. (4.2)–(4.4) when $\lambda = 1$. The equations can be discretized according to Storatonovich interpretation [4.13]. Then, the strength of thermal noise acting on each sphere is determined by a dimensionless parameter $S_i = [2k_B T_i/(K_A \ell^2)]^{1/2}$. We performed simulations for (i) thermally asymmetric nonequilibrium cases in which $S_1 = S_2 = 0$ and $S_3 = 0.2$ or $S_3 = 0.141$, and (ii) a thermally symmetric equilibrium case in which $S_1 = S_2 = S_3 = 0.067$. For comparison, we also performed a simulation for (iii) a thermally asymmetric nonequilibrium two-sphere case in which $S_1 = 0$ and $S_2 = 0.133$ (sphere 3 does not exist). The average over 100 independent runs has been taken for each case.

In Fig. 4.2, we plot the obtained center-of-mass position $X(t) = (x_1 + x_2 + x_3)/3$ as a function of time t. For case (i), we clearly see that a micromachine migrates towards the positive direction with well-defined finite velocities. The dashed lines correspond to the analytical result in Eq. (4.15), which is in good agreement with the numerical simulations. However, a micromachine cannot gain any net displacement for cases (ii) and (iii). Our simulation result clearly demonstrates that a three-sphere micromachine can acquire directional motion because of thermal fluctuations only when the three spheres have different temperatures.

In the above numerical simulations, a three-sphere micromachine undergoes not only ballistic motion but also diffusive motion due to the presence of thermal fluctuations. The crossover time separating these two different regimes can be roughly estimated by the condition $2Dt^* \approx \langle V \rangle^2 t^{*2}$, where the total diffusion coefficient is approximately given by $D \approx k_B \overline{T}/(18\pi\eta a)$ with $\overline{T} = (T_1 + T_2 + T_3)/3$. By denoting the temperature difference in Eq. (4.15) as $\Delta T = T_3 - T_1$, the crossover time is roughly obtained as $t^* \approx D/\langle V \rangle^2 \approx \eta\ell^4 \overline{T}/[ak_B(\Delta T)^2]$. When $S_1 = S_2 = 0$ and $S_3 = 0.2$, for example, we estimate $t^* \approx 300\tau$, which is much smaller than the total simulation time in Fig. 4.2.

4.4 Conclusion

Next, we argue that the analytically obtained velocity in Eqs. (4.15) or (4.19) can be related to the ensemble average of heat flows in the steady state. Within the framework of "stochastic energetics" proposed by Sekimoto [4.13], the heat gained by the i-th sphere per unit time is expressed as

$$\frac{dQ_i}{dt} = 6\pi\eta a(-\dot{x}_i + \xi_i)\dot{x}_i, \tag{4.20}$$

where $\dot{x}_i$ and ξ_i are given by Eqs. (4.2)–(4.4). In the calculation of average heat flows, we also consider terms up to the leading-order contribution of a/ℓ. For example, only the first term on the r.h.s. of Eq. (4.2), $K_A u_A/(6\pi\eta a)$, and the noise term, ξ_1, are taken into account when we eliminate $\dot{x}_1$ in Eq. (4.20). We further use the statistical properties of quantities such as $\langle u_A^2 \rangle$ and $\langle u_A \xi_1 \rangle$, which can be estimated according to Eqs. (4.16) and (4.5).

Then, the lowest-order average heat flows are obtained as

$$\left\langle \frac{dQ_1}{dt} \right\rangle_0 = \frac{k_B}{6(1+\lambda)\tau}[(3+2\lambda)T_1 - (3+\lambda)T_2 - \lambda T_3], \tag{4.21}$$

$$\left\langle \frac{dQ_2}{dt} \right\rangle_0 = \frac{k_B}{6(1+\lambda)\tau}[-(3+\lambda)T_1 + (3+2\lambda+3\lambda^2)T_2 - (\lambda+3\lambda^2)T_3], \tag{4.22}$$

$$\left\langle \frac{dQ_3}{dt} \right\rangle_0 = \frac{k_B}{6(1+\lambda)\tau}[-\lambda T_1 - (\lambda+3\lambda^2)T_2 + (2\lambda+3\lambda^2)T_3], \tag{4.23}$$

which all vanish when $T_1 = T_2 = T_3$. It is also remarkable that the above lowest-order heat flows satisfy [4.12, 4.13]

$$\left\langle \frac{dQ_1}{dt} \right\rangle_0 + \left\langle \frac{dQ_2}{dt} \right\rangle_0 + \left\langle \frac{dQ_3}{dt} \right\rangle_0 = 0. \tag{4.24}$$

Assuming a linear relation between the velocity in Eq. (4.19) and the heat flows

in Eqs. (4.21)-(4.23), we obtain an alternative expression for the velocity:

$$\langle V \rangle = \frac{a}{8K_{\mathrm{A}}\ell^2} \left[\frac{3-5\lambda}{1+\lambda} \left\langle \frac{dQ_1}{dt} \right\rangle_0 + \frac{5-3\lambda}{\lambda(1+\lambda)} \left\langle \frac{dQ_3}{dt} \right\rangle_0 \right]. \qquad (4.25)$$

For the symmetric case of $\lambda = 1$ corresponding to Eq. (4.15), the above expression reduces to

$$\langle V \rangle = \frac{a}{8K_{\mathrm{A}}\ell^2} \left[\left\langle \frac{dQ_3}{dt} \right\rangle_0 - \left\langle \frac{dQ_1}{dt} \right\rangle_0 \right]. \qquad (4.26)$$

This relation indicates that the average velocity is determined by the net heat flow between spheres 1 and 3.

Finally, we briefly comment on previous relevant works. Using coupled Langevin equations, Dunkel and Zaid investigated the interplay between the diffusive and self-driven behaviors of an elastic three-sphere swimmer [4.17]. In this work, however, the temperature of the system was assumed to be uniform. In addition, hydrodynamic simulations of a self-thermophoretic Janus particle were reported in Ref. [4.18] to reproduce the experimental result [4.19]. Again, our model differs from this model because thermal fluctuations of internal degrees of freedom cause the locomotion of an elastic micromachine. We also note from Eq. (4.19) that $\langle V \rangle \neq 0$ for symmetric temperatures $T_1 = T_3 \neq T_2$ as long as the structural asymmetry exists.

In summary, we have shown that an elastic three-sphere micromachine in a viscous fluid can acquire directional motion because of thermal fluctuations when the spheres have different temperatures. We have obtained an expression for the average velocity that is related to the temperatures and average heat flows. Such a mechanism for the locomotion of micromachines is expected to play important roles in nonequilibrium biological systems. In the future, we shall generalize our calculation to the case in which the spheres have different sizes [4.4]. In such a calculation, one needs to take into account higher-order contributions in a and u_{A}, u_{B}. It would be interesting to investigate how these nonlinear contributions affect

44

the nonequilibrium dynamics of thermally driven micromachines.

Bibliography

[4.1] E. Lauga and T. R. Powers, Rep. Prog. Phys. **72** 096601 (2009).

[4.2] E. M. Purcell, Am. J. Phys. **45**, 3 (1977).

[4.3] A. Najafi and R. Golestanian, Phys. Rev. E **69**, 062901 (2004).

[4.4] R. Golestanian and A. Ajdari, Phys. Rev. E **77**, 036308 (2008).

[4.5] J. Pande, L. Merchant, T. Krüger, J. Harting, and A.-S. Smith, New J. Phys. **19**, 053024 (2017).

[4.6] K. Yasuda, Y. Hosaka, M. Kuroda, R. Okamoto, and S. Komura, J. Phys. Soc. Jpn. **86**, 093801 (2017).

[4.7] R. Golestanian and A. Ajdari, Phys. Rev. Lett. **100**, 038101 (2008).

[4.8] R. Golestanian, Phys. Rev. Lett. **105**, 018103 (2010).

[4.9] T. Sakaue, R. Kapral, and A. S. Mikhailov, Eur. Phys. J. B **75**, 381 (2010).

[4.10] M.-J. Huang, H.-Y. Chen, and A. S. Mikhailov, Eur. Phys. J. E **35**, 119 (2012).

[4.11] K. Sekimoto, J. Phys. Soc. Jpn. **66**, 1234 (1997).

[4.12] K. Sekimoto, Prog. Theor. Phys. Suppl. **130**, 17 (1998).

[4.13] K. Sekimoto, *Stochastic Energetics* (Springer, Berlin Heidelberg, 2010).

[4.14] K. Yasuda, R. Okamoto, and S. Komura, J. Phys. Soc. Jpn. **86**, 043801 (2017).

[4.15] M. Doi, *Soft Matter Physics* (Oxford University, Oxford, 2013).

[4.16] A. Y. Grosberg and J.-F. Joanny, Phys. Rev. E **92**, 032118 (2015).

[4.17] J. Dunkel and I. M. Zaid, Phys. Rev. E **80**, 021903 (2009).

[4.18] M. Yang, A. Wysocki, and M. Ripoll, Soft Matter **10**, 6208 (2014).

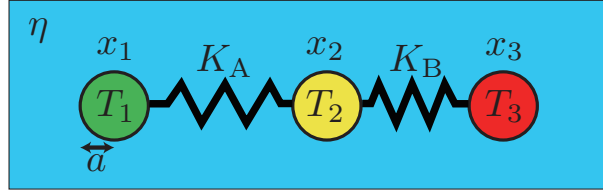[4.19] H.-R. Jiang, N. Yoshinaga, and M. Sano, Phys. Rev. Lett. **105**, 268302 (2010).

Figure 4.1: Thermally driven elastic three-sphere micromachine in a fluid of viscosity η. Three spheres of radius a are connected by two harmonic springs with elastic constants K_A and K_B. The time-dependent positions of the spheres are denoted by $x_i(t)$ $(i = 1, 2, 3)$ in a one-dimensional coordinate system. Importantly, the three spheres are in equilibrium with independent heat baths at temperatures T_i.
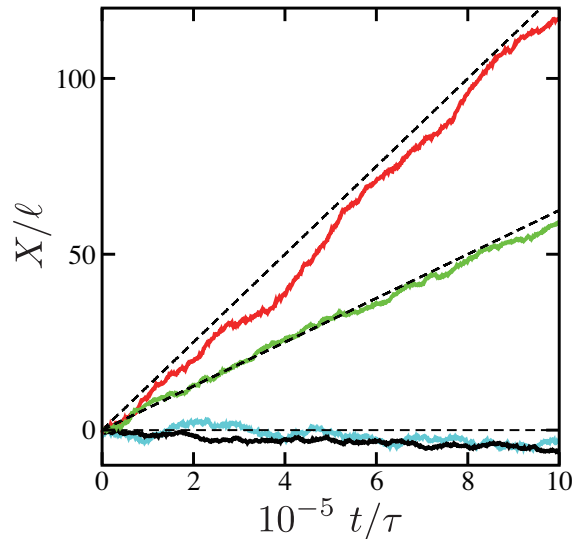
Figure 4.2: Simulations of scaled center-of-mass position X/ℓ of an elastic micromachine as a function of scaled time t/τ when $a/\ell = 0.1$. The strength of thermal noise is $S_i = [2k_B T_i/(K_A \ell^2)]^{1/2}$. Case (i): thermally asymmetric nonequilibrium three-sphere micromachine with $S_1 = S_2 = 0$ and $S_3 = 0.2$ (red) or $S_3 = 0.141$ (green). Case (ii): thermally symmetric equilibrium three-sphere micromachine with $S_1 = S_2 = S_3 = 0.067$ (black). Case (iii): thermally asymmetric nonequilibrium two-sphere micromachine with $S_1 = 0$ and $S_2 = 0.133$ (cyan). The dashed lines are the plots of Eq. (4.15) with the respective parameters.

47

Chapter 5

Anomalous diffusion in viscoelastic media with active force dipoles

With the use of the "two-fluid model", we discuss anomalous diffusion induced by active force dipoles in viscoelastic media. Active force dipoles, such as proteins and bacteria, generate non-thermal fluctuating flows that lead to a substantial increment of the diffusion. Using the partial Green's function of the two-fluid model, we first obtain passive (thermal) two-point correlation functions such as the displacement cross-correlation function between the two point particles separated by a finite distance. We then calculate active (non-thermal) one-point and two-point correlation functions due to active force dipoles. The time correlation of a force dipole is assumed to decay exponentially with a characteristic time scale. We show that the active component of the displacement cross-correlation function exhibits various crossovers from super-diffusive to sub-diffusive behaviors depending on the characteristic time scales and the particle separation. Our theoretical results are intimately related to the microrheology technique to detect fluctuations in non-equilibrium environment.

5.1　Introduction

The cytoplasm of living cells is full of proteins and organelles that play important active roles with the aid of chemical fuels such as adenosine triphosphate (ATP) [5.1]. In such a non-equilibrium environment, the transport properties of chemical species drastically deviate from those in static equilibrium conditions. For example, there are several experimental works reporting the anomalous diffusion of a tagged particle in biological cells due to protein activities [5.2–5.6]. In other systems, a large enhancement of diffusion was also observed for a passive particle immersed in a bacterial bath [5.7, 5.8] or in a suspension of algae Chlamydomonas [5.9], and such a phenomenon has been also studied theoretically [5.10, 5.11].

The modified diffusion in cells was attributed to non-equilibrium forces generated by molecular motors walking on cytoskeletal networks [5.12, 5.13]. Recently, Mikhailov and Kapral proposed a different mechanism caused by non-equilibrium conformational changes of proteins or enzymes [5.14, 5.15]. They showed that, in addition to thermal fluctuations, active proteins in living cells generate non-thermal fluctuating flows that lead to a substantial increment of the diffusion constant. A chemotaxis-like drift of a passive particle was also predicted when a spatial gradient of active proteins is present [5.14, 5.15]. In these previous works, however, the three-dimensional (3D) cytoplasm and two-dimensional (2D) biomembrane were treated as purely viscous fluids characterized by constant shear viscosities [5.16].

In general, biological cells behave as viscoelastic materials [5.17, 5.18]. Hoffman *et al.* experimentally determined the frequency-dependent shear modulus of cultured mammalian cells by using various methods to measure their viscoelastic properties [5.19, 5.20]. Interestingly, they found two universal (weak) power-law dependencies of the shear modulus at low frequencies corresponding to the cortical and intracellular networks. At high frequencies, on the other hand, they observed an exponent of 3/4 which was attributed to the mechanical response of actin fibers.

Such an universal behavior of mechanical responses in living cells was also reported in other work [5.21].

Among various methods, microrheology is one of the most useful techniques to measure the rheological properties of living cells [5.22–5.26]. In this method, the local and bulk mechanical properties of a single cell can be extracted from a Brownian motion of probe particles, including both thermal and non-thermal contributions [5.27]. Concerning its theoretical background, the generalized Stokes-Einstein relation (GSER), equivalent to the fluctuation dissipation theorem (FDT), has been used to analyze thermal diffusive motions. In non-thermal situations, the GSER has been further extended to relate particle mean squared displacement (MSD) and non-thermal force fluctuations [5.28, 5.29]. It should be noted, however, that the GSER contains various assumptions which can be violated in several situations [5.27]. Therefore it is necessary to discuss both thermal and non-thermal Brownian motions in a viscoelastic medium which is described by a well-founded theoretical model.

In this paper, we discuss diffusive motion of passive particles embedded in viscoelastic media that is described by the "two-fluid model" for gels [5.30–5.32]. We especially focus on the effects of non-thermal fluctuations induced by active force dipoles which undergo cyclic motions. We calculate displacement cross-correlation functions (CCF) of two point particles for the passive situation induced by thermal fluctuations and the active situation driven by force dipole fluctuations. Our calculation is closely related to the "two-point microrheology" method which has several technical advantages compared to the "one-point microrheology" [5.33]. As for the stochastic property of a force dipole, we consider the case when there is no correlation between different times, and also the case when it decays exponentially with a characteristic time scale. If the dipole time scale is much larger than the viscoelastic time scale, we show that the active contribution of the displacement CCF exhibits all the possible crossover behaviors between super-diffusive and sub-diffusive motions. Our predictions can be applied not only for cells but also for bacterial suspensions and systems containing active colloids.

Since our theory is based on the standard two-fluid model, it has some similarities to the works by Levine and Lubensky [5.34, 5.35] or MacKintosh and Levine [5.12, 5.13]. In the former studies [5.34, 5.35], they investigated the dynamics of rigid spheres embedded in viscoelastic media by using the two-fluid model, but did not consider the effects of non-thermal fluctuations. In the latter studies [5.12, 5.13], on the other hand, they developed a model for F-actin networks driven out of equilibrium by molecular motors. The main difference in our work is that active force dipoles are embedded in the fluid and exert forces on the fluid itself. In this regard, we use the partial Green's function that connects the force acting on the fluid and the fluid velocity as discussed in Refs. [5.36, 5.37]. In these works, they emphasized the role of the intermediate length scale in the analysis of microrheology data. In our separate work, starting from the two-fluid model, we have derived effective equations of motions for tracer particles displaying local deformations and local fluid flows [5.38].

In the next section, we describe the two-fluid model and show its partial Green's function both in the Fourier space and the real space. In Sec. 5.3, we discuss the passive two-point correlation functions. Using the coupling mobilities and the FDT in thermal equilibrium, we calculate the power spectral density of the velocity CCFs and the displacement CCFs. In Sec. 5.4, we shall investigate active one-point correlation functions due to active force dipoles. We calculate the active velocity auto-correlation function of a passive point particle by assuming different time correlations of force dipoles. We then discuss in Sec. 5.5 the active two-point correlation functions which are useful for two-point microrheology. The summary of our work and some discussions related to the recent experiments are given in Sec. 5.6.
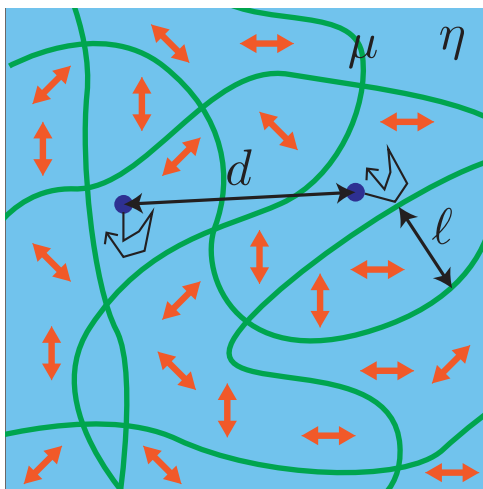
Figure 5.1: Schematic representation of the two-fluid model. The system consists of an elastic network characterized by the Lamé coefficient μ, and a viscous fluid characterized by the shear viscosity η. The elastic and fluid components are coupled through the mutual friction. The length scale ℓ characterizes the typical internal structure of the elastic network. Orange objects represent stochastic force dipoles which are immersed in the fluid component. Two passive point particles separated by a distance d are embedded in the fluid component. These passive particles undergo correlated random Brownian motion due to thermal fluctuations and active stochastic fluctuations induced by active force dipoles.

5.2   Two-fluid model

5.2.1   Model description

To describe viscoelastic media from a general point of view, we employ the two-fluid model that has been broadly used to describe the dynamics of polymer gels [5.30–5.32, 5.39]. As schematically shown in Fig. 5.1, there are two dynamical fields in this model; the displacement field $\mathbf{u}(\mathbf{r}, t)$ of the elastic network and the velocity field $\mathbf{v}(\mathbf{r}, t)$ of the permeating fluid. Here $\mathbf{r}$ is the 3D position vector and t is the time. The coupled dynamical equations for these two field variables are given by

$$\rho_u \frac{\partial^2 \mathbf{u}}{\partial t^2} = \mu \nabla^2 \mathbf{u} + (\mu + \lambda)\nabla(\nabla \cdot \mathbf{u}) - \Gamma\left(\frac{\partial \mathbf{u}}{\partial t} - \mathbf{v}\right) + \mathbf{f}_u, \qquad (5.1)$$

$$\rho_v \frac{\partial \mathbf{v}}{\partial t} = \eta \nabla^2 \mathbf{v} - \nabla p - \Gamma \left(\mathbf{v} - \frac{\partial \mathbf{u}}{\partial t} \right) + \mathbf{f}_v. \tag{5.2}$$

In the above, ρ_u and ρ_v are the mass densities of the two components, μ and λ are the Lamé coefficients of the elastic network, respectively, η is the shear viscosity of the fluid, $p(\mathbf{r}, t)$ is the pressure field, while $\mathbf{f}_u$ and $\mathbf{f}_v$ are external force densities. The elastic and the fluid components are coupled through the mutual friction characterized by the friction coefficient Γ. We note that μ, λ, η and Γ are constants and do not depend on frequency. When the volume fraction of the network is denoted by ϕ, the above equations are further supplemented by the condition of the total volume conservation

$$\nabla \cdot \left[\phi \frac{\partial \mathbf{u}}{\partial t} + (1 - \phi)\mathbf{v} \right] = 0. \tag{5.3}$$

In the following, we employ several simplifications of the model. (i) We neglect inertial effects, which is justified at sufficiently low frequencies. Hence the l.h.s. of Eqs. (5.1) and (5.2) are both neglected. (ii) We assume that the volume fraction of the network is vanishingly small, i.e., $\phi \ll 1$. In this limit, Eq. (5.3) can be approximated as

$$\nabla \cdot \mathbf{v} \approx 0. \tag{5.4}$$

This equation can be regarded as the incompressibility condition of the fluid component.

5.2.2 Partial Green's function

The above linearized equations can be solved by performing the Fourier transform in space and the Laplace transform in time for any function $f(\mathbf{r}, t)$ as defined by

$$f[\mathbf{q}, s] = \int_{-\infty}^{\infty} \mathrm{d}^3 r \int_{0}^{\infty} \mathrm{d}t \, f(\mathbf{r}, t)e^{-i\mathbf{q}\cdot\mathbf{r}-st}. \tag{5.5}$$

Here $\mathbf{q}$ is the 3D wavevector and s the frequency in the Laplace domain. The general Green's function (represented by a 6×6 matrix) connecting $\mathbf{u}$ and $\mathbf{v}$ to $\mathbf{f}_u$ and $\mathbf{f}_v$ was calculated by Levine and Lubensky [5.34, 5.35].

In this paper, we particularly focus on the response of the fluid velocity $\mathbf{v}$ due to the point force $\mathbf{f}_v$, and use the partial Green's function defined by

$$v_\alpha[\mathbf{q}, s] = G_{\alpha\beta}[\mathbf{q}, s] f_{v,\beta}[\mathbf{q}, s]. \tag{5.6}$$

Hereafter, the Einstein summation convention over repeated indices is employed. According to Refs. [5.34–5.37], the Green's function is given by

$$G_{\alpha\beta}[\mathbf{q}, s] = \frac{1 + (\eta_{\mathrm{b}}/\eta)\xi^2 q^2}{\eta_{\mathrm{b}} q^2 (1 + \xi^2 q^2)} \left(\delta_{\alpha\beta} - \hat{q}_\alpha \hat{q}_\beta \right), \tag{5.7}$$

with $q = |\mathbf{q}|$ and $\hat{\mathbf{q}} = \mathbf{q}/q$ (see Appendix 5.A for a detailed derivation). In the above, the frequency-dependent bulk viscosity and characteristic length scale are defined by

$$\eta_{\mathrm{b}} = \eta + \frac{\mu}{s}, \qquad \xi = \left(\frac{\mu\eta}{s\Gamma\eta_{\mathrm{b}}} \right)^{1/2}, \tag{5.8}$$

respectively. Notice that the above 3×3 matrix is nothing but the part of the general 6×6 matrix [5.35]. In order to study the effects of molecular motors that generate forces in the cytoskeleton, one needs to take into account $\mathbf{f}_u$ as discussed in Refs. [5.12, 5.13] and recently by us [5.38]. We note here that the partial Green's function in Eq. (5.7) does not depend on the compressional Lamé coefficient λ, while it appears in the general 6×6 matrix.

The Green's function in Eq. (5.7) can be inverted back from the Fourier space to the real space (but remaining in the Laplace domain). Following the calculation

54

in the Appendix 5.A, we obtain

$$G_{\alpha\beta}[\mathbf{r}, s] = \frac{1}{8\pi\eta r} \left[\left(1 + \frac{1 - \eta_{\mathrm{b}}/\eta}{\eta_{\mathrm{b}}/\eta} \mathcal{G}_1(r/\xi) \right) \delta_{\alpha\beta} + \left(1 + \frac{1 - \eta_{\mathrm{b}}/\eta}{\eta_{\mathrm{b}}/\eta} \mathcal{G}_2(r/\xi) \right) \hat{r}_\alpha \hat{r}_\beta \right].$$

$$(5.9)$$

where $r = |\mathbf{r}|$ and $\hat{\mathbf{r}} = \mathbf{r}/r$. Here we have defined the two scaling functions by

$$\mathcal{G}_1(z) = 1 + \frac{2}{z^2} - 2e^{-z}\left(1 + \frac{1}{z} + \frac{1}{z^2}\right), \qquad (5.10)$$

$$\mathcal{G}_2(z) = 1 - \frac{6}{z^2} + 2e^{-z}\left(1 + \frac{3}{z} + \frac{3}{z^2}\right). \qquad (5.11)$$

In Fig. 5.2, we plot both $\mathcal{G}_1(z)$ and $\mathcal{G}_2(z)$ as a function of $z = r/\xi$. When $\mathcal{G}_1(z) = \mathcal{G}_2(z) = 0$, the Green's function $G_{\alpha\beta}$ is purely determined by η, whereas it is fully described by η_{b} when $\mathcal{G}_1(z) = \mathcal{G}_2(z) = 1$.

5.2.3   Asymptotic expressions

Next we discuss the asymptotic behaviors of the partial Green's function and the scaling functions. We first note that the asymptotic expressions of the scaling functions are given by

$$\mathcal{G}_1(z) \approx \begin{cases} 4z/3 - 3z^2/4, & z \ll 1, \\ 1 + 2/z^2, & z \gg 1, \end{cases} \qquad (5.12)$$

$$\mathcal{G}_2(z) \approx \begin{cases} z^2/4, & z \ll 1, \\ 1 - 6/z^2, & z \gg 1. \end{cases} \qquad (5.13)$$

These asymptotic behaviors are also plotted in Fig. 5.2 by the dotted lines which provide a good approximation especially for $z \gg 1$.

For our later purpose, we focus here on the large scale behavior of the Green's function. For $r \gg \xi$, we obtain

$$G_{\alpha\beta}[\boldsymbol{r}, s] \approx \frac{1}{8\pi\eta r} \frac{s\tau}{1 + s\tau} (\delta_{\alpha\beta} + \hat{r}_\alpha \hat{r}_\beta) - \frac{\ell^2}{4\pi\eta r^3} \frac{1}{(1 + s\tau)^2} (\delta_{\alpha\beta} - 3\hat{r}_\alpha \hat{r}_\beta), \quad (5.14)$$

where we have introduced the characteristic length and time scales as

$$\ell = (\eta/\Gamma)^{1/2}, \qquad \tau = \eta/\mu. \tag{5.15}$$

As argued in Ref. [5.36], the first and the second terms of Eq. (5.14) are proportional to $1/r$ and ℓ^2/r^3, respectively. The competition between these two terms is characterized by the crossover length ℓ.

5.2.4 Coupling mobilities

In the following sections, we shall consider correlated motions of two point particles embedded in the fluid component. For this purpose, we shall introduce the coupling mobility between the two points $M_{\alpha\beta}[r, s]$ that is directly related to the partial Green's function in Eq. (5.9). Since $G_{\alpha\beta}$ is generally expressed as $G_{\alpha\beta} = C_1 \delta_{\alpha\beta} + C_2 \hat{r}_\alpha \hat{r}_\beta$, the "longitudinal" and the "transverse" coupling mobilities are given by $M_{xx} = C_1 + C_2$ and $M_{yy} = C_1$, respectively. Hence they are

$$M_{xx}[r, s] = \frac{1}{4\pi\eta r} \left[1 - \frac{\mathcal{G}_1(z) + \mathcal{G}_2(z)}{2(1 + s\tau)} \right], \tag{5.16}$$

$$M_{yy}[r, s] = \frac{1}{8\pi\eta r} \left[1 - \frac{\mathcal{G}_1(z)}{1 + s\tau} \right], \tag{5.17}$$

where $z = r/\xi = (r/\ell)\sqrt{1 + s\tau}$. We shall use these coupling mobilities in order to calculate various correlation functions in the next sections. Since $M_{xy} = 0$ by symmetry, it is sufficient to consider only the above two coupling mobilities [5.36].

5.3 Passive two-point correlation functions

Here we discuss the correlated dynamics of two distinctive passive particles immersed in a viscoelastic gel that is in thermal equilibrium. This situation is relevant to the "two-point microrheology" experiments as discussed before [5.33]. Compared to the "single-particle microrheology" (with the use of a finite size particle), there are several advantages to perform multi-particle microrheology [5.27].

5.3.1 Fluctuation dissipation theorem

Consider a pair of point particles undergoing Brownian motion separated by a distance d as shown in Fig. 5.1 (but without force dipoles). We denote the positions of these two point particles by $\mathbf{R}_1(t) = \mathbf{R}_1 + \Delta\mathbf{R}_1(t)$ and $\mathbf{R}_2(t) = \mathbf{R}_2 + \Delta\mathbf{R}_2(t)$, where $d = |\mathbf{R}_2 - \mathbf{R}_1|$. Then the velocities of these point particles are given by $\mathbf{V}_1(\mathbf{R}_1, t) = \Delta\dot{\mathbf{R}}_1(t)$ and $\mathbf{V}_2(\mathbf{R}_2, t) = \Delta\dot{\mathbf{R}}_2(t)$. The quantities of interest are the velocity cross-correlation function (CCF) $\langle V_{1\alpha} V_{2\alpha'}(t) \rangle_d$, and the displacement CCF $\langle \Delta R_{1\alpha} \Delta R_{2\alpha'}(t) \rangle_d$. Without loss of generality, we define the x-axis to be along the line connecting the two particles, i.e., $\mathbf{R}_2 - \mathbf{R}_1 = d\hat{\mathbf{e}}_x$.

According to the fluctuation dissipation theorem (FDT), the velocity CCFs in thermal equilibrium are related to the coupling mobility in the Laplace domain by [5.27, 5.36]

$$\langle V_{1\alpha} V_{2\alpha'}[s] \rangle_d = k_{\mathrm{B}} T M_{\alpha\alpha'}[r = d, s], \tag{5.18}$$

where k_{B} is the Boltzmann constant, T the temperature. The power spectral density (PSD) of the passive velocity CCF can be obtained by using the relation

$$\langle V_{1\alpha} V_{2\alpha'}(\omega) \rangle_d = 2\Re \langle V_{1\alpha} V_{2\alpha'}[s = i\omega] \rangle_d, \tag{5.19}$$

where ω is the frequency in the Fourier domain, and $\Re$ indicates the real part.

In Fig. 5.3, we plot the scaled PSDs $\langle V_{1x} V_{2x}(\omega) \rangle_d$ and $\langle V_{1y} V_{2y}(\omega) \rangle_d$ as a function of $\omega\tau$ using the longitudinal and the transverse coupling mobilities obtained in Eqs. (5.16) and (5.17), respectively. Different colors represent different distances,

d, between the two points. In Fig. 5.3(a), $\langle V_{1x} V_{2x}(\omega) \rangle_d$ increases for $\omega\tau > \sqrt{2}(\ell/d)$ as $\sim \omega^2$ [see later Eqs. (5.21) and (5.22)], while it saturates for $\omega\tau > 1$. Since $\langle V_{1y} V_{2y}(\omega) \rangle_d$ takes negative values for smaller $\omega\tau$ when $d/\ell = 10$ and 100, we have plotted its absolute value in Fig. 5.3(b). Notice that in both (a) and (b), the PSDs are scaled by $k_{\rm B}T/(2\pi\eta d)$, and take the same asymptotic value in the large $\omega\tau$ limit.

The passive displacement CCF in thermal equilibrium as a function of time can be directly obtained by the following inverse Laplace transform of the velocity CCF [5.26, 5.27]:

$$\langle \Delta R_{1\alpha} \Delta R_{2\alpha'}(t) \rangle_d = \frac{1}{2\pi i} \int_{c-i\infty}^{c+i\infty} {\rm d}s\, \frac{2}{s^2} \langle V_{1\alpha} V_{2\alpha'}[s] \rangle_d e^{st}, \qquad (5.20)$$

where c is a real number. Performing the numerical inverse Laplace transform of Eq. (5.20), we plot in Fig. 5.4 the longitudinal and the transverse CCFs $\langle \Delta R_{1x} \Delta R_{2x}(t) \rangle_d$ and $\langle \Delta R_{1y} \Delta R_{2y}(t) \rangle_d$ as a function of t/τ for different distances d between the two points.

In Fig. 5.4(a), the longitudinal CCF is proportional to t for $t/\tau < 1$ and $t/\tau > (d/\ell)^2/2$ [see later Eq. (5.23)]. In the former time region which is smaller than the viscoelastic time scale $\tau = \eta/\mu$, the two point particles interact through the fluid component of the two-fluid model. In the latter long time region, on the other hand, the CCF obeys the normal diffusive behavior as expected for any viscoelastic material with a characteristic relaxation time. Between these crossover time scales, the CCF remains almost constant due to the elastic component that suppresses the motion of the point particles. This is because the elastic property of the medium, representing the polymer network, is pronounced in these time scales. For $d/\ell = 1$, on the other hand, the CCF is almost proportional to t during the entire time region.

In Fig. 5.4(b), the absolute value of $\langle \Delta R_{1y} \Delta R_{2y}(t) \rangle_d$ is plotted because it takes negative values for larger t. This means that the relative transverse motion of the two point particles is anti-correlated when their separation d/ℓ is large enough.

Nevertheless, the general time-dependent behavior of the transverse CCF is almost the same as that of the longitudinal one in (a).

The crossover behaviors of the passive displacement CCF for large d/ℓ showing the successive scaling as $t \to t^0 \to t$ can explain some of the apparent power-law behaviors of soft matter [5.40] or biological cells [5.20]. It should be noted, however, that the passive displacement CCF in thermal equilibrium exhibits only a sub-diffusive behavior.

5.3.2 Large distance behaviors

In the limit of large distances $d \gg \ell$ between the two points, we can use Eq. (5.14) for the partial Green's function to obtain the PSDs in the Fourier domain as

$$\langle V_{1x} V_{2x}(\omega) \rangle_d \approx \frac{k_{\mathrm{B}}T}{2\pi\eta d} \frac{(\omega\tau)^2}{1 + (\omega\tau)^2} + \frac{k_{\mathrm{B}}T\ell^2}{\pi\eta d^3} \left[\frac{1}{[1 + (\omega\tau)^2]^2} - \frac{(\omega\tau)^2}{[1 + (\omega\tau)^2]^2} \right], \quad (5.21)$$

$$\langle V_{1y} V_{2y}(\omega) \rangle_d \approx \frac{k_{\mathrm{B}}T}{4\pi\eta d} \frac{(\omega\tau)^2}{1 + (\omega\tau)^2} - \frac{k_{\mathrm{B}}T\ell^2}{2\pi\eta d^3} \left[\frac{1}{[1 + (\omega\tau)^2]^2} - \frac{(\omega\tau)^2}{[1 + (\omega\tau)^2]^2} \right]. \quad (5.22)$$

For the large distance behavior of the displacement CCFs, we obtain

$$\langle \Delta R_{1x} \Delta R_{2x}(t) \rangle_d \approx \frac{k_{\mathrm{B}}T\tau}{2\pi\eta d} (1 - e^{-t/\tau}) + \frac{k_{\mathrm{B}}T\tau\ell^2}{\pi\eta d^3} \left[\frac{t}{\tau}(1 + e^{-t/\tau}) - 2(1 - e^{-t/\tau}) \right],$$
$$(5.23)$$

$$\langle \Delta R_{1y} \Delta R_{2y}(t) \rangle_d \approx \frac{k_{\mathrm{B}}T\tau}{4\pi\eta d} (1 - e^{-t/\tau}) - \frac{k_{\mathrm{B}}T\tau\ell^2}{2\pi\eta d^3} \left[\frac{t}{\tau}(1 + e^{-t/\tau}) - 2(1 - e^{-t/\tau}) \right].$$
$$(5.24)$$

In the above expressions, the first term is proportional to t in the short time regime, whereas it saturates in the long time limit. Whereas the second term in each expression is proportional to t in the long time limit, which dominates the large scale behavior. These properties of the displacement CCF can be clearly

observed in Fig. 5.4 especially for larger d/ℓ. Although not plotted, Eqs. (5.23) and (5.24) almost completely recover the numerical plots in Fig. 5.4.

5.4 Active one-point correlation functions

In this section, we shall consider the collective advection effects due to active force dipoles on passive particles immersed in viscoelastic media. A simple "dimer model" for a stochastic hydrodynamic force dipole was previously discussed in Refs. [5.14, 5.15]. To investigate the hydrodynamic effects of the force dipoles, we employ the partial Green's function representing the response of the fluid velocity $\mathbf{v}$ due to the force $\mathbf{f}_v$ acting on the fluid component [see Eq. (5.6)]. This is different from Refs. [5.12, 5.13] where they discussed the effects of molecular motors generating forces in the cytoskeleton which corresponds to the elastic component of the two-fluid model. Our aim is to focus on the role of active force dipoles that exist in the fluid component. A more unified treatment of these two different sources of active forces has been investigated in our separate publication [5.38].

5.4.1 Velocity induced by active force dipoles

When a point force $\mathbf{f}_v$ is applied to the fluid at a point $\mathbf{r}$, it induces a fluid velocity at another position $\mathbf{R}$ that advects a point particle located there. As in the previous section, we denote the position of this passive point particle by $\mathbf{R}(t) = \mathbf{R}_0 + \Delta\mathbf{R}(t)$, and its velocity by $\mathbf{V}(\mathbf{R}, t) = \Delta\dot{\mathbf{R}}(t)$. Using the Green's function calculated in Sec. 5.2, we obtain the relation between $\mathbf{V}$ and $\mathbf{f}_v$ as

$$V_\alpha(\mathbf{R}, t) = \int_{-\infty}^{t} dt' \, G_{\alpha\beta}(\mathbf{R} - \mathbf{r}, t - t') f_{v,\beta}(\mathbf{r}, t'). \tag{5.25}$$

Consider an oscillating dimer of length $a(t)$ and the force magnitude $f_d(t)$ with its orientation given by the unit vector $\hat{\mathbf{e}}$. In this case, the induced velocity of a

passive particle at $\mathbf{R}$ due to the oscillating dimer is given by [5.14]

$$V_\alpha(\mathbf{R}, t) \approx \int_{-\infty}^{t} dt' \frac{\partial G_{\alpha\beta}(\mathbf{R} - \mathbf{r}, t - t')}{\partial r_\gamma} \hat{e}_\beta \hat{e}_\gamma m(t'), \tag{5.26}$$

where we have used the approximation $a \ll |\mathbf{R} - \mathbf{r}|$, and $m(t) = a(t)f_d(t)$ denotes the magnitude of the force dipole.

We further consider a collection of such active force dipoles, located at positions $\{\mathbf{R}_i\}$ with orientations $\{\hat{\mathbf{e}}_i\}$. By summing up for all the dipoles, the velocity of the passive particle is then given by [5.14]

$$V_\alpha(\mathbf{R}_0, t) \approx \int_{-\infty}^{t} dt' \int d^3r \frac{\partial G_{\alpha\beta}(\mathbf{r}, t - t')}{\partial r_\gamma} \sum_i \hat{e}_{i,\gamma} \hat{e}_{i,\beta} m_i(t') \delta(\mathbf{R}_i - \mathbf{R}_0 - \mathbf{r}),$$

$$\tag{5.27}$$

where we have assumed that the displacement of the passive particle is small, and kept only the lowest order term. This equation describes the motion of a passive point particle due to non-thermal active noise arising from the collective operation of active force dipoles.

Hereafter we introduce the bilateral Fourier transform in time for any function $f(t)$ as

$$f(\omega) = \int_{-\infty}^{\infty} dt \, f(t) e^{-i\omega t}, \tag{5.28}$$

[cf. Eq. (5.5)]. Performing the bilateral Fourier transform of Eq. (5.27), we obtain

$$V_\alpha(\mathbf{R}_0, \omega) \approx \int d^3r \frac{\partial G_{\alpha\beta}[\mathbf{r}, \omega]}{\partial r_\gamma} \sum_i \hat{e}_{i,\gamma} \hat{e}_{i,\beta} m_i(\omega) \delta(\mathbf{R}_i - \mathbf{R}_0 - \mathbf{r}), \tag{5.29}$$

where $G_{\alpha\beta}[\mathbf{r}, \omega] = G_{\alpha\beta}[\mathbf{r}, s = i\omega]$. We shall use this expression to calculate the velocity correlation functions and the mean squared displacement (MSD) of the passive particle.

5.4.2 Active auto-correlation functions

We now calculate the velocity auto-correlation function (ACF) of a passive particle located on average at $\mathbf{R}_0$. If the correlation between different force dipoles vanishes, i.e., $\langle m_i m_j(\omega) \rangle = \langle m^2(\omega) \rangle \delta_{ij}$, we get from Eq. (5.29)

$$
\begin{aligned}
&\langle V_\alpha V_{\alpha'}(\mathbf{R}_0, \omega) \rangle \\
&= \int \mathrm{d}^3 r \, \frac{\partial G_{\alpha\beta}[\mathbf{r}, \omega]}{\partial r_\gamma} \frac{\partial G_{\alpha'\beta'}[\mathbf{r}, -\omega]}{\partial r_{\gamma'}} \sum_i \langle \hat{e}_{i,\gamma} \hat{e}_{i,\beta} \hat{e}_{i,\gamma'} \hat{e}_{i,\beta'} \rangle \langle m_i^2(\omega) \rangle \langle \delta(\mathbf{R}_i - \mathbf{R}_0 - \mathbf{r}) \rangle \\
&= \Omega_{\beta\beta'\gamma\gamma'} \langle m^2(\omega) \rangle \int \mathrm{d}^3 r \, \frac{\partial G_{\alpha\beta}[\mathbf{r}, \omega]}{\partial r_\gamma} \frac{\partial G_{\alpha'\beta'}[\mathbf{r}, -\omega]}{\partial r_{\gamma'}} c(\mathbf{R}_0 + \mathbf{r}),
\end{aligned}
\tag{5.30}
$$

where $c(\mathbf{r}) = \sum_i \langle \delta(\mathbf{R}_i - \mathbf{r}) \rangle$ is the local concentration of force dipoles at a point $\mathbf{r}$ in the fluid component. In the above, a symbol

$$
\begin{aligned}
\Omega_{\beta\beta'\gamma\gamma'} &= \langle \hat{e}_\beta \hat{e}_{\beta'} \hat{e}_\gamma \hat{e}_{\gamma'} \rangle \\
&= \frac{1}{15} (\delta_{\beta\beta'} \delta_{\gamma\gamma'} + \delta_{\beta\gamma} \delta_{\beta'\gamma'} + \delta_{\beta\gamma'} \delta_{\beta'\gamma}),
\end{aligned}
\tag{5.31}
$$

has been defined, and we have assumed that the orientations of active force dipoles are not correlated with their positions. In other words, we do not consider any nematic ordering of force dipoles [5.14].

When active force dipoles are uniformly distributed in space with a constant concentration, $c(\mathbf{r}) = c_0$, the velocity ACF $\langle V_\alpha V_{\alpha'}(\omega) \rangle$ is isotropic, i.e., $\langle V_x^2(\omega) \rangle = \langle V_y^2(\omega) \rangle = \langle V_z^2(\omega) \rangle$ and vanishes otherwise. Hence it is enough to consider only the x-direction, and we obtain the active PSD as

$$
\begin{aligned}
\langle V_x^2(\omega) \rangle &= \frac{c_0}{3} \Omega_{\beta\beta'\gamma\gamma'} \langle m^2(\omega) \rangle \int \mathrm{d}^3 r \, \frac{\partial G_{\alpha\beta}[\mathbf{r}, \omega]}{\partial r_\gamma} \frac{\partial G_{\alpha\beta'}[\mathbf{r}, -\omega]}{\partial r_{\gamma'}} \\
&= \frac{1}{3 \cdot 8^2 \cdot 15\pi^2} \frac{c_0}{\eta^2 \ell} \langle m^2(\omega) \rangle \mathcal{I}(\omega).
\end{aligned}
\tag{5.32}
$$

Here we have introduced the scaled PSD defined by

$$\mathcal{I}(\omega) = 15\Omega_{\beta\beta'\gamma\gamma'} \int \mathrm{d}^3\bar{r}\, \frac{\partial g_{\alpha\beta}[\mathbf{r},\omega]}{\partial\bar{r}_\gamma} \frac{\partial g_{\alpha\beta'}[\mathbf{r},-\omega]}{\partial\bar{r}_{\gamma'}}, \tag{5.33}$$

together with $g_{\alpha\beta}[\mathbf{r},\omega] = 8\pi\eta\ell G_{\alpha\beta}[\mathbf{r}, s = i\omega]$ and $\bar{r} = r/\ell$. Since the above integral diverges for short length scales, we need to introduce a small cutoff length δ. Physically, δ can be regarded as the size of the passive particle. In Fig. 5.5, we numerically plot the scaled PSD, $\mathcal{I}(\omega)$, as a function of $\omega\tau$ for different cutoff lengths $\delta/\ell = 1$, 10 and 100. These values correspond to the situation when the passive particle is larger than the mesh size. For $\omega\tau > 2\sqrt{3}(\ell/\delta)^2$, the PSD increases as $\sim \omega^2$ and saturates for $\omega\tau > 1$ [see later Eq. (5.34)]. Note that the asymptotic value of the scaled PSD for large $\omega\tau$ is independent of δ.

If we use Eq. (5.14) for the partial Green's function $G_{\alpha\beta}$ in the large distance limit $r \gg \ell$, the scaled PSD can be approximately calculated as

$$\mathcal{I}(\omega) \approx 48\pi \left[\frac{(\omega\tau)^2}{1+(\omega\tau)^2} \left(\frac{\ell}{\delta}\right) - \frac{4(\omega\tau)^2}{[1+(\omega\tau)^2]^2} \left(\frac{\ell}{\delta}\right)^3 + \frac{12}{[1+(\omega\tau)^2]^2} \left(\frac{\ell}{\delta}\right)^5 \right]. \tag{5.34}$$

The detailed derivation of this expression is given in the Appendix 5.B. Although not plotted, we have confirmed that Eq. (5.34) perfectly reproduces the curve of $\delta/\ell = 100$ in Fig. 5.5. We should keep in mind, however, that to regard the cutoff length δ as the particle size is only an approximation, and hence the numerical prefactor should not be taken as accurate when we compare with experiments.

5.4.3 Uncorrelated force dipoles

In order to further calculate the active PSD, the statistical property for the time correlation of a force dipole needs to be specified. First we assume that it is only δ-correlated in time and is given by

$$\langle m(t)m(t')\rangle = S\delta(t-t'), \tag{5.35}$$

where S fixes the fluctuation amplitude. In the Fourier representation, this simply means that $\langle m^2(\omega) \rangle = S$. Once we know the active PSD of the velocity ACF, the corresponding MSD of a passive particle in the x-direction can be obtained by the inverse Fourier transform:

$$\langle (\Delta R_x)^2(t) \rangle = \int_{-\infty}^{\infty} \frac{d\omega}{2\pi} \frac{2}{(i\omega)^2} \langle V_x^2(\omega) \rangle e^{i\omega t}. \tag{5.36}$$

In contrast to the inverse Laplace transform in Eq. (5.20), we also take into account the initial condition by including a constant term in the above transformation. In Fig. 5.6(a), we numerically plot the scaled $\langle (\Delta R_x)^2(t) \rangle$ as a function of t/τ for $\delta/\ell = 1$, 10 and 100. Here the MSD is proportional to t both for short time scales $t/\tau < 1$ and for long time scales $t/\tau > (\delta/\ell)^4/12$ [see later Eq. (5.38)]. For the intermediate time range $1 < t/\tau < (\delta/\ell)^4/12$, on the other hand, the MSD is strongly suppressed due to the elastic component of the two-fluid model, and it remains almost constant.

If we use the asymptotic expression Eq. (5.14) for the partial Green's function as before, the PSD can be obtained from Eqs. (5.32) and (5.34) as

$$\langle V_x^2(\omega) \rangle \approx \frac{1}{60\pi} \frac{c_0 S}{\eta^2 \ell} \left[\frac{(\omega\tau)^2}{1+(\omega\tau)^2} \left(\frac{\ell}{\delta} \right) - \frac{4(\omega\tau)^2}{[1+(\omega\tau)^2]^2} \left(\frac{\ell}{\delta} \right)^3 + \frac{12}{[1+(\omega\tau)^2]^2} \left(\frac{\ell}{\delta} \right)^5 \right]. \tag{5.37}$$

Then, with the use of Eq. (5.36), the asymptotic MSD can be analytically obtained as

$$\langle (\Delta R_x)^2(t) \rangle \approx \frac{1}{60\pi} \frac{c_0 S \tau}{\eta^2 \ell} \left[(1 - e^{-t/\tau}) \left(\frac{\ell}{\delta} \right) + 2[e^{-t/\tau}(t/\tau + 1) - 1] \left(\frac{\ell}{\delta} \right)^3 \right.$$
$$\left. + 6[e^{-t/\tau}(t/\tau + 3) + 2t/\tau - 3] \left(\frac{\ell}{\delta} \right)^5 \right]. \tag{5.38}$$

The first term in the r.h.s. of the above equation indicates that the normal diffusion occurs for the short time scale $t \ll \tau$, while it saturates in the longer times. In

the long time limit, on the other hand, we can set $e^{-t/\tau} \approx 0$, and one finds that MSD is proportional to t for $t \gg (\delta/\ell)^4/12$ [see the third line of Eq. (5.38)], as mentioned above.

5.4.4 Exponentially correlated force dipoles

Next we calculate the PSD and the MSD when the time correlation of a force dipole decays exponentially with a characteristic relaxation time τ_d, i.e.,

$$\langle m(t)m(t')\rangle = \frac{S}{2\tau_d}e^{-|t-t'|/\tau_d}. \tag{5.39}$$

In this case, we have $\langle m^2(\omega)\rangle = S/[1+(\omega\tau_d)^2]$ in the Fourier representation. Some justification of the above simple expression will be separately discussed in Sec. 5.6. Mathematically, Eq. (5.39) reduces to Eq. (5.35) in the limit of $\tau_d \to 0$. Then the active PSD is given by

$$\langle V_x^2(\omega)\rangle = \frac{1}{2880\pi^2}\frac{c_0 S}{\eta^2\ell}\frac{1}{1+(\omega\tau_d)^2}\mathcal{I}(\omega), \tag{5.40}$$

where $\mathcal{I}(\omega)$ was defined before in Eq. (5.33).

In Fig. 5.6(b), we numerically plot the scaled $\langle(\Delta R_x)^2(t)\rangle$ as a function of t/τ when $\tau_d/\tau = 100$ for $\delta/\ell = 1$, 10 and 100, i.e., the distance between the two points is larger than the mesh size. For $\delta/\ell = 1$, we find that the active MSD is proportional to t^2 and exhibits a super-diffusive behavior within the time region $t < \tau_d$. For $\delta/\ell = 100$, such a super-diffusive behavior is observed only up to the viscoelastic time scale $t/\tau < 1$, and the MSD exhibits a normal diffusive behavior for $t/\tau > 1$. The active MSD for $\delta/\ell = 100$ is further suppressed for larger time scales. In the very long time limit, the active MSD will be again proportional to t [5.38].

Using the asymptotic expression Eq. (5.14), the active PSD is now given by

$$\langle V_x^2(\omega)\rangle \approx \frac{1}{60\pi} \frac{c_0 S}{\eta^2 \ell} \frac{1}{1+(\omega\tau_\mathrm{d})^2} \left[\frac{(\omega\tau)^2}{1+(\omega\tau)^2} \left(\frac{\ell}{\delta}\right) \right.$$
$$\left. - \frac{4(\omega\tau)^2}{[1+(\omega\tau)^2]^2} \left(\frac{\ell}{\delta}\right)^3 + \frac{12}{[1+(\omega\tau)^2]^2} \left(\frac{\ell}{\delta}\right)^5 \right]. \tag{5.41}$$

Then the corresponding active one-point MSD can be obtained up to the lowest order in ℓ/δ as

$$\langle (\Delta R_x)^2(t)\rangle \approx \frac{1}{60\pi} \frac{c_0 S\tau}{\eta^2 \ell} \frac{1}{1+\tau_\mathrm{d}/\tau} \left[1 + \frac{(\tau_\mathrm{d}/\tau)e^{-t/\tau_\mathrm{d}}}{1-\tau_\mathrm{d}/\tau} - \frac{e^{-t/\tau}}{1-\tau_\mathrm{d}/\tau}\right] \left(\frac{\ell}{\delta}\right). \tag{5.42}$$

This equation reduces to the first line of Eq. (5.38) in the limit of $\tau_\mathrm{d} \to 0$. By Taylor expanding the above expression for small t, one can indeed show that the linear term in t vanishes, and the active MSD increases as $\sim t^2$. The full expression of the active one-point MSD including higher order terms is provided in the Appendix 5.C. The analytic expressions in Eqs. (5.41) and (5.42) are the general and important results of this paper.

5.5 Active two-point correlation functions

5.5.1 Velocity cross-correlation functions

In this section, we consider the active velocity CCF between the two points at $\mathbf{R}_1$ and $\mathbf{R}_2$ that are separated by a distance d, as shown in Fig. 5.1 and also discussed in Sec. 5.3. With the use of Eq. (5.27), the active two-point velocity CCF can be

evaluated by

$$
\begin{aligned}
&\langle V_{1\alpha} V_{2\alpha'}(\mathbf{R}_1, \mathbf{R}_2, \omega)\rangle_d \\
&= \int \mathrm{d}^3 r \frac{\partial G_{\alpha\beta}[\mathbf{r}, \omega]}{\partial r_\gamma} \left(\frac{\partial G_{\alpha'\beta'}[\mathbf{r}', -\omega]}{\partial r'_{\gamma'}} \right)_{\mathbf{r}'=\mathbf{r}-(\mathbf{R}_2-\mathbf{R}_1)} \\
&\quad \times \sum_i \langle \hat{e}_{i,\gamma} \hat{e}_{i,\beta} \hat{e}_{i,\gamma'} \hat{e}_{i,\beta'} \rangle \langle m_i^2(\omega)\rangle \langle \delta(\mathbf{R}_i - \mathbf{R}_1 - \mathbf{r})\rangle \\
&= \Omega_{\beta\beta'\gamma\gamma'} \langle m^2(\omega)\rangle \\
&\quad \times \int \mathrm{d}^3 r \frac{\partial G_{\alpha\beta}[\mathbf{r}, \omega]}{\partial r_\gamma} \left(\frac{\partial G_{\alpha'\beta'}[\mathbf{r}', -\omega]}{\partial r'_{\gamma'}} \right)_{\mathbf{r}'=\mathbf{r}-(\mathbf{R}_2-\mathbf{R}_1)} \\
&\quad \times c(\mathbf{R}_1 + \mathbf{r}).
\end{aligned}
\tag{5.43}
$$

As before, we can generally set $\mathbf{R}_2 - \mathbf{R}_1 = d\hat{\mathbf{e}}_x$ without loss of generality. We also assume that the active force dipoles are uniformly distributed in space with a constant concentration, c_0. Then one can further rewrite as

$$
\langle V_{1\alpha} V_{2\alpha'}(\omega)\rangle_d = \frac{1}{8^2 \cdot 15\pi^2} \frac{c_0}{\eta^2 \ell} \langle m^2(\omega)\rangle \mathcal{I}_{\alpha\alpha'}(d, \omega),
\tag{5.44}
$$

where

$$
\mathcal{I}_{\alpha\alpha'}(d, \omega) = 15\Omega_{\beta\beta'\gamma\gamma'} \int \mathrm{d}^3 \bar{r} \frac{\partial g_{\alpha\beta}[\mathbf{r}, \omega]}{\partial \bar{r}_\gamma} \left(\frac{\partial g_{\alpha'\beta'}[\mathbf{r}', -\omega]}{\partial \bar{r}_{\gamma'}} \right)_{\mathbf{r}'=\mathbf{r}-\mathbf{d}},
\tag{5.45}
$$

with $g_{\alpha\beta} = 8\pi\eta\ell G_{\alpha\beta}$ as defined before.

In Fig. 5.7, we numerically plot the scaled active PSDs $\langle V_{1x} V_{2x}(\omega)\rangle_d$ and $\langle V_{1y} V_{2y}(\omega)\rangle_d$ as a function of $\omega\tau$ for different distances $d/\ell = 1.1$, 10 and 100, as before. (The reason that we chose here $d/\ell = 1.1$ is that there was a numerical stability issue exactly at $d/\ell = 1$.) The PSD increases as $\sim \omega^2$ for the intermediate frequency range. Within the lowest order term in Eq. (5.14), the asymptotic

expressions of the active PSDs can be obtained as

$$\mathcal{I}_{xx}(d,\omega) \approx \frac{16\pi\ell}{d} \frac{(\omega\tau)^2}{1+(\omega\tau)^2}, \tag{5.46}$$

$$\mathcal{I}_{yy}(d,\omega) = \mathcal{I}_{zz}(d,\omega) \approx \frac{8\pi\ell}{d} \frac{(\omega\tau)^2}{1+(\omega\tau)^2}. \tag{5.47}$$

5.5.2 Displacement cross-correlation functions

Performing the inverse Fourier transform of the active two-point PSDs as before [see Eq. (5.36)], we obtain the corresponding longitudinal and transverse displacement CCFs $\langle \Delta R_{1x} \Delta R_{2x}(t) \rangle_d$ and $\langle \Delta R_{1y} \Delta R_{2y}(t) \rangle_d$ for the distances $d/\ell = 1.1$, 10 and 100. In Fig. 5.8(a) and (b), we plot these quantities when the time correlation of a force dipole is δ-correlated as assumed in Eq. (5.35). Fig. 5.8 should be compared with Fig. 5.6(a) where we have shown the MSD for the active one-point case. Both longitudinal and transverse displacement CCFs are proportional to t for short time scales $t/\tau < 1$ and also for longer time scales. For the intermediate time range, however, these CCFs are strongly suppressed and become constant due to the elastic component of the two-fluid model.

In Fig. 5.9(a) and (b), on the other hand, we consider the case when the time correlation of a force dipole is characterized by a relaxation time $\tau_{\mathrm{d}}/\tau = 100$ [see Eq. (5.39)]. These figures should be compared with Fig. 5.6(b) because the overall behavior is similar. For $\delta/\ell = 1.1$, the active displacement CCFs are proportional to t^2 when $t < \tau_{\mathrm{d}}$, showing a strong super-diffusive behavior. For $\delta/\ell = 100$, however, this super-diffusive behavior is observed only within the time region smaller than the viscoelastic time scale, $t/\tau < 1$, and the CCFs increase as $\sim t$ for $t/\tau > 1$. For much longer time scales, the active CCFs are further suppressed because of the elasticity. In the long time limit, the active CCFs are both proportional to t.

5.6　Summary and discussion

In this paper, we have discussed anomalous diffusion induced by active force dipoles in viscoelastic media that is described by the standard two-fluid model for gels. We first reviewed the two-fluid model and showed its partial Green's function both in the Fourier and the real spaces. With the use of the coupling mobilities and the FDT in thermal equilibrium, we have calculated the PSD of the velocity CCFs and the displacement CCFs between the two point particles both for the longitudinal and the transverse directions. The obtained results are useful to interpret the data obtained by two-point microrheology experiments. The passive (thermal) two-point CCF increases linearly with time at shorter and longer time scales, while it is suppressed and remains almost constant at intermediate time scales (see Fig. 5.4).

Moreover, we have calculated active (non-thermal) one-point and two-point correlation functions due to active force dipoles. We have used the relation between the velocity and the dipole strength, as given by Eq. (5.26), and the formulation in Ref. [5.14] in order to further calculate the active PSD of the velocity CCFs. For the one-point case, one needs to introduce a cutoff length scale, δ, in evaluating the integrals, whereas a finite distance, d, between the two point particles plays the role of the cutoff length in the two-point case. As for the statistical property of force dipoles, we considered the case when their magnitude is uncorrelated in time [see Eq. (5.35)] and the case when it decays exponentially with a characteristic time τ_{d} [see Eq. (5.39)].

For the active case, the important results can be summarized as follows. As shown in Fig. 5.6(b) (one-point case) or Fig. 5.9 (two-point case), we have found that the active MSD or the displacement CCFs exhibits various crossovers from super-diffusive to sub-diffusive behaviors depending on the characteristic time scales ($\tau = \eta/\mu$ and τ_{d}) and the particle separation d (or the cutoff length δ for the one-point case). We emphasize that the active displacement CCF is proportional to t^2 for time scales shorter than the viscoelastic time scale, $t < \tau$, and

69

it is proportional to t for the intermediate time scales, $\tau < t < \tau_\mathrm{d}$. Within the present model, the passive contribution only describes sub-diffusion, whereas the active contribution is responsible for both sub-diffusion and super-diffusion. Our results are useful in understanding active properties of the cytoplasm using force spectrum microscopy combined with the microrheology experiment [5.6], as further discussed below.

In Ref. [5.6], Guo *et al.* measured the MSD of microinjected tracer particles in mellanoma cells. They showed that the MSD was nearly constant at shorter time scales ($t < 0.1$ s), while it exhibited a slightly super-diffusive behavior at longer time scales ($t > 0.1$ s), i.e., $\langle (\Delta R)^2 \rangle \sim t^\beta$ with $\beta \approx 1.2$. However, when they inhibited motor and polymerization activity by depleting cells of ATP, the MSD was almost constant in time, i.e., $\beta \approx 0$. Such an ATP-dependent Brownian motion was also observed in prokaryotic cells and yeast [5.4, 5.5]. In addition to the MSD measurement, Guo *et al.* performed active microrheology experiment [5.24, 5.25], and found that the frequency-dependent elastic modulus follows a power-law form, i.e., $|G(\omega)| \sim \omega^\alpha$ with $\alpha \approx 0.15$ [5.6].

For simplicity, one may assume that PSD of the active force also obeys a power-law behavior, i.e., $\langle m^2(\omega) \rangle \sim \omega^{-\gamma}$ with a different exponent γ. Among these three exponents, the following scaling relation should hold [5.6, 5.28]:

$$\beta = 2\alpha + \gamma - 1. \tag{5.48}$$

In thermal equilibrium, $\gamma = -\alpha + 1$ holds according to the FDT and hence $\beta = \alpha$. In this case, the anomalous diffusion purely reflects the viscoelasticity of the surrounding media. The exponentially correlated force dipoles in Eq. (5.39) leads to the active PSD in Eq. (5.40), and hence $\gamma = 2$ for $\omega\tau_\mathrm{d} \gg 1$. Experimentally, the value $\gamma \approx 2$ was observed by Lau *et al.* [5.28] and later reconfirmed by Guo *et al.* [5.6]. When $\alpha \approx 0.15$ and $\gamma \approx 2$, Eq. (5.48) gives $\beta \approx 1.3$ which is almost consistent with the MSD measurement mentioned above ($\beta \approx 1.2$). In the older experiment [5.28], on the other hand, the measured exponents were $\alpha \approx 0.25$,

70

$\gamma \approx 2$ and hence $\beta \approx 1.5$. In both of these experiments, they claimed that active forces dominate the low-frequency regime, whereas thermal forces dominate the high-frequency regime [5.6, 5.28].

It should be reminded, however, that different values of γ were reported by different groups [5.42–5.44]. For example, a combination of active and passive microrheology measurements using PC3 tumor cells resulted in $\alpha \approx 0.4$, $\beta \approx 1.3$ and $\gamma \approx 1.5$, satisfying also the scaling relation Eq. (5.48). They argued that such a difference can arise because active and passive measurements were done in Ref. [5.28] with different probes and at very different locations in the cell. In Refs. [5.42–5.44], they performed dual passive-active measurements with a unique probe. Given these situations, we consider that the power-law behavior of the force fluctuations and its exponent require further experimental and theoretical investigations.

We also point out that Eq. (5.48) cannot be always true because the exponents can take values only $0 \leq \beta \leq 2$ and $0 \leq \alpha \leq 1$. Hence, if $\gamma = 2$ holds, one should always observe a super-diffusive behavior because $\beta = 2\alpha + 1 \geq 1$. However, subdiffusive behaviors ($\beta < 1$) in cells have been observed in many cases [5.45–5.47]. Moreover, the above relation also restricts the value of α to $0 < \alpha \leq 0.5$ because $\beta < 2$, which is not always the case [5.19, 5.20].

In our work, we have assumed that the time correlation of a force dipole is an exponentially decaying function with a characteristic time τ_{d}, as given in Eq. (5.39). Hence its Fourier transform has a Lorentzian form, and decays as ω^{-2} for $\omega\tau_{\mathrm{d}} \gg 1$. A similar Lorentzian form of force fluctuations was discussed by Levine and MacKintosh [5.12, 5.13]. While some of the experiments which reported the exponent $\gamma = 2$ [5.6, 5.28] justify our assumption, different values of γ found in the other experiments [5.42–5.44] indicate that the dipole correlation cannot be a simple exponentially decaying function. Hence a more detailed investigation for the statistical property of a fluctuating force dipole is required. Currently, we are analyzing the stochastic properties of a simple model of a catalytically active bidomain protein [5.14]. In this model, the two protein domains are represented by beads

connected by an elastic spring, and the two internal states, namely, free protein and ligand-protein complex, are assumed.

Although our theory is general and can be applied not only for cells but also for other macroscopic systems, it is useful to give some typical parameter values corresponding to a cell. Since the characteristic length scale $\ell = (\eta/\Gamma)^{1/2}$ roughly corresponds to the mesh size of a polymer gel, it is roughly given by $\ell \sim 10^{-7}$ m for a typical cell. Hence the distance between the two point particles such as $d/\ell = 100$ means $d \sim 10^{-5}$ m. According to Ref. [5.6], we also have $\eta \sim 10^{-3}$ Pa·s and $\mu \sim 1$ Pa so that the viscoelastic time scale can be estimated as $\tau = \eta/\mu \sim 10^{-3}$ s. This means that the dipole time scale $\tau_{\mathrm{d}}/\tau = 100$ used in Figs. 5.6(b) and 5.9 corresponds to $\tau_{\mathrm{d}} \sim 10^{-1}$ s. Although this time scale is somewhat larger than the cycle time of a single protein machine [5.14], it still gives a good estimate to characterize the collective dynamics of a protein complex.

Recently, Fodor *et al.* [5.48] have made an attempt to theoretically reproduce the MSD data measured in the cytoplasm of living A7 [5.6]. They used one-dimensional Langevin equation in the presence of a random active force to calculate both the thermal and non-thermal MSD. Their theory has a similarity to the present work because they also introduce two time scales which are analogous to $\tau = \eta/\mu$ and τ_{d} in our theory. An important new aspect in the present paper is that the internal structure of the viscoelastic medium is properly taken into account. Both thermal and non-thermal MSDs exhibit complicated time sequences depending on the length-scale of the observation relative to the mesh size ℓ. In Ref. [5.48], the size of tracer particles was assumed to be always larger than the mesh size of the cytoskeletal network.

In our separate work, we have considered the two-fluid model where active macromolecules, described as force dipoles, cyclically operate both in the elastic and the fluid components [5.38]. Through coarse-graining, we have derived effective equations of motions for tracer particles displaying local deformations and local fluid flows. The equation for deformation tracers coincides with the phenomenological model by Fodor *et al.* [5.48] (see also the related publication [5.49]).

Our analysis reveals that localization and diffusion phenomena are generally involved. The motion of tracers immobilized within the elastic subsystem is localized in the long-time limit, but it can show a diffusion-like behavior at the intermediate time scales shorter than the cooperative correlation times of molecular motor aggregates operating in the active gels [5.38].

Recently, Bruinsma *et al.* [5.50] investigated a large scale correlated motion of chromatin inside the nuclei of living cells by using another "two-fluid model" for polymer solutions [5.51] (but not for gels). They derived the response functions that connect the chromatin density and velocity correlation function to the correlation functions of the active sources that are either scalar or vector quantities. One of the differences in their theory is that the form of the complex viscoelastic moduli needs to be specified in order to compare with experiments, whereas the viscoelasticity naturally arises from the present two-fluid model. It is interesting to note that their active PSD also contains Lorentzian type frequency dependence as we have obtained such as in Eq. (5.40). It would be interesting to calculate the active MSD based on this different two-fluid model.

Finally, we mention that anomalous diffusion observed in colloidal gels has been also explained in terms of force dipoles due to structural inhomogeneities [5.52, 5.53]. Assuming that such inhomogeneities are randomly distributed, it was shown that the relaxation time of the dynamic structure factor is inversely proportional to the wavenumber. In Ref. [5.54], the MSD exhibits diffusive motion at short times and super-diffusive motion at long times.

Appendix 5.A   Partial Green's function

In this appendix, we show the derivation of Eqs. (5.7) and (5.9) [5.34–5.37]. By using the Fourier transform in space and the Laplace transform in time, Eqs. (5.1), (5.2) and (5.4) can be represented in the steady state as

$$0 = -\mu q^2 \mathbf{u}[\mathbf{q}, s] - (\mu + \lambda)\mathbf{q}(\mathbf{q} \cdot \mathbf{u}[\mathbf{q}, s]) - \Gamma\left(s\mathbf{u}[\mathbf{q}, s] - \mathbf{v}[\mathbf{q}, s]\right), \qquad (5.49)$$

$$0 = -\eta q^2 \mathbf{v}[\mathbf{q}, s] - i\mathbf{q}p[\mathbf{q}, s] - \Gamma\left(\mathbf{v}[\mathbf{q}, s] - s\mathbf{u}[\mathbf{q}, s]\right) + \mathbf{f}_v[\mathbf{q}, s], \tag{5.50}$$

$$\mathbf{q} \cdot \mathbf{v}[\mathbf{q}, s] = 0. \tag{5.51}$$

Taking the inner products of both Eqs. (5.49) and (5.50) with $\mathbf{q}$, and using Eq. (5.51), we obtain

$$p[\mathbf{q}, s] = -\frac{i\mathbf{q} \cdot \mathbf{f}_v[\mathbf{q}, s]}{q^2}. \tag{5.52}$$

From Eq. (5.49), we can solve for $\mathbf{u}$ as

$$u_\alpha[\mathbf{q}, s] = \left(\frac{\Gamma}{\mu q^2 + s\Gamma}\delta_{\alpha\beta} - \frac{\Gamma(\mu + \lambda)q^2}{(\mu q^2 + s\Gamma)(2\mu q^2 + \lambda q^2 + s\Gamma)}\hat{q}_\alpha\hat{q}_\beta\right)v_\beta[\mathbf{q}, s]. \tag{5.53}$$

Substituting Eqs. (5.52) and (5.53) into Eq. (5.50), we obtain the following equation

$$\left(\frac{q^2[\eta\mu q^2 + (s\eta + \mu)\Gamma]}{\mu q^2 + s\Gamma}\delta_{\alpha\beta} - \frac{s\Gamma^2(\mu + \lambda)q^2}{(\mu q^2 + s\Gamma)(2\mu q^2 + \lambda q^2 + s\Gamma)}\hat{q}_\alpha\hat{q}_\beta\right)v_\beta[\mathbf{q}, s]$$
$$= (\delta_{\alpha\beta} - \hat{q}_\alpha\hat{q}_\beta)f_{v,\beta}[\mathbf{q}, s]. \tag{5.54}$$

Then we can solve for $\mathbf{v}$ as

$$v_\alpha[\mathbf{q}, s] = \frac{\mu q^2 + s\Gamma}{q^2[\eta\mu q^2 + (s\eta + \mu)\Gamma]}(\delta_{\alpha\beta} - \hat{q}_\alpha\hat{q}_\beta)f_{v,\beta}[\mathbf{q}, s]. \tag{5.55}$$

In terms of η_{b} and ξ defined in Eq. (5.8), we finally obtain Eq. (5.7).

Next, we derive the real space representation of the partial Green's function [5.41]. We first assume that it has the form of

$$G_{\alpha\beta}[\mathbf{r}, s] = C_1\delta_{\alpha\beta} + C_2\hat{r}_\alpha\hat{r}_\beta, \tag{5.56}$$

so that

$$G_{\alpha\alpha}[\mathbf{q}, s] = 3C_1 + C_2, \tag{5.57}$$

$$G_{\alpha\beta}[\mathbf{q}, s]\hat{r}_\alpha\hat{r}_\beta = C_1 + C_2. \tag{5.58}$$

Hence we have

$$\begin{aligned}
3C_1 + C_2 &= 2\int \frac{d^3q}{(2\pi)^3} \frac{1 + (\eta_\mathrm{b}/\eta)\xi^2 q^2}{\eta_\mathrm{b}q^2(1 + \xi^2 q^2)} e^{i\mathbf{q}\cdot\mathbf{r}}, \\
&= \frac{1}{2\pi\eta r}\left[1 + \frac{1 - \eta_\mathrm{b}/\eta}{\eta_\mathrm{b}/\eta}(1 - e^{-r/\xi})\right],
\end{aligned} \tag{5.59}$$

$$\begin{aligned}
C_1 + C_2 &= \int \frac{d^3q}{(2\pi)^3} \frac{1 + (\eta_\mathrm{b}/\eta)\xi^2 q^2}{\eta_\mathrm{b}q^2(1 + \xi^2 q^2)}\left[1 - (\hat{\mathbf{q}}\cdot\hat{\mathbf{r}})^2\right]e^{i\mathbf{q}\cdot\mathbf{r}} \\
&= \frac{1}{4\pi\eta r}\left[1 + \frac{1 - \eta_\mathrm{b}/\eta}{\eta_\mathrm{b}/\eta}\left(1 - 2(\xi/r)^2 + 2e^{-r/\xi}\left[(\xi/r) + (\xi/r)^2\right]\right)\right]. \tag{5.60}
\end{aligned}$$

Solving for C_1 and C_2, we finally arrive at Eq. (5.9) with Eqs. (5.10) and (5.11).

Appendix 5.B Derivation of Eq. (5.34)

In this appendix, we show the derivation of Eq. (5.34). Here we use the dimensionless form of the Green's function $g_{\alpha\beta} = 8\pi\eta\ell G_{\alpha\beta}$, and consider its asymptotic expression [see Eq. (5.14)]

$$\begin{aligned}
g_{\alpha\beta}[\mathbf{r}, \omega] &= \frac{i\omega\tau\ell}{r(1 + i\omega\tau)}(\delta_{\alpha\beta} + \hat{r}_\alpha\hat{r}_\beta) - \frac{2\ell^3}{r^3(1 + i\omega\tau)^2}(\delta_{\alpha\beta} - 3\hat{r}_\alpha\hat{r}_\beta) \\
&\equiv A_{\alpha\beta}(\mathbf{r}, \omega) - B_{\alpha\beta}(\mathbf{r}, \omega), \tag{5.61}
\end{aligned}$$

where we have defined the functions $A_{\alpha\beta}$ and $B_{\alpha\beta}$ in the last equation. The spatial derivatives of these functions with respect to $\bar{r} = r/\ell$ are

$$\frac{\partial}{\partial\bar{r}_\gamma}A_{\alpha\beta}(\mathbf{r}, \omega) = \frac{i\omega\tau}{1 + i\omega\tau}\left(\frac{\bar{r}_\alpha\delta_{\beta\gamma} + \bar{r}_\beta\delta_{\alpha\gamma} - \bar{r}_\gamma\delta_{\alpha\beta}}{\bar{r}^3} - 3\frac{\bar{r}_\alpha\bar{r}_\beta\bar{r}_\gamma}{\bar{r}^5}\right), \tag{5.62}$$

$$\frac{\partial}{\partial \bar{r}_\gamma} B_{\alpha\beta}(\mathbf{r},\omega) = \frac{2}{(1+i\omega\tau)^2}\left(-3\frac{\bar{r}_\alpha\delta_{\beta\gamma}+\bar{r}_\beta\delta_{\alpha\gamma}+\bar{r}_\gamma\delta_{\alpha\beta}}{\bar{r}^5}+15\frac{\bar{r}_\alpha\bar{r}_\beta\bar{r}_\gamma}{\bar{r}^7}\right). \quad (5.63)$$

Using these results, we can further calculate the following quantities

$$15\Omega_{\beta\beta'\gamma\gamma'}\frac{\partial}{\partial\bar{r}_\gamma}A_{\alpha\beta}(\mathbf{r},\omega)\frac{\partial}{\partial\bar{r}_{\gamma'}}A_{\alpha\beta'}(\mathbf{r},-\omega) = 12\frac{(\omega\tau)^2}{1+(\omega\tau)^2}\bar{r}^{-4}, \quad (5.64)$$

$$15\Omega_{\beta\beta'\gamma\gamma'}\frac{\partial}{\partial\bar{r}_\gamma}A_{\alpha\beta}(\mathbf{r},\omega)\frac{\partial}{\partial\bar{r}_{\gamma'}}B_{\alpha\beta'}(\mathbf{r},-\omega) = -72\frac{i\omega\tau-(\omega\tau)^2}{[1+(\omega\tau)^2]^2}\bar{r}^{-6}, \quad (5.65)$$

$$15\Omega_{\beta\beta'\gamma\gamma'}\frac{\partial}{\partial\bar{r}_\gamma}B_{\alpha\beta}(\mathbf{r},\omega)\frac{\partial}{\partial\bar{r}_{\gamma'}}A_{\alpha\beta'}(\mathbf{r},-\omega) = -72\frac{-i\omega\tau-(\omega\tau)^2}{[1+(\omega\tau)^2]^2}\bar{r}^{-6}, \quad (5.66)$$

$$15\Omega_{\beta\beta'\gamma\gamma'}\frac{\partial}{\partial\bar{r}_\gamma}B_{\alpha\beta}(\mathbf{r},\omega)\frac{\partial}{\partial\bar{r}_{\gamma'}}B_{\alpha\beta'}(\mathbf{r},-\omega) = \frac{720}{[1+(\omega\tau)^2]^2}\bar{r}^{-8}. \quad (5.67)$$

Hence the dimensionless PSD in Eq. (5.33) can be obtained as

$$\begin{aligned}
\mathcal{I}(\omega) &= 15\Omega_{\beta\beta'\gamma\gamma'}\int \mathrm{d}^3\bar{r}\,\frac{\partial g_{\alpha\beta}[\mathbf{r},\omega]}{\partial\bar{r}_\gamma}\frac{\partial g_{\alpha\beta'}[\mathbf{r},-\omega]}{\partial\bar{r}_{\gamma'}} \\
&= 4\pi\int_{\delta/\ell}^\infty \mathrm{d}\bar{r}\,\bar{r}^2\left(12\frac{(\omega\tau)^2}{1+(\omega\tau)^2}\bar{r}^{-4}-144\frac{(\omega\tau)^2}{[1+(\omega\tau)^2]^2}\bar{r}^{-6}+\frac{720}{[1+(\omega\tau)^2]^2}\bar{r}^{-8}\right) \\
&= 48\pi\left[\frac{(\omega\tau)^2}{1+(\omega\tau)^2}\left(\frac{\ell}{\delta}\right)-4\frac{(\omega\tau)^2}{[1+(\omega\tau)^2]^2}\left(\frac{\ell}{\delta}\right)^3+\frac{12}{[1+(\omega\tau)^2]^2}\left(\frac{\ell}{\delta}\right)^5\right].
\end{aligned}$$
$$(5.68)$$

Hence we finally obtain Eq. (5.34).

Appendix 5.C Full expression of Eq. (5.42)

The full expression of Eq. (5.42) including higher order terms in ℓ/δ is given as follows

$$
\langle (\Delta R_x)^2(t) \rangle
$$

$$
\approx \frac{1}{60\pi} \frac{c_0 S\tau}{\eta^2 \ell} \left[\left(\frac{1}{1+\tau_{\mathrm{d}}/\tau} + \frac{(\tau_{\mathrm{d}}/\tau)e^{-t/\tau_{\mathrm{d}}}}{1-(\tau_{\mathrm{d}}/\tau)^2} - \frac{e^{-t/\tau}}{1-(\tau_{\mathrm{d}}/\tau)^2} \right) \left(\frac{\ell}{\delta} \right) \right.
$$

$$
+ \left(\frac{\left[-2(t/\tau)(\tau_{\mathrm{d}}/\tau)^2 + 2t/\tau - 6(\tau_{\mathrm{d}}/\tau)^2 + 2 \right] e^{-t/\tau}}{\left[1-(\tau_{\mathrm{d}}/\tau)^2 \right]^2} + \frac{4(\tau_{\mathrm{d}}/\tau)^3 e^{-t/\tau_{\mathrm{d}}}}{\left[1-(\tau_{\mathrm{d}}/\tau)^2 \right]^2} \right.
$$

$$
\left. - \frac{2(2\tau_{\mathrm{d}}/\tau+1)}{\left[1+\tau_{\mathrm{d}}/\tau \right]^2} \right) \left(\frac{\ell}{\delta} \right)^3
$$

$$
+ \left(\frac{6 \left[-(t/\tau)(\tau_{\mathrm{d}}/\tau)^2 + t/\tau - 5(\tau_{\mathrm{d}}/\tau)^2 + 3 \right] e^{-t/\tau}}{\left[1-(\tau_{\mathrm{d}}/\tau)^2 \right]^2} + \frac{12(\tau_{\mathrm{d}}/\tau)^5 e^{-t/\tau_{\mathrm{d}}}}{\left[1-(\tau_{\mathrm{d}}/\tau)^2 \right]^2} \right.
$$

$$
\left. \left. - \frac{6[2(\tau_{\mathrm{d}}/\tau)^3 + 4(\tau_{\mathrm{d}}/\tau)^2 + 6\tau_{\mathrm{d}}/\tau + 3]}{\left[1+\tau_{\mathrm{d}}/\tau \right]^2} + \frac{12t}{\tau} \right) \left(\frac{\ell}{\delta} \right)^5 \right]. \tag{5.69}
$$

Bibliography

[5.1] B. Alberts, A. Johnson, P. Walter, J. Lewis, and M. Raff, *Molecular Biology of the Cell* (Garland Science, New York, 2008).

[5.2] C. P. Brangwynne, G. H. Koenderink, F. C. MacKintosh, and D. A. Weitz, J. Cell Biol. **183**, 583 (2008).

[5.3] F. C. MacKintosh, Proc. Nat. Acad. Sci. USA **109**, 7138 (2012).

[5.4] S. C. Weber, A. J. Spakowitz, and J. A. Theriot, Proc. Nat. Acad. Sci. USA **109**, 7338 (2012).

[5.5] B. R. Parry, I. V. Surovtsev, M. T. Cabeen, C. S. O'Hern, E. R. Dufresne, and C. Jacobs-Wagner, Cell **156**, 183 (2014).

[5.6] M. Guo, A. J. Ehrlicher, M. H. Jensen, M. Renz, J. R. Moore, R. D. Goldman, J. Lippincott-Schwartz, F. C. MacKintosh, and D. A. Weitz, Cell **158**, 822 (2014).

[5.7] X.-L. Wu and A. Libchaber, Phys. Rev. Lett. **84**, 3017 (2000).

[5.8] D. T. N. Chen, A. W. C. Lau, L. A. Hough, M. F. Islam, M. Goulian, T. C. Lubensky, and A. G. Yodh, Phys. Rev. Lett. **99**, 148302 (2007).

[5.9] K. C. Leptos, J. S. Guasto, J. P. Gollub, A. I. Pesci, and R. E. Goldstein, Phys. Rev. Lett. **103**, 198103 (2009).

[5.10] Y. Hatwalne, S. Ramaswamy, M. Rao, and R. A. Simha, Phys. Rev. Lett. **92**, 118101 (2004).

[5.11] P. T. Underhill and M. D. Graham, Phys. Fluids **23**, 121902 (2011).

[5.12] F. C. MacKintosh and A. J. Levine, Phys. Rev. Lett. **100**, 018104 (2008).

[5.13] A. J. Levine and F. C. MacKintosh, J. Phys. Chem. B **113**, 3820 (2009).

[5.14] A. S. Mikhailov and R. Kapral, Proc. Nat. Acad. Sci. USA **112**, E3639 (2015).

[5.15] R. Kapral and A. S. Mikhailov, Physica D **318**, 100 (2016).

[5.16] Y. Koyano, H. Kitahata, and A. S. Mikhailov Phys. Rev. E **94**, 022416 (2016).

[5.17] B. Fabry, G. N. Maksym, J. P. Butler, M. Glogauer, D. Navajas, and J. J. Fredberg, Phys. Rev. Lett. **87**, 148102 (2001).

[5.18] P. Kollmannsberger and B. Fabry, Annu. Rev. Mater. Res. **41**, 75 (2011).

[5.19] B. D. Hoffman, G. Massiera, K. M. Van Citters, and J. C. Crocker, Proc. Nat. Acad. Sci. USA **103**, 10259 (2006).

[5.20] B. D. Hoffman and J. C. Crocker, Annu. Rev. Biomed. Eng. **11**, 259 (2009).

[5.21] X. Trepat, L. Deng, S. S. An, D. Navajas, D. J. Tschumperlin, W. T. Gerthoffer, J. P. Butler, and J. J. Fredberg, Nature **447**, 592 (2007).

[5.22] T. G. Mason and D. A. Weitz, Phys. Rev. Lett. **74**, 1250 (1995).

[5.23] T. G. Mason, K. Ganesan, J. H. van Zanten, D. Wirtz, and S. C. Kuo, Phys. Rev. Lett. **79**, 3282 (1997).

[5.24] F. Gittes, B. Schnurr, P. D. Olmsted, F. C. MacKintosh, and C. F. Schmidt, Phys. Rev. Lett. **79**, 3286 (1997).

[5.25] B. Schnurr, F. Gittes, F. C. MacKintosh, and C. F. Schmidt, Macromolecules **30**, 7781 (1997).

[5.26] T. G. Mason, Rheol. Acta **39**, 371 (2000).

[5.27] T. M. Squires and T. G. Mason, Annu. Rev. Fluid Mech. **42**, 413 (2010).

[5.28] A. W. C. Lau, B. D. Hoffman, A. Davies, J. C. Crocker, and T. C. Lubensky, Phys. Rev. Lett. **91**, 198101 (2003).

[5.29] A. W. C. Lau and T. C. Lubensky, Phys. Rev. E **80**, 011917 (2009).

[5.30] P. G. de Gennes, Macromolecules **9**, 587 (1976).

[5.31] P. G. de Gennes, Macromolecules **9**, 594 (1976).

[5.32] F. Brochard and P. G. de Gennes, Macromolecules **10**, 1157 (1977).

[5.33] J. C. Crocker, M. T. Valentine, E. R. Weeks, T. Gisler, P. D. Kaplan, A. G. Yodh, and D. A. Weitz, Phys. Rev. Lett. **85**, 888 (2000).

[5.34] A. J. Levine and T. C. Lubensky, Phys. Rev. Lett. **85**, 1774 (2000).

[5.35] A. J. Levine and T. C. Lubensky, Phys. Rev. E **63**, 041510 (2001).

[5.36] A. Sonn-Segev, A. Bernheim-Groswasser, H. Diamant, and Y. Roichman, Phys. Rev. Lett. **112**, 088301 (2014).

[5.37] A. Sonn-Segev, A. Bernheim-Groswasser, and Y. Roichman, Soft Matter **10**, 8324 (2014).

[5.38] K. Yasuda, R. Okamoto, S. Komura, and A. S. Mikhailov, to be published in EPL.

[5.39] H. Diamant, Eur. Phys. J. E **38**, 32 (2015).

[5.40] D. T. N. Chen, Q. Wen, P. A. Janmey, J. C. Crocker, and A. G. Yodh, Annu. Rev. Condens. Matter Phys. **1**, 301 (2010).

[5.41] M. Doi and S. F. Edwards, *The Theory of Polymer Dynamics*, (Clarendon Press, Oxford, 1986).

[5.42] C. Wilhelm, Phys. Rev. Lett. **101**, 028101 (2008).

[5.43] F. Gallet, D. Arcizet, P. Bohec, and A. Richert, Soft Matter **5**, 2947 (2009).

[5.44] D. Robert, T.-H. Nguyen, F. Gallet, and C. Wilhelm, PLoS ONE **5**, e10046 (2010).

[5.45] I. M. Tolić-Nørrelykke, E.-L. Munteanu, G. Thon, L. Oddershede, and K. Berg-Sørensen Phys. Rev. Lett. **93**, 078102 (2004).

[5.46] I. Golding and E. C. Cox, Phys. Rev. Lett. **96**, 098102 (2006).

[5.47] S. C. Weber, A. J. Spakowitz, and J. A. Theriot, Phys. Rev. Lett. **104**, 238102 (2010).

[5.48] É. Fodor, M. Guo, N. S. Gov, P. Visco, D. A. Weitz, and F. van Wijland, EPL **110**, 48005 (2015).

[5.49] É. Fodor, W. W. Ahmed, M. Almonacid, M. Bussonnier, N. S. Gov, M.-H. Verlhac, T. Betz, P. Visco, and F. van Wijland, EPL **116**, 30008 (2016).

[5.50] R. Bruinsma, A. Y. Grosberg, Y. Rabin, and A. Zidovska, Biophys. J. **106**, 1871 (2014).

[5.51] M. Doi and A. Onuki, J. Phys. II (France) **2**, 1631 (1992).

[5.52] L. Cipelletti, S. Manley, R. C. Ball, and D. A. Weitz, Phys. Rev. Lett. **84**, 2275 (2000).

[5.53] A. Duri and L. Cipelletti, EPL **76**, 972 (2006).

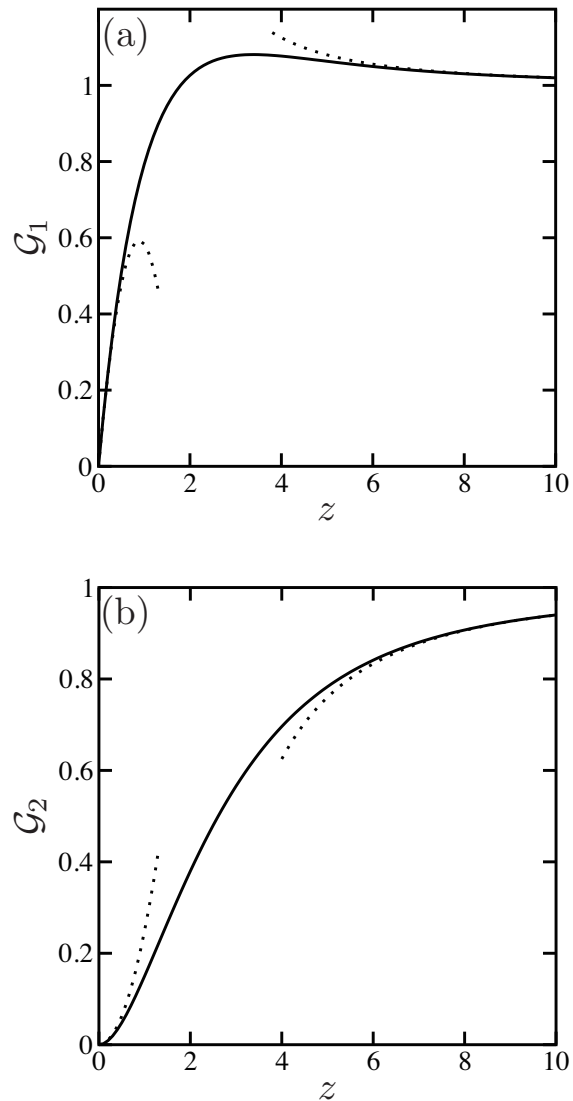[5.54] Y. Gao, J. Kima, and M. E. Helgeson, Soft Matter **11**, 6360 (2015).

Figure 5.2: Scaling functions (a) $\mathcal{G}_1$ and (b) $\mathcal{G}_2$ [see Eq. (5.10) and (5.11), respectively] appearing in the partial Green's function of the two-fluid model. The scaling variable is $z = r/\xi$, where r is the distance and ξ is the frequency-dependent characteristic length scale [see Eq. (5.8)]. The asymptotic behaviors of these scaling functions, as analytically given by Eqs. (5.12) and (5.13), respectively, are plotted with dotted lines.
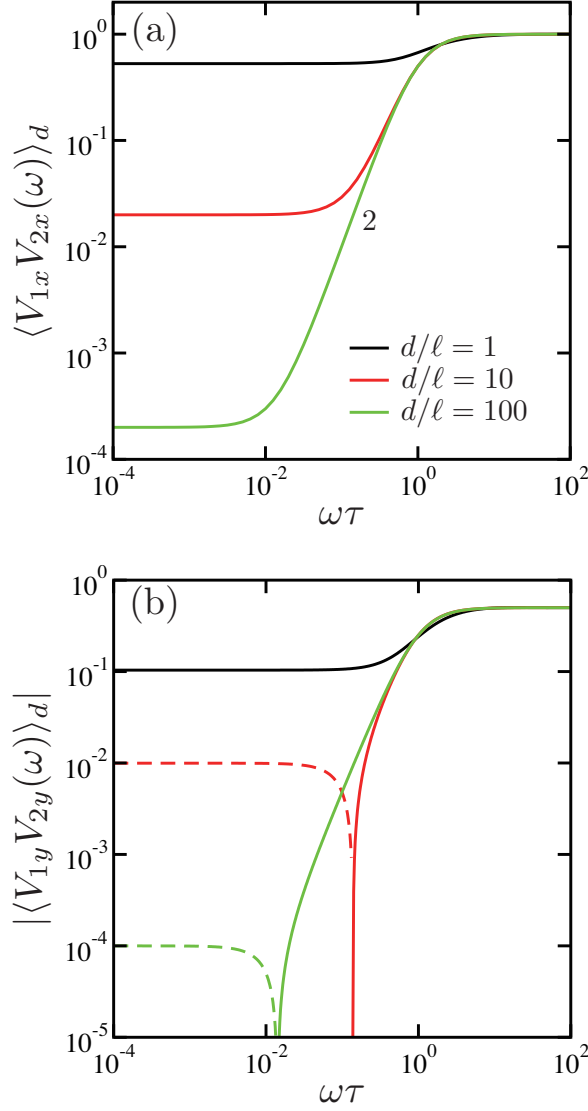
Figure 5.3: The passive component of the power spectral density (PSD) of the two-point velocity cross-correlation functions (CCFs) (a) $\langle V_{1x}V_{2x}(\omega)\rangle_d$ and (b) $|\langle V_{1y}V_{2y}(\omega)\rangle_d|$ [see Eq. (5.19)] as a function of $\omega\tau$ for $d/\ell = 1, 10, 100$. Here $\tau = \eta/\mu$ is the viscoelastic time scale, and d is the distance between the two point particles immersed in viscoelastic media described by the two-fluid model. Both CCFs are scaled by $k_B T/(2\pi\eta d)$ in order to make them dimensionless. Since $\langle V_{1y}V_{2y}(\omega)\rangle_d$ takes negative values for smaller $\omega\tau$ (shown by the dashed lines), we have plotted in (b) its absolute value. The number "2" in (a) indicates the slope representing the exponent of the power-law behaviors.
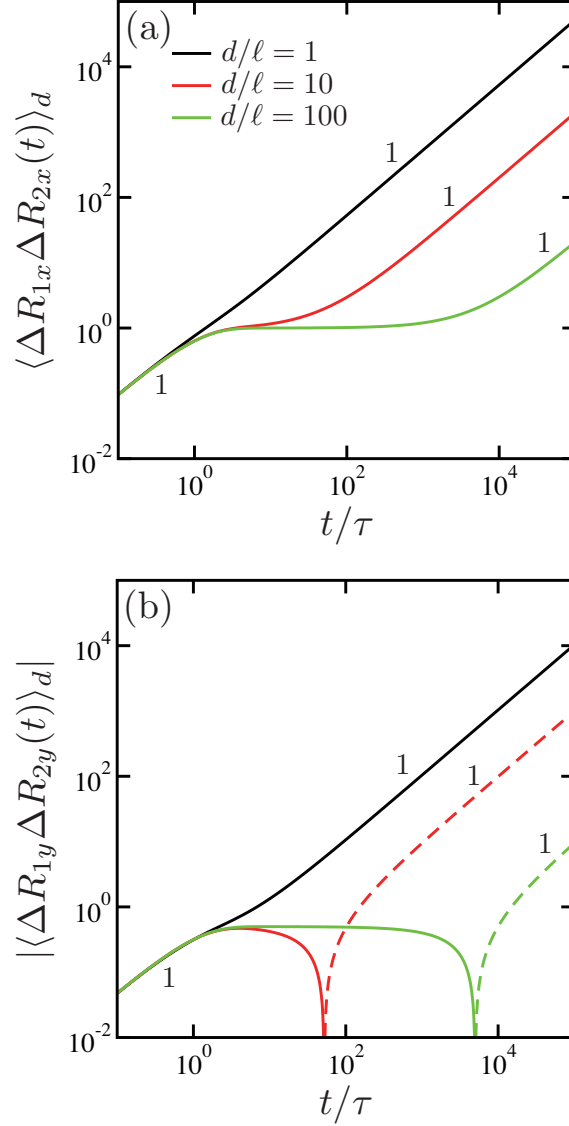
83

Figure 5.4: The passive component of the two-point displacement cross-correlation functions (CCFs) (a) $\langle \Delta R_{1x} \Delta R_{2x}(t) \rangle_d$ and (b) $|\langle \Delta R_{1y} \Delta R_{2y}(t) \rangle_d|$ [see Eq. (5.20)] as a function of t/τ for $d/\ell = 1, 10, 100$. Here d is the distance between the two point particles immersed in viscoelastic media. Both CCFs are scaled by $k_B T \tau / (2\pi \eta d)$ in order to make them dimensionless. Since $\langle \Delta R_{1y} \Delta R_{2y}(t) \rangle_d$ takes negative values for larger t/τ (shown by the dashed lines), we have plotted in (b) its absolute value. The numbers indicate the slope representing the exponent of the power-law behaviors.
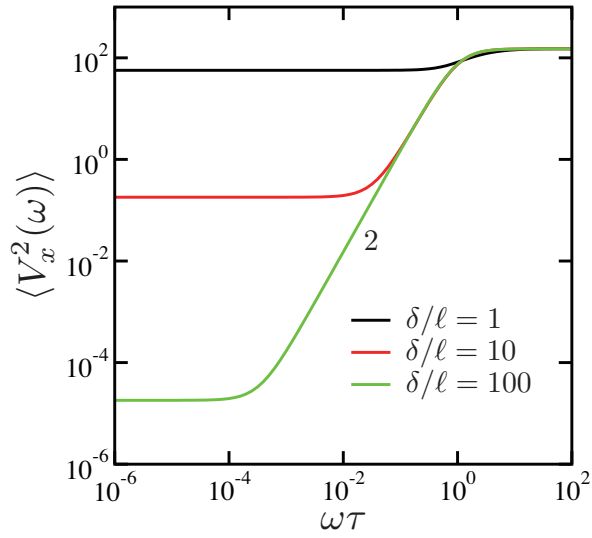
Figure 5.5: The active component of the power spectral density (PSD) $\langle V_x^2(\omega) \rangle$ [see Eq. (5.32)] as a function of $\omega\tau$ for $\delta/\ell = 1, 10, 100$. Here a single point particle is immersed in viscoelastic media described by the two-fluid model, and δ is the cutoff length corresponding to the particle size. In the plot, the PSD is scaled by $c_0\langle m^2(\omega)\rangle/(2880\pi^2\eta^2\delta)$ in order to make it dimensionless. The number indicates the slope representing the exponent of the power-law behavior.
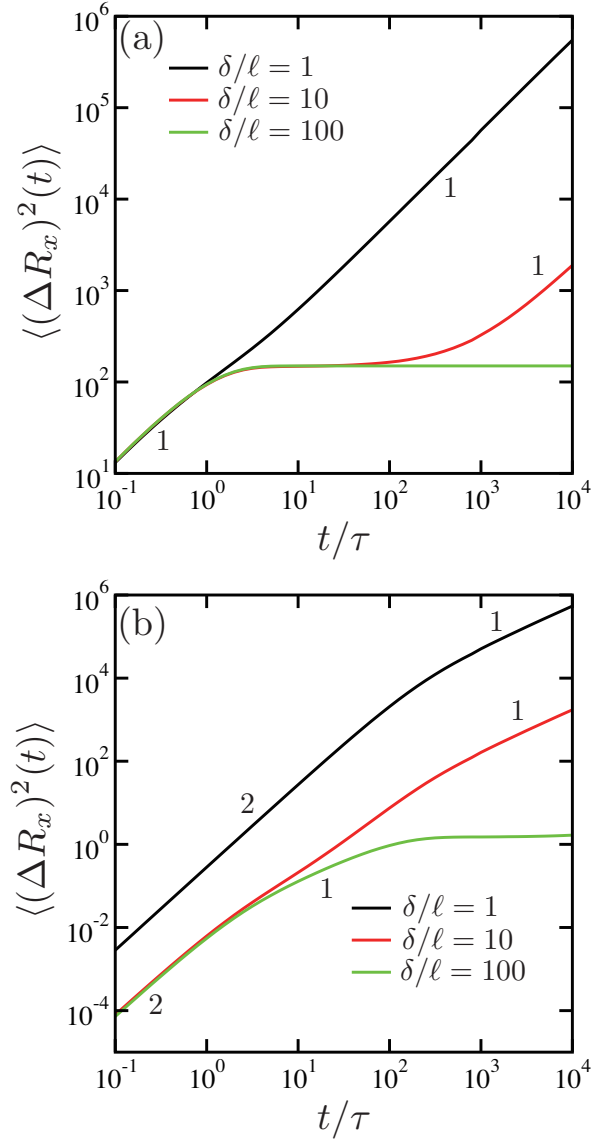
Figure 5.6: The active component of the mean squared displacement (MSD) $\langle(\Delta R_x)^2(t)\rangle$ [see Eq. (5.36)] as a function of t/τ for $\delta/\ell = 1$, 10, 100. Here a single point particle is immersed in viscoelastic media, and δ is the cutoff length. (a) The case when the time correlation of the force dipole is δ-correlated [see Eq. (5.35)]. (b) The case when the time correlation of the force dipole decays exponentially with a characteristic relaxation time τ_{d} [see Eq. (5.39)], and we set here $\tau_{\mathrm{d}}/\tau = 100$. In these plots, $\langle(\Delta R_x)^2(t)\rangle$ is scaled by $c_0 S\tau/(2880\pi^2\eta^2\delta)$ in order to make it dimensionless. The numbers indicate the slope representing the exponent of the power-law behavior.
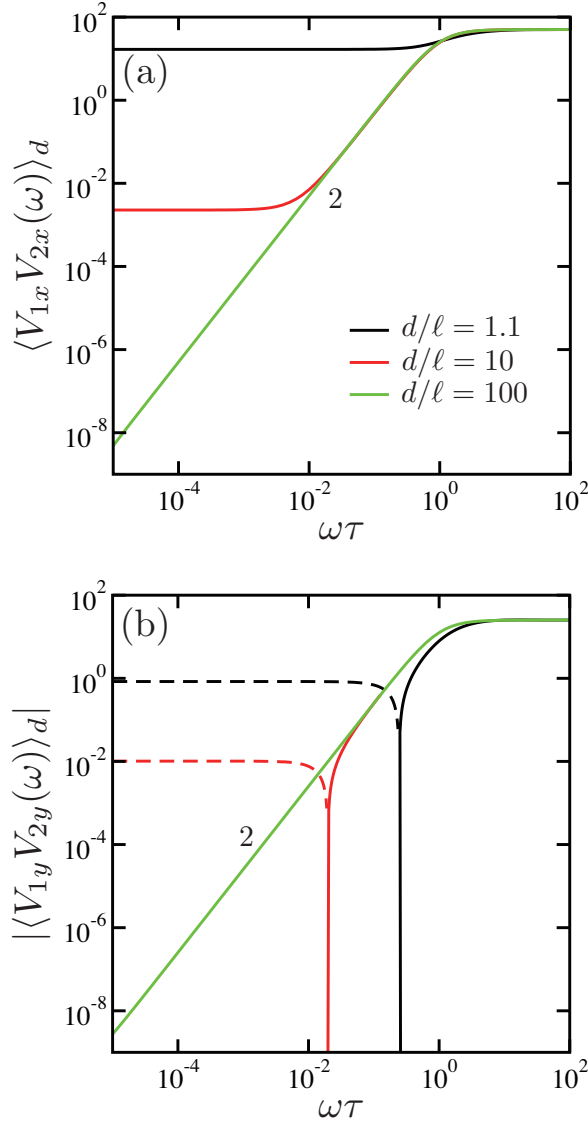
Figure 5.7: The active component of the scaled power spectral density (PSD) (a) $\langle V_{1x}V_{2x}(\omega)\rangle_d$ and (b) $|\langle V_{1y}V_{2y}(\omega)\rangle_d|$ [see Eq. (5.44)] as a function of $\omega\tau$ for $d/\ell = 1.1, 10, 100$. Here d is the distance between the two point particles immersed in viscoelastic media. Both PSDs are scaled by $c_0\langle m^2(\omega)\rangle/(960\pi^2\eta^2 d)$ in order to make them dimensionless. Since $\langle V_{1y}V_{2y}(\omega)\rangle_d$ takes negative values for smaller $\omega\tau$ (shown by the dashed lines), we have plotted in (b) its absolute value. The numbers indicate the slope representing the exponent of the power-law behaviors.
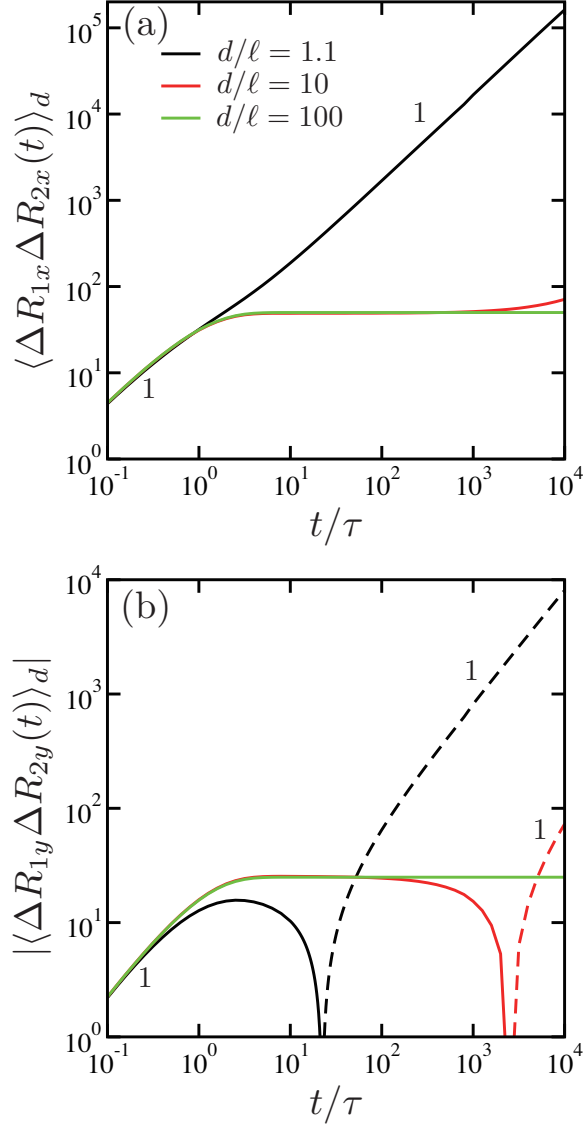
Figure 5.8: The active component of the two-point displacement cross-correlation functions (CCFs) (a) $\langle \Delta R_{1x} \Delta R_{2x}(t) \rangle_d$ and (b) $|\langle \Delta R_{1y} \Delta R_{2y}(t) \rangle_d|$ as a function of t/τ for $d/\ell = 1.1, 10, 100$. Here d is the distance between the two point particles immersed in viscoelastic media, and the time correlation of the force dipole is δ-correlated [see Eq. (5.35)]. Both CCFs are scaled by $c_0 S \tau/(960\pi^2 \eta^2 d)$ in order to make them dimensionless. Since $\langle \Delta R_{1y} \Delta R_{2y}(t) \rangle_d$ takes negative values for larger t/τ (shown by the dashed lines), we have plotted in (b) its absolute value. The numbers indicate the slope representing the exponent of the power-law behaviors.
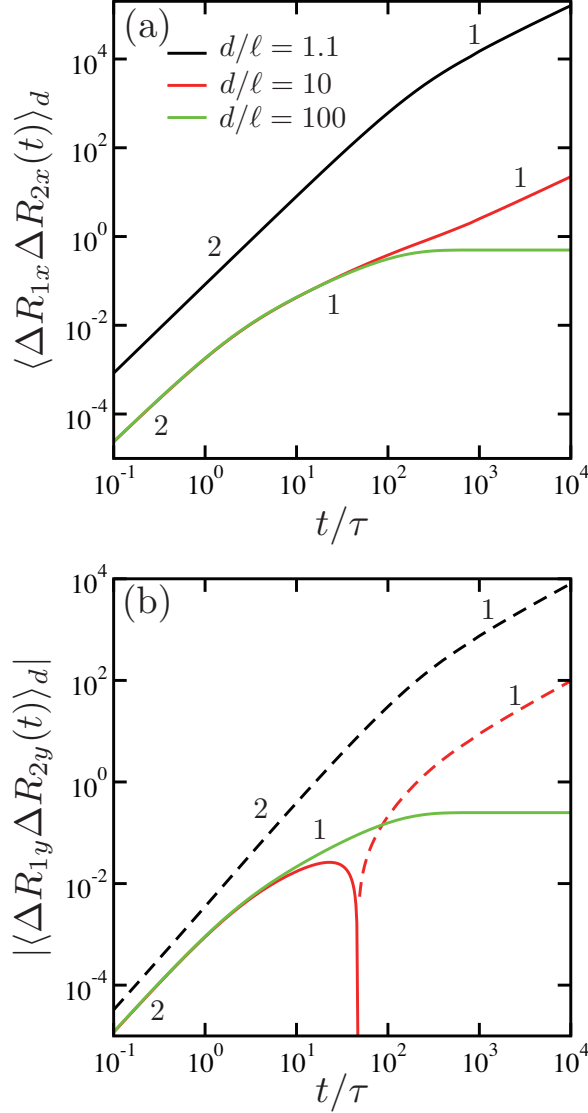
Figure 5.9: The active component of the two-point displacement cross-correlation functions (CCFs) (a) $\langle \Delta R_{1x} \Delta R_{2x}(t) \rangle_d$ and (b) $|\langle \Delta R_{1y} \Delta R_{2y}(t) \rangle_d|$ as a function of t/τ for $d/\ell = 1.1, 10, 100$. Here d is the distance between the two point particles immersed in viscoelastic media. The time correlation of the force dipole decays exponentially with a characteristic relaxation time τ_d [see Eq. (5.39)], and we set here $\tau_d/\tau = 100$. Both CCFs are scaled by $c_0 S \tau/(960\pi^2\eta^2 d)$ in order to make them dimensionless. Since $\langle \Delta R_{1y} \Delta R_{2y}(t) \rangle_d$ takes negative values for larger t/τ (shown by the dashed lines), we have plotted in (b) its absolute value. The numbers indicate the slope representing the exponent of the power-law behaviors.

Chapter 6

Dynamics of a membrane interacting with an active wall

Active motions of a biological membrane can be induced by non-thermal fluctuations that occur in the outer environment of the membrane. We discuss the dynamics of a membrane interacting hydrodynamically with an active wall that exerts random velocities on the ambient fluid. Solving the hydrodynamic equations of a bound membrane, we first derive a dynamic equation for the membrane fluctuation amplitude in the presence of different types of walls. Membrane two-point correlation functions are calculated for three different cases; (i) a static wall, (ii) an active wall, and (iii) an active wall with an intrinsic time scale. We focus on the mean squared displacement (MSD) of a tagged membrane describing the Brownian motion of a membrane segment. For the static wall case, there are two asymptotic regimes of MSD ($\sim t^{2/3}$ and $\sim t^{1/3}$) when the hydrodynamic decay rate changes monotonically. In the case of an active wall, the MSD grows linearly in time ($\sim t$) in the early stage, which is unusual for a membrane segment. This linear-growth region of the MSD is further extended when the active wall has a finite intrinsic time scale.

6.1 Introduction

The random slow dynamics of fluid membranes visible as a flickering phenomenon in giant unilamellar vesicles (GUVs) or red blood cells (RBCs) has attracted many interests in the last few decades [6.1]. These thermally excited shape fluctuations can be essentially understood as a Brownian motion of a two-dimensional (2D) lipid bilayer membrane in a three-dimensional (3D) viscous fluid such as water. For spherically closed artificial GUVs, characteristic relaxation times for shape deformations were calculated analytically [6.2–6.5]. Analysis of shape fluctuations can be used for quantitative measurements of surface tension and/or bending rigidity of single-component GUVs [6.6] or GUVs containing bacteriorhodopsin pumps [6.7].

Historically, investigations on fluctuations of cell membranes have started with RBCs whose flickering can be observed under a microscope [6.8]. Brochard and Lennon were among the first to describe quantitatively membrane fluctuations as thermally excited undulations, mainly governed by the bending rigidity of the membrane [6.9]. Later experiments showed that flickering in RBCs is not purely of thermal origin but rather corresponds to a non-equilibrium situation because the fluctuation amplitude decreases upon ATP depletion [6.10, 6.11]. Here ATP hydrolysis plays an important role to control membrane-spectrin cytoskeleton interactions [6.12]. More advanced techniques have demonstrated that, at longer time scales (small frequencies), a clear difference exists between the power spectral density of RBC membranes measured for normal cells and those ATP depleted; the fluctuation amplitude turns out to be higher in the former [6.13, 6.14]. At shorter time scales, on the other hand, membranes fluctuate as in the thermodynamic equilibrium. It should be noted, however, that the role of ATP in flickering is still debatable because Boss *et al.* have recently claimed that the mean fluctuation amplitudes of RBC membranes can be described by the thermal equilibrium theory, while ATP merely affects the bending rigidity [6.15].

In order to understand shape fluctuations of RBCs, one needs to properly take into account the effects of spectrin cytoskeleton network that is connected to the

91

membrane by actin, glycophorin, and protein 4.1R [6.1, 6.12]. Gov *et al.* treated the cytoskeleton as a rigid wall (shell) located at a fixed distance from the membrane, and assumed that its static and dynamic fluctuations are confined by the cytoskeleton [6.16, 6.17]. They further considered that the sparse connection of membrane and cytoskeleton gives rise to a finite surface tension for length scales larger than the membrane persistence length. The bending free energy for a membrane was extended to include a surface tension and a confinement potential with which the effects of ATP on the membrane fluctuations was described. However, since an active component of the membrane fluctuations also depend on the fluid viscosity [6.18], they cannot be solely attributed to the static parameters such as the surface tension or the potential. Gov and Safran later estimated the active contribution to the membrane fluctuations due to the release of stored tension in the spectrin filament and membrane in each dissociation event [6.19, 6.20]. In contrast to static thermal fluctuations, they showed that the active cytoskeleton may contribute to the membrane fluctuations at intermediate length scales.

Effects of membrane confinement are important not only for shape fluctuations of RBCs but also for a hydrodynamic coupling between closely apposed lipid bilayer membranes [6.21, 6.22], and dynamical transitions occurring in lamellar membranes under shear flow [6.23, 6.24]. After the seminal works by Kramer [6.25] and by Brochard and Lennon [6.9], the wavenumber-dependent decay rate for the bending modes of a membrane bound to a wall was calculated by Seifert [6.26] and Gov *et al.* [6.17]. In particular, Seifert showed that the scale separation between the membrane-wall distance and the correlation length determined by the confinement potential can lead to various crossover behaviors of the decay rate. In these hydrodynamic calculations, however, the wall that interacts with the membrane was treated as a static object and does not play any active role.

Quite generally, active motions of a membrane can be induced by non-thermal fluctuations that occur in the outer environment of the membrane such as cytoskeleton or cytoplasm. In this paper, we consider the dynamics of a membrane interacting with an active wall that generates random velocities in the ambient

fluid. These random velocities at the wall can be naturally taken into account through the boundary conditions of the fluid. We first derive a dynamic equation for the membrane fluctuation amplitude in the presence of hydrodynamic interactions. Then we calculate the membrane two-point correlation functions for three different cases; (i) a static wall, (ii) an active wall, and (iii) an active wall with an intrinsic time scale. We especially focus on the mean squared displacement (MSD) of a tagged membrane segment, and discuss its asymptotic time dependencies for the above cases. For the static wall case, the membrane fluctuates due to thermal agitations, and there are two asymptotic regimes of MSD ($\sim t^{2/3}$ and $\sim t^{1/3}$) if the hydrodynamic decay rate changes monotonically as a function of the wavenumber. When the wall is active, there is a region during which the MSD grows linearly with time ($\sim t$), which is unusual for a membrane segment. If the active wall has a finite intrinsic time scale, the above linear-growth regime of the MSD is further extended. As a whole, active fluctuations at the wall propagate through the surrounding fluid and greatly affects the membrane fluctuations.

This paper is organized as follows. In the next section, we discuss the hydrodynamics of a bound membrane that interacts with an active wall. We also derive a dynamic equation for the membrane fluctuation amplitude in the presence of hydrodynamic interactions. In Sec. 6.3, we calculate the membrane two-point correlation functions for three different cases of the wall as mentioned above. We investigate various asymptotic behaviors of the MSD of a tagged membrane both in the static and the active wall cases. Some further discussions are provided in Sec. 6.4.

6.2   Hydrodynamics of a bound membrane

6.2.1   Free energy of a bound membrane

As depicted in Fig. 6.1, we consider a fluid membrane bound at an average distance $\bar{\ell}$ from a wall which defines the xy-plane. Within the Monge representation, which
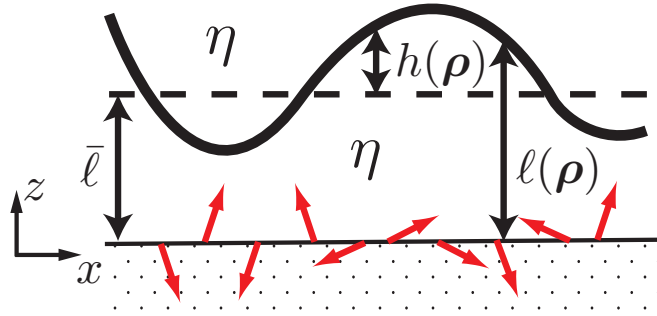
Figure 6.1: A fluctuating membrane interacting with an active wall. The membrane separated by a distance $\ell(\boldsymbol{\rho})$ from the wall feels a potential $V(\ell)$ per unit area. The average of $\ell(\boldsymbol{\rho})$ is $\bar{\ell}$, and the membrane fluctuation is defined by $h(\boldsymbol{\rho}) = \ell(\boldsymbol{\rho}) - \bar{\ell}$. Between the membrane and the wall as well as above the membrane are filled with a fluid of viscosity η. Red arrows on the wall indicate active velocities exerted on the fluid by the wall.

is valid for nearly flat surfaces, the membrane shape is specified by the distance $\ell(\boldsymbol{\rho}) = \ell(x, y)$ between the membrane and the wall. The free energy F of a tensionless membrane in a potential $V(\ell)$ per unit area reads [6.27, 6.28]

$$F = \int d^2\rho \left[\frac{\kappa}{2} (\nabla^2 \ell)^2 + V(\ell) \right], \tag{6.1}$$

where κ is the bending rigidity and $d^2\rho = dx\,dy$. We use a harmonic approximation for fluctuations $h(\boldsymbol{\rho}) = \ell(\boldsymbol{\rho}) - \bar{\ell}$ around the minimum of the potential at $\ell = \bar{\ell}$, and obtain the approximated form

$$F \approx \frac{\kappa}{2} \int d^2\rho \left[(\nabla^2 h)^2 + \xi^{-4} h^2 \right], \tag{6.2}$$

where $\xi = [\kappa/(d^2V/d\ell^2)_{\ell=\bar{\ell}}]^{1/4}$ is the correlation length due to the potential. Later we use a dimensionless quantity defined by $\Xi \equiv \xi/\bar{\ell}$ in order to discuss different cases.

In the following, we introduce the 2D spatial Fourier transform of $h(\boldsymbol{\rho})$ defined

as

$$h(\boldsymbol{q}) = \int d^2\rho\, h(\boldsymbol{\rho})e^{-i\boldsymbol{q}\cdot\boldsymbol{\rho}}, \tag{6.3}$$

where $\boldsymbol{q} = (q_x, q_y)$. Then the static correlation function can be obtained from Eq. (6.2) as

$$\langle h(\boldsymbol{q})h(-\boldsymbol{q})\rangle = \frac{k_{\mathrm{B}}T}{\kappa(q^4 + \xi^{-4})} = \frac{k_{\mathrm{B}}T}{E(q, \xi)}, \tag{6.4}$$

where k_{B} is the Boltzmann constant, T the temperature, $q = |\boldsymbol{q}|$ and we have introduced the notation $E(q, \xi) \equiv \kappa(q^4 + \xi^{-4})$.

In the present model, we assume that the wall is rigid and does not deform. Even when the wall, mimicking the cytoskeleton network, is deformable, the above free energy Eq. (6.1) would not be changed if we regard ℓ as a local distance between the membrane and the cytoskeleton. In this case, however, the bending rigidity κ should be replaced with an effective one which is also dependent on the bending rigidity of the cytoskeleton network itself [6.29].

6.2.2 Hydrodynamic equations and boundary conditions

The dynamics of a membrane is dominated by the surrounding fluid which is assumed to be incompressible and to obey the Stokes equation. We choose z as the coordinate perpendicular to the wall located at $z = 0$ as in Fig. 6.1. Then the velocity $\boldsymbol{v}(\boldsymbol{\rho}, z)$ and the pressure $p(\boldsymbol{\rho}, z)$ for $z \neq \bar{\ell}$ satisfy the following equations

$$\nabla \cdot \boldsymbol{v} = 0, \tag{6.5}$$

$$\eta\nabla^2\boldsymbol{v} - \nabla p - \boldsymbol{f} = 0, \tag{6.6}$$

where η is the viscosity of the surrounding fluid and $\boldsymbol{f}(\boldsymbol{\rho}, z)$ is any force acting on the fluid. The fluid velocity can be obtained from the above equations by

supplementing them with proper boundary conditions. In Appendix 6.A, we show a formal solution appropriate for the membrane/wall system, and obtain the fluid velocity $\boldsymbol{v}$ in terms of the force $\boldsymbol{f}$. Without loss of generality, we can choose the x- and y-coordinates as the parallel (longitudinal) and the perpendicular (transverse) directions to the in-plane vector $\boldsymbol{q}$, respectively. Since the transverse y-component of the velocity is not coupled to the other components, we are allowed to set $v_y = 0$ in what follows.

Let us denote the fluid regions $0 \leq z \leq \bar{\ell}$ and $\bar{\ell} \leq z$ with the superscripts "$-$" and "$+$", respectively. In general, we consider time-dependent boundary conditions at $z = 0$ and time-independent conditions at $z \to \infty$:

$$v_x^-(\boldsymbol{q}, z = 0, t) = V_{x0}(\boldsymbol{q}, t), \tag{6.7}$$

$$v_z^-(\boldsymbol{q}, z = 0, t) = V_{z0}(\boldsymbol{q}, t), \tag{6.8}$$

$$v_x^+(\boldsymbol{q}, z \to \infty, t) = v_z^+(\boldsymbol{q}, z \to \infty, t) = 0. \tag{6.9}$$

The statistical properties of $V_{x0}(\boldsymbol{q}, t)$ and $V_{z0}(\boldsymbol{q}, t)$ will be discussed for different types of walls in the next Section. As described in Appendix, the z-component of the velocity is then obtained as

$$\begin{aligned} v_z^-(\boldsymbol{q}, z, t) = &A[\sinh(qz) - qz\cosh(qz)] + Bqz\sinh(qz) \\ &- iqzV_{x0}(\boldsymbol{q}, t)e^{-qz} + (1 + qz)V_{z0}(\boldsymbol{q}, t)e^{-qz}, \end{aligned} \tag{6.10}$$

$$v_z^+(\boldsymbol{q}, z, t) = Ce^{-q(z-\bar{\ell})} + Dq(z - \bar{\ell})e^{-q(z-\bar{\ell})}, \tag{6.11}$$

where A, B, C, and D are the coefficients determined by the other boundary conditions at the membrane $z = \bar{\ell}$. Note that both v_x and p can be also expressed in terms of these four coefficients.

At $z = \bar{\ell}$ where the membrane exists, continuity of v_x and v_z yields

$$v_x^-(\boldsymbol{q}, z = \bar{\ell}, t) = v_x^+(\boldsymbol{q}, z = \bar{\ell}, t), \tag{6.12}$$

$$v_z^-(\boldsymbol{q}, z = \bar{\ell}, t) = v_z^+(\boldsymbol{q}, z = \bar{\ell}, t), \tag{6.13}$$

and incompressibility of the membrane requires that the in-plane divergence of v_x vanishes

$$iqv_x^-(\boldsymbol{q}, z = \bar{\ell}, t) = 0. \tag{6.14}$$

Moreover, the forces are required to balance in the normal direction at $z = \bar{\ell}$. This condition is written as

$$-T_{zz}^+ + T_{zz}^- = -\frac{\delta F}{\delta h(\boldsymbol{q}, t)} = -E(q, \xi)h(\boldsymbol{q}, t), \tag{6.15}$$

where $E(q, \xi)$ was defined in Eq. (6.4). In the above, $T_{zz}^\pm$ is the zz-component of the fluid stress tensor

$$T_{ij} = -p\delta_{ij} + \eta(\partial_i v_j + \partial_j v_i), \tag{6.16}$$

evaluated at $z = \bar{\ell} \pm 0$ and $i, j = x, z$. The above four boundary conditions in Eqs. (6.12)–(6.15) at $z = \bar{\ell}$ determine the solution of $\boldsymbol{v}$ and p in the entire region of the fluid.

6.2.3 Dynamic equation of a bound membrane

Next we derive a dynamic equation for the membrane fluctuation amplitude. The time derivative of the fluctuation amplitude $h(\boldsymbol{q}, t)$ (membrane velocity) should coincide with the normal velocity of the fluid at the membrane $v_z(\boldsymbol{q}, z = \bar{\ell}, t)$ obtained from Eqs. (6.10) and (6.11) together with the four coefficients (see also Appendix). Using the result of the above hydrodynamic calculation, we can write

the dynamic equation of $h(\boldsymbol{q}, t)$ as follows

$$\frac{\partial h(\boldsymbol{q}, t)}{\partial t} = -\gamma(q, \bar{\ell}, \xi)h(\boldsymbol{q}, t) + \Lambda_x(q, \bar{\ell})V_{x0}(\boldsymbol{q}, t) + \Lambda_z(q, \bar{\ell})V_{z0}(\boldsymbol{q}, t) + \zeta(\boldsymbol{q}, t).$$

(6.17)

In the above, $\gamma(q, \bar{\ell}, \xi)$ is the hydrodynamic decay rate

$$\gamma(q, \bar{\ell}, \xi) = \Gamma(q, \bar{\ell})E(q, \xi),$$ (6.18)

where the kinetic coefficient $\Gamma(q, \bar{\ell})$ is given by

$$\Gamma(q, \bar{\ell}) = \frac{1}{2\eta q}\frac{\sinh^2(q\bar{\ell}) - (q\bar{\ell})^2}{\sinh^2(q\bar{\ell}) - (q\bar{\ell})^2 + \sinh(q\bar{\ell})\cosh(q\bar{\ell}) + (q\bar{\ell})}.$$ (6.19)

The same expression was obtained by Seifert [6.26]. The second and the third terms on the r.h.s. of Eq. (6.17) are due to the wall boundary conditions Eqs. (6.7) and (6.8). Our calculation yields

$$\Lambda_x(q, \bar{\ell}) = \frac{-iq\bar{\ell}\sinh(q\bar{\ell})}{\sinh^2(q\bar{\ell}) - (q\bar{\ell})^2 + \sinh(q\bar{\ell})\cosh(q\bar{\ell}) + (q\bar{\ell})},$$ (6.20)

$$\Lambda_z(q, \bar{\ell}) = \frac{\sinh(q\bar{\ell}) + q\bar{\ell}\cosh(q\bar{\ell})}{\sinh^2(q\bar{\ell}) - (q\bar{\ell})^2 + \sinh(q\bar{\ell})\cosh(q\bar{\ell}) + (q\bar{\ell})}.$$ (6.21)

The last term in Eq. (6.17) represents the thermal white noise; its average vanishes $\langle\zeta(\boldsymbol{q}, t)\rangle = 0$ while its correlation is fixed by the fluctuation-dissipation theorem (FDT) [6.30, 6.31]

$$\langle\zeta(\boldsymbol{q}, t)\zeta(-\boldsymbol{q}, t')\rangle = 2k_{\mathrm{B}}T\Gamma(q, \bar{\ell})\delta(t - t').$$ (6.22)

6.2.4 Hydrodynamic decay rate

We first introduce $\bar{t} \equiv 4\eta\bar{\ell}^3/\kappa$ as a characteristic time. In Fig. 6.2, we plot the scaled decay rate $\gamma(q, \bar{\ell}, \xi)\bar{t}$ (see Eq. (6.18)) as a function of the dimensionless wavenumber $q\bar{\ell}$ when $\Xi = \xi/\bar{\ell} = 10$ and 0.1. For our later discussion, it is useful here to discuss its asymptotic behaviors. We first note that the kinetic coefficient $\Gamma(q, \bar{\ell})$ in Eq. (6.19) behaves as

$$
\Gamma \approx \begin{cases} \bar{\ell}^3 q^2/12\eta, & q \ll 1/\bar{\ell} \\ 1/4\eta q, & q \gg 1/\bar{\ell}. \end{cases} \tag{6.23}
$$

Depending on the relative magnitude between $\bar{\ell}$ and ξ, two different asymptotic behaviors of the decay rate can be distinguished [6.26]. For $\bar{\ell} \ll \xi$ (corresponding to $\Xi = 10$ in Fig. 6.2), the decay rate increases monotonically as

$$
\gamma \approx \begin{cases} \kappa\bar{\ell}^3 q^2/12\eta\xi^4, & q \ll 1/\xi \\ \kappa\bar{\ell}^3 q^6/12\eta, & 1/\xi \ll q \ll 1/\bar{\ell} \\ \kappa q^3/4\eta, & 1/\bar{\ell} \ll q. \end{cases} \tag{6.24}
$$

The small-q behavior $\gamma \sim q^2$ results from the conservation of the fluid volume between the membrane and the wall [6.32]. The dependence $\gamma \sim q^6$ in the intermediate regime, where the effect of potential becomes irrelevant, was predicted by Brochard and Lennon [6.9]. For large q, we recover the behavior of a free membrane $\gamma \sim q^3$. All these asymptotic behaviors are observed in Fig. 6.2.

For $\xi \ll \bar{\ell}$ (corresponding to $\Xi = 0.1$ in Fig. 6.2), on the other hand, γ changes non-monotonically as [6.26]

$$
\gamma \approx \begin{cases} \kappa\bar{\ell}^3 q^2/12\eta\xi^4, & q \ll 1/\bar{\ell} \\ \kappa/4\eta\xi^4 q, & 1/\bar{\ell} \ll q \ll 1/\xi \\ \kappa q^3/4\eta. & 1/\xi \ll q. \end{cases} \tag{6.25}
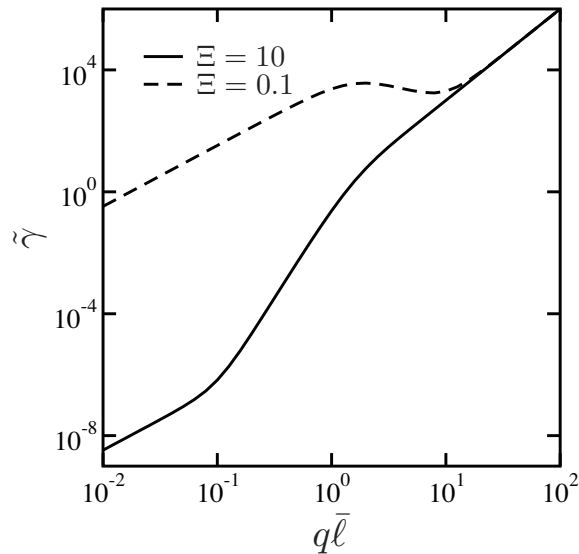$$

Figure 6.2: Dimensionless decay rate $\tilde{\gamma} \equiv \gamma \bar{t}$ (see Eq. (6.18)) with $\bar{t} = 4\eta \bar{\ell}^3/\kappa$ as a function of dimensionless wavenumber $q\bar{\ell}$. The solid and dashed lines represent $\Xi = \xi/\bar{\ell} = 10$ and 0.1, respectively.

While the small-q and large-q behaviors are unchanged from Eq. (6.24), here the decay rate decreases with increasing q in the intermediate range. This unusual decrease of the decay rate clearly appears for $1 < q\bar{\ell} < 10$ in Fig. 6.2. Such an anomalous behavior occurs due to the fact that the potential confines the mean-square fluctuation amplitudes to $\langle h^2 \rangle \approx k_{\mathrm{B}} T \xi^4/\kappa$ independently of q (see Eq. (6.4)), while hydrodynamic damping becomes less effective with increasing q [6.26]. We also note that the absolute value of γ in the small-q region is sensitive to the value of Ξ, while it is independent of Ξ in the large-q region.

6.3   Membrane two-point correlation functions

Using the result of the hydrodynamic calculation, we shall discuss in this section the two-point correlation functions of bound membranes [6.33, 6.34]. We separately investigate the cases of (i) a static wall, (ii) an active wall, and (iii) an active wall with an intrinsic time scale.
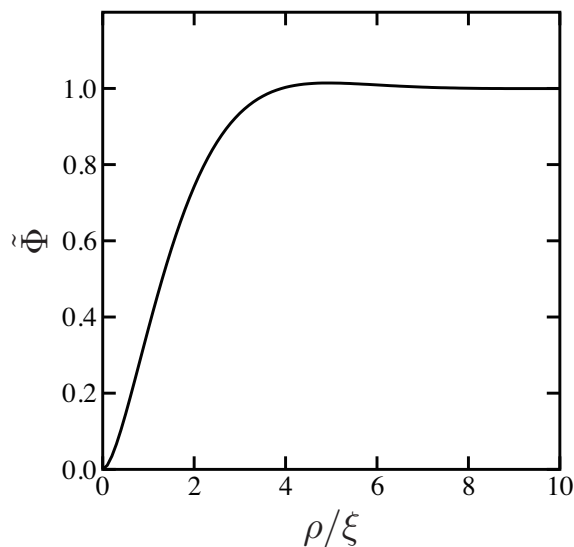
6.3.1 Static wall

Figure 6.3: Dimensionless static correlator $\tilde{\Phi} \equiv (4\kappa/k_{\mathrm{B}}T\xi^2)\Phi$ in the presence of a static wall (see Eq. (6.31)) as a function of dimensionless distance ρ/ξ. Notice that $\tilde{\Phi}$ takes a maximum value at $\rho/\xi = 4.93$.

In the case of a static wall, the velocities at the wall vanish in Eqs. (6.7) and (6.8), i.e., $V_{x0}(\boldsymbol{q},t) = V_{z0}(\boldsymbol{q},t) = 0$. Hence Eq. (6.17) reduces to

$$\frac{\partial h(\boldsymbol{q},t)}{\partial t} = -\gamma(q,\bar{\ell},\xi)h(\boldsymbol{q},t) + \zeta(\boldsymbol{q},t), \tag{6.26}$$

and one can easily solve for $h(\boldsymbol{q},t)$ as

$$h(\boldsymbol{q},t) = h(\boldsymbol{q},0)e^{-\gamma(q,\bar{\ell},\xi)t} + \int_0^t dt_1\, \zeta(\boldsymbol{q},t_1)e^{-\gamma(q,\bar{\ell},\xi)(t-t_1)}. \tag{6.27}$$

Using the above solution and Eq. (6.22), we calculate the membrane two-point correlation function which can be separated into two parts [6.33, 6.34]

$$\langle [h(\boldsymbol{\rho},t) - h(\boldsymbol{\rho}',0)]^2 \rangle = \Phi(\boldsymbol{\rho} - \boldsymbol{\rho}') + \phi(\boldsymbol{\rho} - \boldsymbol{\rho}',t), \tag{6.28}$$

where the translational invariance of the system has been assumed. In the above,

101

the first term is a purely static correlator

$$\Phi(\boldsymbol{\rho} - \boldsymbol{\rho}') = \langle [h(\boldsymbol{\rho}) - h(\boldsymbol{\rho}')]^2 \rangle$$

$$= 2 \int \frac{d^2q}{(2\pi)^2} \langle h(\boldsymbol{q}) h(-\boldsymbol{q}) \rangle \left[1 - e^{i\boldsymbol{q}\cdot(\boldsymbol{\rho} - \boldsymbol{\rho}')} \right], \qquad (6.29)$$

describing the static membrane roughness, while the second term is a dynamical correlator

$$\phi(\boldsymbol{\rho} - \boldsymbol{\rho}', t) = 2 \int \frac{d^2q}{(2\pi)^2} \langle h(\boldsymbol{q}) h(-\boldsymbol{q}) \rangle e^{i\boldsymbol{q}\cdot(\boldsymbol{\rho} - \boldsymbol{\rho}')} \left[1 - e^{-\gamma(q,\bar{\ell},\xi)t} \right], \qquad (6.30)$$

describing the propagation of fluctuations with a distance $|\boldsymbol{\rho} - \boldsymbol{\rho}'|$.

Using the static correlation function for $h(\boldsymbol{q})$ in Eq. (6.4), we first calculate the static correlator

$$\Phi(\boldsymbol{\rho} - \boldsymbol{\rho}') = \frac{k_{\mathrm{B}}T}{\pi\kappa} \int_0^\infty dq \, \frac{q}{q^4 + \xi^{-4}} [1 - J_0(q|\boldsymbol{\rho} - \boldsymbol{\rho}'|)]$$

$$= \frac{k_{\mathrm{B}}T\xi^2}{4\kappa} \left[1 - \frac{1}{\pi} G_{0,4}^{3,0} \left(\frac{(|\boldsymbol{\rho} - \boldsymbol{\rho}'|/\xi)^4}{256} \middle| \, 0, \tfrac{1}{2}, \tfrac{1}{2}, 0 \, \right) \right], \qquad (6.31)$$

where $J_0(z)$ is the zero-order Bessel function of the first kind, and the Meijer G-function is used in the last expression [6.35]. In Fig. 6.3, we plot the scaled static correlator $\Phi(\boldsymbol{\rho} - \boldsymbol{\rho}')$ as a function of ρ/ξ where $\rho = |\boldsymbol{\rho} - \boldsymbol{\rho}'|$. Only in this plot, we use ξ to scale the length because the above static correlator is solely determined by the free energy in Eq. (6.2), and Eq. (6.31) does not depend on $\bar{\ell}$. In the large distance $\rho/\xi \gg 1$, the (route mean square) height difference between two points on the bound membrane is proportional to ξ. It is interesting to note that $\Phi(\boldsymbol{\rho} - \boldsymbol{\rho}')$ changes non-monotonically and shows a maximum around $\rho/\xi \approx 4.93$. A similar overshoot behavior of the membrane profile was reported before [6.36].

As for the dynamical correlator in Eq. (6.30), we perform the angular integration and obtain the expression

$$\phi(\boldsymbol{\rho} - \boldsymbol{\rho}', t) = \frac{k_{\mathrm{B}}T}{\pi\kappa} \int_0^\infty dq \, \frac{q}{q^4 + \xi^{-4}} \left[1 - e^{-\gamma(q,\bar{\ell},\xi)t} \right] J_0(q|\boldsymbol{\rho} - \boldsymbol{\rho}'|). \qquad (6.32)$$

We first set $\boldsymbol{\rho} = \boldsymbol{\rho}'$ and discuss the mean squared displacement (MSD) of a tagged membrane segment given by [6.33, 6.34]

$$\phi_0(t) = \frac{k_\mathrm{B}T}{\pi\kappa} \int_0^\infty dq \, \frac{q}{q^4 + \xi^{-4}} \left[1 - e^{-\gamma(q,\bar{\ell},\xi)t} \right], \qquad (6.33)$$

where we have used $J_0(0) = 1$. Instead of the correlation length ξ, we hereafter use $\bar{\ell}$ to scale the length. Note that the hydrodynamic effect is manifested by the appearance of the length $\bar{\ell}$. In Fig. 6.4, we plot the dimensionless MSD ϕ_0 as a function of $t/\bar{t}$ (recall that $\bar{t} = 4\eta\bar{\ell}^3/\kappa$) for $\Xi = 10$ (monotonic damping case) and $\Xi = 0.1$ (non-monotonic damping case), respectively. In order to find out the asymptotic behaviors clearly, we have also plotted an effective growth exponent α defined by

$$\alpha(t) = \frac{d \ln \phi_0(t)}{d \ln t}. \qquad (6.34)$$

For both $\Xi = 10$ and 0.1, the MSD increases monotonically as a function of time. For $\Xi = 10$ ($\bar{\ell} \ll \xi$), there are three different asymptotic regimes of the time dependence. In the small time regime ($t \ll \bar{t}$), the MSD behaves as $\phi_0 \sim t^{2/3}$ which corresponds to the diffusion of a free membrane [6.33, 6.34]. This scaling behavior can be obtained by using the large-q behavior of the decay rate in Eq. (6.24)

$$\begin{aligned}
\phi_0(t) &\approx \frac{k_\mathrm{B}T}{\pi\kappa} \int_0^\infty dq \, \frac{1}{q^3} \left[1 - e^{-(\kappa q^3/4\eta)t} \right] \\
&\sim \frac{k_\mathrm{B}T}{\kappa^{1/3}\eta^{2/3}} t^{2/3}.
\end{aligned} \qquad (6.35)$$

In the intermediate time regime ($\bar{t} \ll t \ll \Xi^6 \bar{t}$), we have $\phi_0 \sim t^{1/3}$ which stems from the intermediate-q behavior of γ in Eq. (6.24)

$$\begin{aligned}
\phi_0(t) &\approx \frac{k_\mathrm{B}T}{\pi\kappa} \int_0^\infty dq \, \frac{1}{q^3} \left[1 - e^{-(\kappa\bar{\ell}^3 q^6/12\eta)t} \right] \\
&\sim \frac{k_\mathrm{B}T\bar{\ell}}{\kappa^{2/3}\eta^{1/3}} t^{1/3}.
\end{aligned} \qquad (6.36)$$

In this regime, as discussed by Brochard and Lennon [6.9], the conservation of the enclosed incompressible volume between the membrane and the wall is important, while the effect of the potential acting between them is irrelevant. The Fourier transform of the above expression, i.e., the power spectral density, was previously discussed by Gov *et al.* in Ref. [6.16]. In the long time regime ($\Xi^6 \bar{t} \ll t$), the MSD saturates at the value given by

$$\phi_0(t \to \infty) \approx \left[\frac{k_{\mathrm{B}} T \bar{\ell}^2}{\pi \kappa} \right] \frac{\pi \Xi^2}{4} \sim \frac{k_{\mathrm{B}} T}{\kappa} \xi^2. \tag{6.37}$$

For $\Xi = 0.1$ ($\xi \ll \bar{\ell}$), on the other hand, there are only two asymptotic regimes. The MSD increases as $\phi_0 \sim t^{2/3}$ in the small time regime ($t \ll \Xi^3 \bar{t}$), whereas in the long time regime ($\Xi^3 \bar{t} \ll t$), it saturates at the value given by Eq. (6.37).

Let us consider then the case $\boldsymbol{\rho} \neq \boldsymbol{\rho}'$. In Fig. 6.5, we plot the scaled $\phi(\boldsymbol{\rho} - \boldsymbol{\rho}', t)$ in Eq. (7.16) as a function of $\rho/\bar{\ell}$ for different times when $\Xi = 10$. For all the cases, the dynamic correlator changes non-monotonically and exhibits a typical undershoot behavior. The minimum of ϕ occurs for larger ρ as time evolves. In the long time limit, $t \to \infty$, $\phi(\boldsymbol{\rho} - \boldsymbol{\rho}', t)$ in Eq. (7.16) coincides with the second term in Eq. (6.31) and is given by the Meijer G-function.

6.3.2 Active wall

We now investigate the case when the wall is active so that it exerts random velocities on the ambient fluid. The membrane dynamics in the presence of an active wall is described by Eq. (6.17). This equation can be also solved for $h(\boldsymbol{q}, t)$ as

$$\begin{aligned} h(\boldsymbol{q}, t) =&\, h(\boldsymbol{q}, 0) e^{-\gamma(q, \bar{\ell}, \xi) t} + \Lambda_x(q, \bar{\ell}) \int_0^t dt_1\, V_{x0}(\boldsymbol{q}, t_1) e^{-\gamma(q, \bar{\ell}, \xi)(t - t_1)} \\ &+ \Lambda_z(q, \bar{\ell}) \int_0^t dt_2\, V_{z0}(\boldsymbol{q}, t_2) e^{-\gamma(q, \bar{\ell}, \xi)(t - t_2)} + \int_0^t dt_3\, \zeta(\boldsymbol{q}, t_3) e^{-\gamma(q, \bar{\ell}, \xi)(t - t_3)}. \end{aligned} \tag{6.38}$$

The random velocities generated at the wall are assumed to have the following statistical properties

$$\langle V_{x0}(\boldsymbol{\rho}, t)\rangle = \langle V_{z0}(\boldsymbol{\rho}, t)\rangle = 0, \tag{6.39}$$

$$\langle V_{x0}(\boldsymbol{\rho}, t)V_{x0}(\boldsymbol{\rho}', t')\rangle = 2S_x\delta(\boldsymbol{\rho} - \boldsymbol{\rho}')\delta(t - t'), \tag{6.40}$$

$$\langle V_{z0}(\boldsymbol{\rho}, t)V_{z0}(\boldsymbol{\rho}', t')\rangle = 2S_z\delta(\boldsymbol{\rho} - \boldsymbol{\rho}')\delta(t - t'), \tag{6.41}$$

$$\langle V_{x0}(\boldsymbol{\rho}, t)V_{z0}(\boldsymbol{\rho}', t')\rangle = 0, \tag{6.42}$$

$$\langle V_{x0}(\boldsymbol{\rho}, t)\zeta(\boldsymbol{\rho}', t')\rangle = \langle V_{z0}(\boldsymbol{\rho}, t)\zeta(\boldsymbol{\rho}', t')\rangle = 0, \tag{6.43}$$

where we have introduced the amplitudes S_x and S_z in Eqs. (6.40) and (6.41), respectively. With these statistical properties, we can calculate the total two-point correlation function which consists of the static and the dynamical parts as before

$$\langle [h(\boldsymbol{\rho}, t) - h(\boldsymbol{\rho}', 0)]^2\rangle_{\mathrm{tot}} = \Phi_{\mathrm{tot}}(\boldsymbol{\rho} - \boldsymbol{\rho}') + \phi_{\mathrm{tot}}(\boldsymbol{\rho} - \boldsymbol{\rho}', t). \tag{6.44}$$

In the above total correlation function, the static correlator in the presence of the active wall becomes

$$
\begin{aligned}
&\Phi_{\mathrm{tot}}(\boldsymbol{\rho} - \boldsymbol{\rho}') \\
&= \frac{1}{\pi} \int_0^\infty dq\, q \left[\frac{k_{\mathrm{B}}T}{\kappa(q^4 + \xi^{-4})} + \frac{S_x|\Lambda_x(q, \bar{\ell})|^2}{\gamma(q, \bar{\ell}, \xi)} + \frac{S_z|\Lambda_z(q, \bar{\ell})|^2}{\gamma(q, \bar{\ell}, \xi)} \right] [1 - J_0(q|\boldsymbol{\rho} - \boldsymbol{\rho}'|)] \\
&\equiv \Phi(\boldsymbol{\rho} - \boldsymbol{\rho}') + \Phi_x(\boldsymbol{\rho} - \boldsymbol{\rho}') + \Phi_z(\boldsymbol{\rho} - \boldsymbol{\rho}'), \tag{6.45}
\end{aligned}
$$

where Λ_x and Λ_z were obtained in Eqs. (6.20) and (6.21), respectively, while $\Phi(\boldsymbol{\rho} - \boldsymbol{\rho}')$ was defined in Eq. (6.31) for the static wall case. In the above equations, we have defined two correlators Φ_x and Φ_z. On the other hand, the dynamical correlator in Eq. (6.44) is given by

$$\phi_{\text{tot}}(\boldsymbol{\rho} - \boldsymbol{\rho}', t) = \frac{1}{\pi} \int_0^\infty dq\, q \left[\frac{k_{\text{B}}T}{\kappa(q^4 + \xi^{-4})} + \frac{S_x |\Lambda_x(q, \bar{\ell})|^2}{\gamma(q, \bar{\ell}, \xi)} + \frac{S_z |\Lambda_z(q, \bar{\ell})|^2}{\gamma(q, \bar{\ell}, \xi)} \right]$$
$$\times \left[1 - e^{-\gamma(q, \bar{\ell}, \xi)t} \right] J_0(q|\boldsymbol{\rho} - \boldsymbol{\rho}'|). \tag{6.46}$$

By setting $\boldsymbol{\rho} = \boldsymbol{\rho}'$, the total MSD of a tagged membrane segment in the presence of the active wall becomes

$$\phi_{\text{tot}}(t) = \frac{1}{\pi} \int_0^\infty dq\, q \left[\frac{k_{\text{B}}T}{\kappa(q^4 + \xi^{-4})} + \frac{S_x |\Lambda_x(q, \bar{\ell})|^2}{\gamma(q, \bar{\ell}, \xi)} + \frac{S_z |\Lambda_z(q, \bar{\ell})|^2}{\gamma(q, \bar{\ell}, \xi)} \right] \left[1 - e^{-\gamma(q, \bar{\ell}, \xi)t} \right]$$
$$\equiv \phi_0(t) + \phi_{x0}(t) + \phi_{z0}(t), \tag{6.47}$$

where the first term $\phi_0(t)$ was defined before in Eq. (6.33) for the static wall case, while ϕ_{x0} and ϕ_{z0} have been newly defined here.

Before showing the result of MSD, we first discuss the wavenumber dependencies of the quantities $|\Lambda_x|^2/\gamma$ and $|\Lambda_z|^2/\gamma$ appearing in Eqs. (6.45)–(6.47). These quantities originating from the active wall are plotted in Fig. 6.6 as a function of $q\bar{\ell}$ for $\Xi = 10$ and 0.1. Using the asymptotic behaviors of γ, as shown in Eqs. (6.24) and (6.25), we can obtain the limiting expressions for $|\Lambda_x|^2/\gamma$ and $|\Lambda_z|^2/\gamma$ as well. When $\bar{\ell} \ll \xi$ (corresponding to $\Xi = 10$), we have

$$|\Lambda_x|^2/\gamma \approx \begin{cases} 3\eta\xi^4/\kappa\bar{\ell}, & q \ll 1/\xi \\ 3\eta/\kappa\bar{\ell}q^4, & 1/\xi \ll q \ll 1/\bar{\ell} \\ 4\eta\bar{\ell}^2 e^{-2\bar{\ell}q}/\kappa q, & 1/\bar{\ell} \ll q, \end{cases} \tag{6.48}$$

$$|\Lambda_z|^2/\gamma \approx \begin{cases} 12\eta\xi^4/\kappa\bar{\ell}^3 q^2, & q \ll 1/\xi \\ 12\eta/\kappa\bar{\ell}^3 q^6, & 1/\xi \ll q \ll 1/\bar{\ell} \\ 4\eta\bar{\ell}^2 e^{-2\bar{\ell}q}/\kappa q, & 1/\bar{\ell} \ll q. \end{cases} \qquad (6.49)$$

For $\xi \ll \bar{\ell}$ (corresponding to $\Xi = 0.1$), on the other hand, we obtain

$$|\Lambda_x|^2/\gamma \approx \begin{cases} 3\eta\xi^4/\kappa\bar{\ell}, & q \ll 1/\bar{\ell} \\ 4\eta\xi^4\bar{\ell}^2 q^3 e^{-2\bar{\ell}q}/\kappa, & 1/\bar{\ell} \ll q \ll 1/\xi \\ 4\eta\bar{\ell}^2 e^{-2\bar{\ell}q}/\kappa q, & 1/\xi \ll q, \end{cases} \qquad (6.50)$$

$$|\Lambda_z|^2/\gamma \approx \begin{cases} 12\eta\xi^4/\kappa\bar{\ell}^3 q^2, & q \ll 1/\bar{\ell} \\ 4\eta\xi^4\bar{\ell}^2 q^3 e^{-2\bar{\ell}q}/\kappa, & 1/\bar{\ell} \ll q \ll 1/\xi \\ 4\eta\bar{\ell}^2 e^{-2\bar{\ell}q}/\kappa q. & 1/\xi \ll q. \end{cases} \qquad (6.51)$$

The static correlators Φ_x and Φ_z defined in Eq. (6.45) due to the active wall can now be obtained by performing numerical integrals. In Fig. 6.7, we plot the static correlators Φ_x and Φ_z as a function of ρ/ℓ when $\Xi = 10$. Here Φ_x and Φ_z are scaled by $4\eta\bar{\ell}S_x/\pi\kappa$ and $4\eta\bar{\ell}S_z/\pi\kappa$, respectively. We notice that Φ_x behaves similarly to that of the static wall case Φ given in Eq. (6.31) and plotted in Fig. 6.3. On the other hand, Φ_z diverges logarithmically for large $\rho/\bar{\ell}$ because the integral is found to be infrared divergent. Such a logarithmic divergence is avoided when we consider a finite membrane size which gives rise to a cutoff for small wavenumbers in the integral of Eq. (6.45). It should be noted that both Φ_x and Φ_z depend on $\bar{\ell}$ and ξ, while Φ is solely determined by ξ. This means that Φ_x and Φ_z include the geometrical as well as the hydrodynamic effects.

In Figs. 6.8 and 6.9, we plot the scaled membrane MSD ϕ_{x0} and ϕ_{z0} (see Eq. (6.47)), respectively, as a function of $t/\bar{t}$ when $\Xi = 10$ and 0.1. For $\bar{\ell} \ll \xi$ (corresponding to $\Xi = 10$), there are three different asymptotic regimes both for

107

ϕ_{x0} and ϕ_{z0}. In the small time regime ($t \ll \bar{t}$), we have $\phi_{x0} \sim t$ and $\phi_{z0} \sim t$, showing a normal diffusive behavior. This is because ϕ_{x0} can be approximated as

$$\begin{aligned}
\phi_{x0}(t) &\approx \frac{4\eta \bar{\ell}^2 S_x}{\pi \kappa} \int_0^\infty dq \, e^{-2\bar{\ell}q} \left[1 - e^{-(\kappa q^3/4\eta)t} \right] \\
&\approx \frac{\bar{\ell}^2 S_x t}{\pi} \int_0^\infty dq \, e^{-2\bar{\ell}q} q^3 \sim \frac{S_x}{\bar{\ell}^2} t.
\end{aligned} \tag{6.52}$$

Notice that only small-q contributes to the integral, and the same holds for ϕ_{z0}. In the intermediate time regime ($\bar{t} \ll t \ll \Xi^6 \bar{t}$), we have $\phi_{x0} \sim t^{1/3}$ and $\phi_{z0} \sim t^{2/3}$ which can be asymptotically obtained by Eqs. (6.36) and (6.35), respectively. In the long time regime ($\Xi^6 \bar{t} \ll t$), ϕ_{x0} saturates at the value

$$\phi_{x0}(t \to \infty) \approx \left[\frac{4\eta \bar{\ell} S_x}{\pi \kappa} \right] \frac{3\Xi^2}{8} \sim \frac{\eta \xi^2 S_x}{\kappa \bar{\ell}}. \tag{6.53}$$

On the other hand, ϕ_{z0} diverges logarithmically for $t \to \infty$, which can be seen in Fig. 6.9(a) and also shown analytically. Such a divergence in time occurs for small q and can be avoided when the membrane size is finite as mentioned before.

For $\xi \ll \bar{\ell}$ (corresponding to $\Xi = 0.1$), on the other hand, there are only two asymptotic regimes. The MSDs increase both linearly as $\phi_{x0} \sim t$ and $\phi_{z0} \sim t$ in the small time regime ($t \ll \Xi^3 \bar{t}$). In the long time regime ($\Xi^3 \bar{t} \ll t$), ϕ_{x0} saturates at the value

$$\phi_{x0}(t \to \infty) \approx \left[\frac{4\eta \bar{\ell} S_x}{\pi \kappa} \right] \frac{3\Xi^4}{8} \sim \frac{\eta \xi^4 S_x}{\kappa \bar{\ell}^3}, \tag{6.54}$$

while ϕ_{z0} also diverges logarithmically as above.

6.3.3 Active wall with an intrinsic time scale

Finally we consider a situation in which the activity of the wall occurs over a finite time scale τ. In this case, the statistical properties of random velocities which have been given in Eqs. (6.40) and (6.41) would be replaced by the following exponential

correlation function in time [6.19, 6.20, 6.42]

$$\langle V_{x0}(\boldsymbol{\rho}, t) V_{x0}(\boldsymbol{\rho}', t') \rangle = \frac{S_x}{\tau} \delta(\boldsymbol{\rho} - \boldsymbol{\rho}') e^{-|t-t'|/\tau}, \qquad (6.55)$$

$$\langle V_{z0}(\boldsymbol{\rho}, t) V_{z0}(\boldsymbol{\rho}', t') \rangle = \frac{S_z}{\tau} \delta(\boldsymbol{\rho} - \boldsymbol{\rho}') e^{-|t-t'|/\tau}, \qquad (6.56)$$

while the other velocity correlations remain the same. In general, the intrinsic time scale τ can be different between the x- and z-components. In the above relations, we have put a factor $1/\tau$ so that the physical dimension of S_x and S_z is the same as before.

Repeating the same procedure as before, we obtain the total two-point correlation function which can be also separated into the static and dynamics parts as in Eq. (6.44). The static correlators in the presence of the active wall now become

$$\Phi_x(\boldsymbol{\rho} - \boldsymbol{\rho}') = \frac{1}{\pi} \int_0^\infty dq\, q \frac{S_x |\Lambda_x(q, \bar{\ell})|^2}{\gamma(q, \bar{\ell}, \xi)[\gamma(q, \bar{\ell}, \xi)\tau + 1]} [1 - J_0(q|\boldsymbol{\rho} - \boldsymbol{\rho}'|)], \qquad (6.57)$$

$$\Phi_z(\boldsymbol{\rho} - \boldsymbol{\rho}') = \frac{1}{\pi} \int_0^\infty dq\, q \frac{S_z |\Lambda_z(q, \bar{\ell})|^2}{\gamma(q, \bar{\ell}, \xi)[\gamma(q, \bar{\ell}, \xi)\tau + 1]} [1 - J_0(q|\boldsymbol{\rho} - \boldsymbol{\rho}'|)]. \qquad (6.58)$$

A similar static correlator was previously discussed by Gov *et al.* [6.19, 6.20, 6.42]. Notice that the above expressions reduce to those in Eq. (6.45) when $\tau \to 0$. This is reasonable because the exponential function in Eqs. (6.55) and (6.56) reduce to a δ-function in the limit of $\tau \to 0$.

Similarly, the two MSD functions of a tagged membrane segment are given by

$$\phi_{x0}(t) = \frac{1}{\pi} \int_0^\infty dq\, q \frac{S_x |\Lambda_x(q, \bar{\ell})|^2}{\gamma(q, \bar{\ell}, \xi)[\gamma(q, \bar{\ell}, \xi)\tau + 1]} \left[1 - e^{-\gamma(q, \bar{\ell}, \xi)t}\right], \qquad (6.59)$$

$$\phi_{z0}(t) = \frac{1}{\pi} \int_0^\infty dq\, q \frac{S_z |\Lambda_z(q, \bar{\ell})|^2}{\gamma(q, \bar{\ell}, \xi)[\gamma(q, \bar{\ell}, \xi)\tau + 1]} \left[1 - e^{-\gamma(q, \bar{\ell}, \xi)t}\right], \qquad (6.60)$$

which also reduce to those in Eq. (6.47) when $\tau \to 0$. In Figs. 6.10 and 6.11, we plot the scaled ϕ_{x0} and ϕ_{z0}, respectively, as a function of $t/\bar{t}$ for different τ-values when $\Xi = 10$. We first notice that both ϕ_{x0} and ϕ_{z0} decrease when the intrinsic time scale τ is taken into account. Also the initial time regions during which ϕ_{x0} and ϕ_{z0} grow linearly in time increase for larger τ-values, and the regions showing the scaling $\phi_{x0} \sim t^{1/3}$ or $\phi_{z0} \sim t^{2/3}$ become narrower. In the large τ limit, there will be only two scaling regimes of the MSDs.

6.4   Summary and discussion

In this paper, we have discussed the dynamics of a membrane interacting with an active wall that generates random velocities. We have generally shown that the dynamics of a bound membrane is significantly affected by active fluctuations at the wall and they propagate through the surrounding fluid. Using the result of the hydrodynamic calculation of a bound membrane, we have derived a dynamic equation for the membrane fluctuation amplitude (see Eq. (6.17)). As noted by Seifert before [6.26], there are two different asymptotic behaviors of the hydrodynamic decay rate γ depending on the relative magnitude between the average membrane-wall distance $\bar{\ell}$ and the correlation length ξ (see Eqs. (6.24) and (6.25)). We have obtained in Sec. 6.3 the membrane two-point correlation functions for three different wall cases; (i) a static wall, (ii) an active wall, and (iii) an active wall with an intrinsic time scale.

As a dynamic part of the correlation function, we have mainly discussed the MSD of a tagged membrane and investigated its asymptotic time dependencies for the different types of walls. For the static wall case, the membrane fluctuates due to thermal agitations. When the decay rate γ changes monotonically, the MSD given by Eq. (6.33) exhibits two asymptotic behaviors $\phi_0 \sim t^{2/3}$ and $\phi_0 \sim t^{1/3}$ before it reaches a constant value that is fixed by ξ (see Fig.6.4). When the wall is active, on the other hand, the partial MSDs in Eq. (6.47) grow linearly in time, $\phi_{x0} \sim \phi_{z0} \sim t$, in the early stage. Compared to the dynamics due to thermal

fluctuations, this is a unique behavior of a membrane segment in the presence of an active wall (see Figs. 6.8 and 6.9). When the active wall has a finite intrinsic time scale τ as defined in Eqs. (6.55) and (6.56), the linear-growth region of the MSD is further extended as τ is increased.

The present work should be distinguished from those dealing with the dynamics of "active membranes" [6.8]. These membranes contain active proteins such as ion pumps which consume the chemical energy and drive the membrane out of equilibrium. Being motivated by the theoretical predictions [6.37–6.43], some experiments have shown that active forces enhance membrane fluctuations [6.44–6.46]. In our theory, we have considered that the active components are incorporated not in the membrane but in the wall, and discussed their hydrodynamic effects on the membrane fluctuations. Hence our work is related to the recent work by Maitra et $al.$ [6.47] who discussed the dynamics of a membrane coupled to an actin cortex consisting of filaments with active stresses and currents.

For our further discussion, we give here some numerical estimates of the quantities used in our calculations. As an example, we consider the shape fluctuations of RBCs. Previously, the data for normal RBC [6.48] was well described by using the following parameters [6.19, 6.20]; $\kappa \sim 10^{-19}$ J, $\bar{\ell} \sim 2 - 3 \times 10^{-8}$ m, and $\xi \sim 2 - 3 \times 10^{-7}$ m. Then the important dimensionless parameter is roughly $\Xi = \xi/\bar{\ell} \sim 10$ for RBCs, and the decay rate γ is expected to increase monotonically as in Eq. (6.24). Using the value of water viscosity $\eta \sim 10^{-3}$ J/m^3, we obtain the characteristic time scale as $\bar{t} = 4\eta\bar{\ell}^3/\kappa \sim 10^{-7}$ s. Hence the second crossover time scale discussed in Eq. (6.36) is roughly given by $\Xi^6\bar{t} \sim 10^{-1}$ s. Since $\bar{t}$ and $\Xi^6\bar{t}$ are well separated, the three different asymptotic regimes of $\phi_0(t)$ should be clearly observable.

The intrinsic time scale τ appearing in Eqs. (6.55) and (6.56) represents the duration of force production at the active wall, and can be roughly estimated as $\tau \sim 10^{-3}$ s for the spectrin network of RBCs [6.19, 6.20]. Hence the choice of $\tau/\bar{t} \sim 10^4$ in Figs. 6.10 or 6.11 is reasonable. Moreover, the force balance between the spectrin compression and the membrane bending yields a characteristic length

scale of the order of $L \sim 10^{-7}$ m. From the viewpoint of dimensional analysis, the quantities S_x and S_z, which fix the amplitudes of the random velocities in Eq. (6.40) and (6.41), respectively, can be evaluated as $S_x \sim L^4/\tau \sim 10^{-24}$ m^4/s and similarly for S_z. With this value, the amplitude of the MSD due to the active wall becomes $\phi_{x0} \sim \eta\bar{\ell}S_x/\kappa \sim 10^{-17}$ m^2. This value is comparable to that of thermal fluctuations $\phi_0 \sim k_{\mathrm{B}}T\bar{\ell}^2/\kappa \sim 10^{-16}$ m^2.

As mentioned in Sec. 6.2, the decay rate γ changes non-monotonically when $\Xi \ll 1$. This situation may occur for a charged membrane pushed by an osmotic pressure [6.26]. When unscreened electrostatic interactions compete with an osmotic pressure, the condition $\Xi \ll 1$ is met whenever $\bar{\ell} \gg \kappa\ell_{\mathrm{B}}/k_{\mathrm{B}}T \sim 5 \times 10^{-9}$ m where ℓ_{B} is the Bjerrum length. As the unbinding transition point is approached [6.28], $\bar{\ell}$ becomes much larger than ξ.

Following the calculation by Seifert [6.26], we have shown in Sec. 6.2 that the hydrodynamic kinetic coefficient $\Gamma(q, \bar{\ell})$ is given by Eq. (6.19). In Ref. [6.17], Gov *et al.* used different boundary conditions at the membrane and obtained an alternative expression for the kinetic coefficient

$$\Gamma_{\mathrm{G}}(q, \bar{\ell}) = \frac{e^{-2q\bar{\ell}}}{4\eta q} \left[e^{2q\bar{\ell}} - 1 - 2q\bar{\ell} - 2(q\bar{\ell})^2 \right]. \tag{6.61}$$

As expressed in Eq. (6.14), Seifert and we have used an incompressibility condition for the fluid near the membrane, whereas Gov *et al.* employed a zero-shear-stress condition, which implies that the xz-component of the shear on both sides of the membrane are equal. Gov *et al.* insisted that the latter condition is appropriate for a fluid membrane which cannot support shear stress across its width [6.17]. We have quantitatively compared Eqs. (6.19) and (6.61) and confirmed that they only differ by a numerical factor of 4 in the small-q regime, and the asymptotic scaling behaviors are completely identical. Notice that $\Gamma_{\mathrm{G}}(q, \bar{\ell})$ in Eq. (6.61) behaves as

$$\Gamma_{\mathrm{G}} \approx \begin{cases} \bar{\ell}^3 q^2/3\eta, & q \ll 1/\bar{\ell} \\ 1/4\eta q, & q \gg 1/\bar{\ell}, \end{cases} \tag{6.62}$$

which can be compared with Eq. (6.23). In any case, the differences between Eqs. (6.19) and (6.61) are not significant as far as the role of the wall is concerned, and various scaling behaviors of the MSD discussed in this paper are valid.

In this paper, we have only dealt with a tensionless membrane whose shape is governed by Eq. (6.1). In Ref. [6.16], it was claimed that the attachment of the cytoskeleton to the membrane would induce an effective surface tension. For a membrane with a finite surface tension Σ, the free energy is modified to

$$F = \int d^2\rho \left[\frac{\kappa}{2}(\nabla^2\ell)^2 + V(\ell) + \frac{\Sigma}{2}(\nabla\ell)^2 \right]. \qquad (6.63)$$

Hence the quantity E in the static correlation function Eq. (6.4) should now be replaced with

$$E(q,\xi) = \kappa(q^4 + \xi^{-4}) + \Sigma q^2. \qquad (6.64)$$

The new term associated with the surface tension neither modifies the small wavenumber nor the large wavenumber asymptotic behaviors [6.26]. Although a more complicated crossover behavior can arise in the intermediate wavenumber if $\Sigma > \kappa/\xi^2$, we do not discuss it here because our main aim is to see the effects of the active wall. In general, the presence of the finite surface tension tends to suppress the membrane fluctuations.

In our model, the outer fluid is assumed to be purely viscous characterized by a constant viscosity η. It should be noted, however, fluids surrounding biomembranes are viscoelastic rather than purely viscous. This is a common situation in all eukaryotic cells whose cytoplasm is a soup of proteins and organelles, including a thick sub-membrane layer of actin-meshwork forming a part of the cell cytoskeleton [6.12]. The extra-cellular fluid can also be viscoelastic because it is filled with extracellular matrix or hyaluronic acid gel. In order to mimic the real situations, the dynamics of undulating bilayer membrane surrounded by viscoelastic media was considered before [6.49, 6.50]. It was assumed that both sides of the membrane are occupied by viscoelastic media with a frequency-dependent modulus that

113

obeys a power-law behavior $G(\omega) = G_0(i\omega)^\beta$ with $0 \le \beta \le 1$ [6.49–6.52]. Such a frequency dependence is commonly observed for various polymeric solutions at high frequencies. The limits of $\beta = 0$ and 1 correspond to the purely elastic and purely viscous cases, respectively. Following the previous results, we argue that the time dependencies of MSD which has been expressed as $\phi_0 \sim t^\alpha$ in the pure viscous case will be modified to $\phi_0 \sim t^{\alpha\beta}$ both for the static and the active wall cases. Hence the asymptotic exponent of the MSD is generally smaller than that for a purely viscous fluid.

Appendix 6.A   Solutions of hydrodynamic equations

The incompressibility condition Eq. (6.5) and the Stokes equation (6.6) can be formally solved for the fluid velocity $\boldsymbol{v}$ in terms of the force $\boldsymbol{f}$ acting on the fluid [6.53]:

$$v_x(\boldsymbol{q}, z) = \int_{-\infty}^{\infty} dz' \frac{e^{-q|z-z'|}}{4\eta q}[(1 - q|z - z'|)f_x(\boldsymbol{q}, z') + iq(z' - z)f_z(\boldsymbol{q}, z')], \quad (6.65)$$

$$v_y(\boldsymbol{q}, z) = \int_{-\infty}^{\infty} dz' \frac{e^{-q|z-z'|}}{4\eta q}2f_y(\boldsymbol{q}, z'), \quad (6.66)$$

$$v_z(\boldsymbol{q}, z) = \int_{-\infty}^{\infty} dz' \frac{e^{-q|z-z'|}}{4\eta q}[(1 + q|z - z'|)f_z(\boldsymbol{q}, z') + iq(z' - z)f_x(\boldsymbol{q}, z')], \quad (6.67)$$

with $q = |\boldsymbol{q}|$. Notice that v_y in Eq. (6.66) is not coupled to the other components and hence can be neglected.

For the fluid in the region $0 \le z \le \bar{\ell}$, the forces are acting both at $z = 0$ and

$z = \bar{\ell}$ so that f_x and f_z can be written as

$$f_x(\boldsymbol{q}, z) = f_x(\boldsymbol{q}, 0)\delta(z) + f_x(\boldsymbol{q}, \bar{\ell})\delta(z - \bar{\ell}), \tag{6.68}$$

$$f_z(\boldsymbol{q}, z) = f_z(\boldsymbol{q}, 0)\delta(z) + f_z(\boldsymbol{q}, \bar{\ell})\delta(z - \bar{\ell}). \tag{6.69}$$

Substituting Eqs. (6.68) and (6.69) into Eq. (6.67), we obtain Eq. (6.10) where the the coefficients A and B are given by

$$A = \frac{e^{-q\bar{\ell}}}{2\eta q} \left[iq\bar{\ell} f_x(\boldsymbol{q}, \bar{\ell}) + (1 + q\bar{\ell}) f_z(\boldsymbol{q}, \bar{\ell}) \right], \tag{6.70}$$

$$B = \frac{e^{-q\bar{\ell}}}{2\eta q} \left[-i(1 - q\bar{\ell}) f_x(\boldsymbol{q}, \bar{\ell}) + q\bar{\ell} f_z(\boldsymbol{q}, \bar{\ell}) \right]. \tag{6.71}$$

For the fluid in the region $\bar{\ell} \le z$, the forces are acting only at $z = \bar{\ell}$ so that f_x and f_z can be written as

$$f_x(\boldsymbol{q}, z) = f_x(\boldsymbol{q}, \bar{\ell})\delta(z - \bar{\ell}), \tag{6.72}$$

$$f_z(\boldsymbol{q}, z) = f_z(\boldsymbol{q}, \bar{\ell})\delta(z - \bar{\ell}). \tag{6.73}$$

Substituting Eqs. (6.72) and (6.73) into Eq. (6.67), we obtain Eq. (6.11) where the the coefficients C and D are given by

$$C = \frac{f_z(\boldsymbol{q}, \bar{\ell})}{4\eta q}, \tag{6.74}$$

$$D = \frac{f_z(\boldsymbol{q}, \bar{\ell}) - if_x(\boldsymbol{q}, \bar{\ell})}{4\eta q}. \tag{6.75}$$

Using these four coefficients A, B, C and D, the x-component of the velocity $v_x^{\pm}(\boldsymbol{q}, z, t)$ and the pressure $p^{\pm}(\boldsymbol{q}, z, t)$ are obtained as follows:

$$v_x^{-}(\boldsymbol{q}, z, t) = - iAqz \sinh(qz) + iB[\sinh(qz) + qz\cosh(qz)]$$
$$+ (1 - qz)V_{x0}(\boldsymbol{q}, t)e^{-qz} - iqzV_{z0}(\boldsymbol{q}, t)e^{-qz}, \tag{6.76}$$

115

$$v_x^+(\boldsymbol{q}, z, t) = -ie^{-q(z-\bar{\ell})}(C - D - Dq\bar{\ell} + Dqz), \qquad (6.77)$$

$$
\begin{aligned}
p^-(\boldsymbol{q}, z, t) = &-2\eta q[A\cosh(qz) - B\sinh(qz)] \\
&+ 2\eta q[V_{z0}(\boldsymbol{q}, t) - iV_{x0}(\boldsymbol{q}, t)]e^{-qz}, \qquad (6.78)
\end{aligned}
$$

$$p^+(\boldsymbol{q}, z, t) = 2\eta Dqe^{-q(z-\bar{\ell})}. \qquad (6.79)$$

The four unknown coefficients are determined by the boundary conditions (6.12), (6.13), (6.14) and (6.15) at $z = \bar{\ell}$.

Bibliography

[6.1] Edited by R. Lipowsky and E. Sackmann, *Structure and Dynamics of Membranes – from Cells to Vesicles* (Elsevier, Amsterdam, 1995).

[6.2] S. T. Milner and S. A. Safran, *Phys. Rev. A* **36**, 4371 (1987).

[6.3] S. Komura and K. Seki, *Physica A* **192**, 27 (1993).

[6.4] K. Seki and S. Komura, *Physica A* **219**, 253 (1995).

[6.5] S. Komura, *Vesicles*, edited by M. Rosoff (Marcel Dekker, New York, 1996) p.198.

[6.6] G. Popescu, T. Ikeda, K. Goda, C. A. Best, M. Laposata, S. Manley, R. R. Dasari, K. Badizadegan, and M. S. Feld, *Phys. Rev. Lett.* **97**, 218101 (2006).

[6.7] M. D. El Alaoui Faris, D. Lacoste, J. Pécréaux, J.-F. Joanny, J. Prost, and P. Bassereau, *Phys. Rev. Lett.* **102**, 038102 (2009).

[6.8] D. Lacoste and P. Bassereau, *Liposomes, Lipid Bilayers and Model Membranes: From Basic Research to Application*, edited by G. Pabst, N. Kučerka, M.-P. Nieh, and J. Katsaras (CRC Press, Abington, 2014) p.271.

[6.9] F. Brochard and J.-F. Lennon, *J. Phys. (Paris)* **36**, 1035 (1975).

[6.10] S. Levin and R. Korenstein, *Biophys. J.* **60**, 733 (1991).

[6.11] S. Tuvia, S. Levin, A. Bitler, and R. Korenstein, *J. Cell Biol.* **141**, 1551 (1998).

[6.12] B. Alberts, A. Johnson, P. Walter, J. Lewis, and M. Raff, *Molecular Biology of the Cell* (Garland Science, New York, 2008).

[6.13] T. Betz, M. Lenz, J.-F. Joanny, and C. Sykes, *Proc. Natl. Acad. Sci.* **106**, 15320 (2009).

[6.14] Y. Park, C. A. Best, T. Auth, N. S. Gov, S. A. Safran, G. Popescug, S. Suresh, and M. S. Felda, *Proc. Natl. Acad. Sci.* **107**, 1289 (2010).

[6.15] D. Boss, A. Hoffmann, B. Rappaz, C. Depeursinge, P. J. Magistretti, D. V. de Ville, and P. Marquet, *PLoS ONE* **7**, e40667 (2012).

[6.16] N. Gov, A. G. Zilman, and S. Safran, *Phys. Rev. Lett.* **90**, 228101 (2003).

[6.17] N. Gov, A. G. Zilman, and S. Safran, *Phys. Rev. E* **70**, 011104 (2004).

[6.18] S. Tuvia, A. Almagor, A. Bitler, S. Levin, R. Korenstein, and S. Yedgar, *Proc. Natl. Acad. Sci.* **94**, 5045 (1997).

[6.19] N. S. Gov and S. A. Safran, *Biophys. J.* **88**, 1859 (2005).

[6.20] N. S. Gov, *Phys. Rev. E* **75**, 011921 (2007).

[6.21] Y. Kaizuka and J. T. Groves, *Biophys. J.* **86**, 905 (2004).

[6.22] Y. Kaizuka and J. T. Groves, *Phys. Rev. Lett.* **96**, 118101 (2006).

117

[6.23] O. Diat, D. Roux, and F. Nallet, *J. Phys. II France* **3**, 1427 (1993).

[6.24] C.-Y. D. Lu, P. Chen, Y. Ishii, S. Komura, and T. Kato, *Eur. Phys. J. E* **25**, 91 (2008).

[6.25] L. Kramer, J. Chem. Phys. **55**, 2097 (1971).

[6.26] U. Seifert, *Phys. Rev. E* **49**, 3124 (1994).

[6.27] S. A. Safran, *Statistical Thermodynamics of Surfaces, Interfaces, and Membranes* (New York, Addison-Wesley, 1994).

[6.28] R. Lipowsky and S. Leibler, *Phys. Rev. Lett.* **56**, 2541 (1986).

[6.29] R. Lipowsky and B. Zielinska, *Phys. Rev. Lett.* **62**, 1572 (1989).

[6.30] R. Kubo, M. Toda, and N. Hashitsume, *Statistical Physics II* (Springer-Verlag, New York, 1991).

[6.31] L. D. Landau, E. M. Lifshitz, and L. P. Pitaevskii, *Statistical Physics* (Pergamon Press, Offord, 1980).

[6.32] Y. Marathe and S. Ramaswamy, *Europhys. Lett.* **8**, 581 (1989).

[6.33] A. G. Zilman and R. Granek, *Phys. Rev. Lett.* **77**, 4788 (1996).

[6.34] A. G. Zilman and R. Granek, *Chem. Phys.* **284**, 195 (2002).

[6.35] Wolfram Research Inc., Mathematica 10 (Wolfram Research, Champaign, 1988).

[6.36] S. Komura and D. Andelman, *Eur. Phys. J. E* **3**, 259 (2000).

[6.37] J. Prost and R. Bruinsma, *Europhys. Lett.* **33**, 321 (1996).

[6.38] J. Prost, J.-B. Manneville, and R. Bruinsma, *Eur. Phys. J. B* **1**, 465 (1998).

[6.39] S. Ramaswamy, J. Toner, and J. Prost, *Phys. Rev. Lett.* **84**, 3494 (2000).

[6.40] R. Granek and S. Pierrat, *Phys. Rev. Lett.* **83**, 872 (1999).

[6.41] H.-Y. Chen, *Phys. Rev. Lett.* **92**, 168101 (2004).

[6.42] N. Gov, *Phys. Rev. Lett.* **93**, 268104 (2004).

[6.43] D. Lacoste and A. W. C. Lau, *Europhys. Lett.* **70**, 418 (2005).

[6.44] J.-B. Manneville, P. Bassereau, D. Lévy, and J. Prost, *Phys. Rev. Lett.* **82**, 4356 (1999).

[6.45] J.-B. Manneville, P. Bassereau, S. Ramaswamy, and J. Prost, *Phys. Rev. E* **64**, 021908 (2001).

[6.46] P. Girard, J. Prost, and P. Bassereau, *Phys. Rev. Lett.* **94**, 088102 (2005).

[6.47] A. Maitra, P. Srivastava, M. Rao, and S. Ramaswamy, *Phys. Rev. Lett.* **112**, 258101 (2014).

[6.48] A. Zilker, H. Engelhardt, and E. Sackmann, *J. Phys. (Paris)* **48**, 2139 (1987).

[6.49] R. Granek, *Soft Matter* **7**, 5281 (2011).

[6.50] S. Komura, K. Yasuda, and R. Okamoto, *J. Phys.: Condens. Matter* **27**, 432001 (2015).

[6.51] S. Komura, S. Ramachandran, and K. Seki, *EPL* **97**, 68007 (2012).

[6.52] S. Komura, S. Ramachandran, and K. Seki, *Materials* **5**, 1923 (2012).
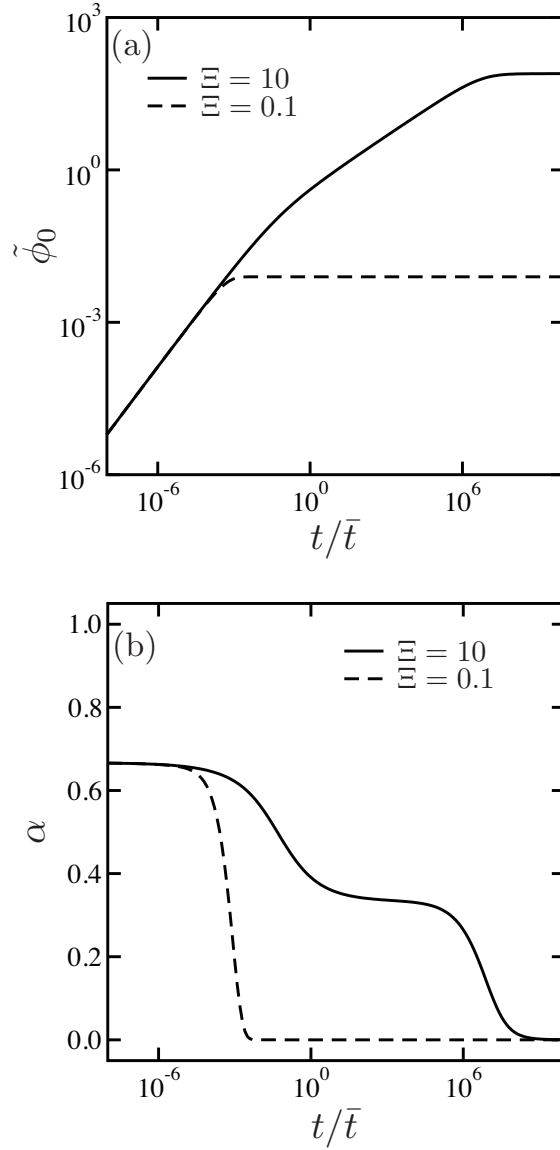
[6.53] U. Seifert, *Adv. Phys.* **46**, 13 (1997).

Figure 6.4: (a) Dimensionless mean squared displacement (MSD) of a tagged membrane segment $\tilde{\phi}_0 \equiv (\pi\kappa/k_{\mathrm{B}}T\bar{\ell}^2)\phi_0$ in the presence of a static wall (see Eq. (6.33)) as a function of dimensionless time $t/\bar{t}$ where $\bar{t} = 4\eta\bar{\ell}^3/\kappa$. The solid and dashed lines represent $\Xi = \xi/\bar{\ell} = 10$ and 0.1, respectively. (b) Effective exponent α of the MSDs in (a) as defined in Eq. (6.34).
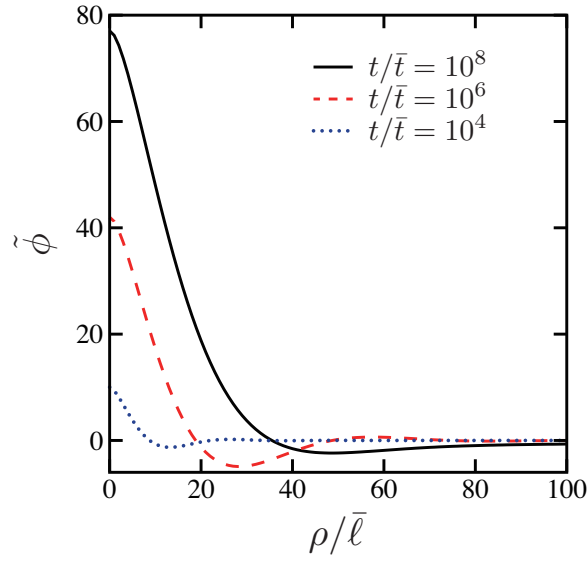
120

Figure 6.5: Dimensionless dynamical correlator $\tilde{\phi} \equiv (\pi\kappa/k_{\mathrm{B}}T\bar{\ell}^2)\phi$ in the presence of a static wall (see Eq. (7.16)) as a function of dimensionless distance $\rho/\bar{\ell}$ for $t/\bar{t} = 10^8$ (solid black), 10^6 (dashed red), 10^4 (dotted blue) when $\Xi = \xi/\bar{\ell} = 10$. Here the characteristic time is $\bar{t} = 4\eta\bar{\ell}^3/\kappa$.
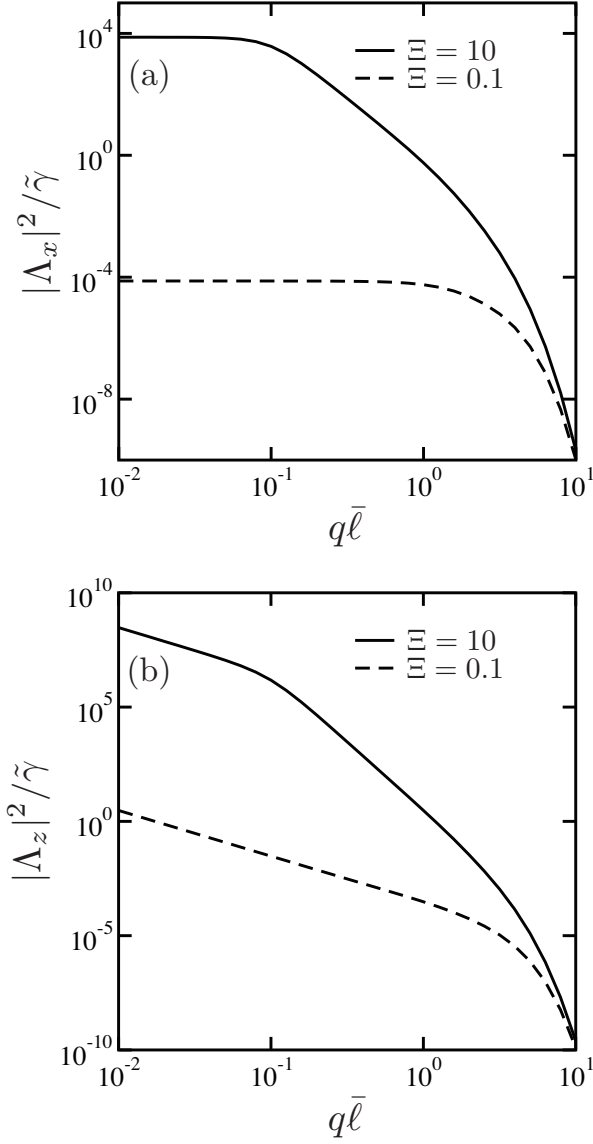
Figure 6.6: Plots of (a) $|\Lambda_x|^2/\tilde{\gamma}$ (see Eq. (6.20)) and (b) $|\Lambda_z|^2/\tilde{\gamma}$ (see Eq. (6.21)) as a function of dimensionless wave number $q\bar{\ell}$. Here $\tilde{\gamma} \equiv \gamma\bar{t}$ (see Eq. (6.18)) with $\bar{t} = 4\eta\bar{\ell}^3/\kappa$ is the dimensionless decay rate. The solid and dashed lines represent $\Xi = \xi/\bar{\ell} = 10$ and 0.1, respectively.
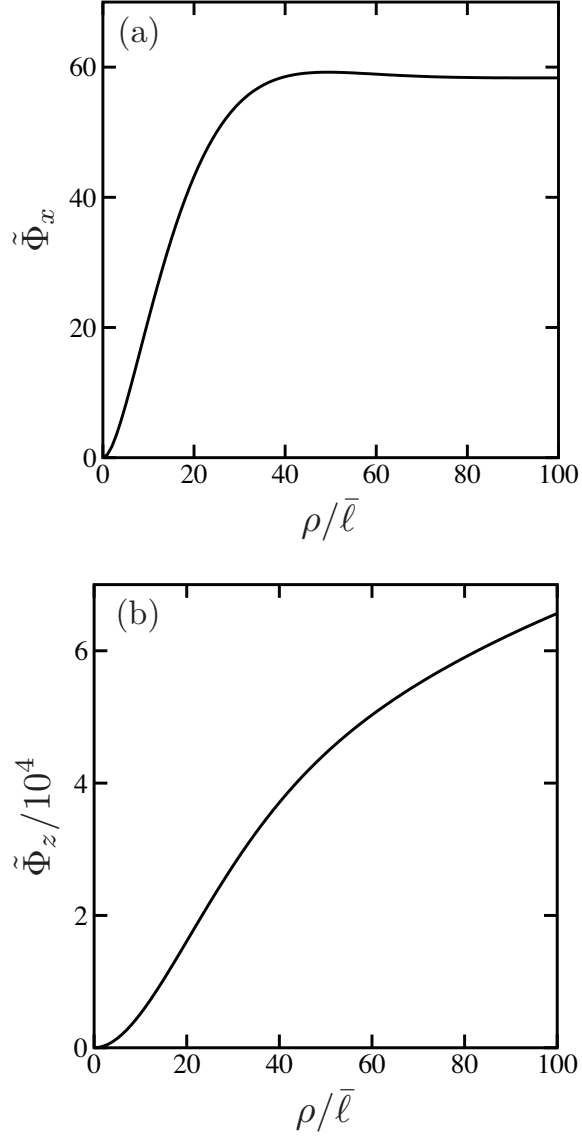
Figure 6.7: Dimensionless static correlators (a) $\tilde{\Phi}_x \equiv (\pi\kappa/4\eta\bar{\ell}S_x)\Phi_x$ and (a) $\tilde{\Phi}_z \equiv (\pi\kappa/4\eta\bar{\ell}S_z)\Phi_z$ (divided by 10^4) in the presence of an active wall (see Eq. (6.45)) as a function of dimensionless distance $\rho/\bar{\ell}$ when $\Xi = \xi/\bar{\ell} = 10$.
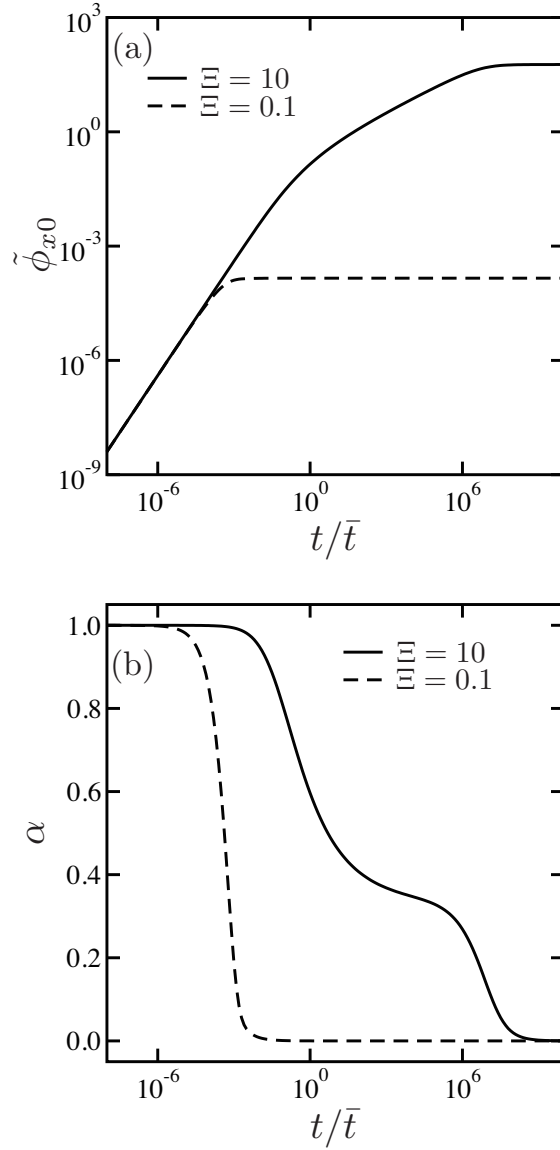
Figure 6.8: (a) Dimensionless mean squared displacement (MSD) of a tagged membrane segment $\tilde{\phi}_{x0} \equiv (\pi\kappa/4\eta\bar{\ell}S_x)\phi_{x0}$ in the presence of an active wall (see Eq. (6.47)) as a function of dimensionless time $t/\bar{t}$ where $\bar{t} = 4\eta\bar{\ell}^3/\kappa$. The solid and dashed lines represent $\Xi = \xi/\bar{\ell} = 10$ and 0.1, respectively. (b) Effective exponent α of the MSDs in (a) as defined in Eq. (6.34).
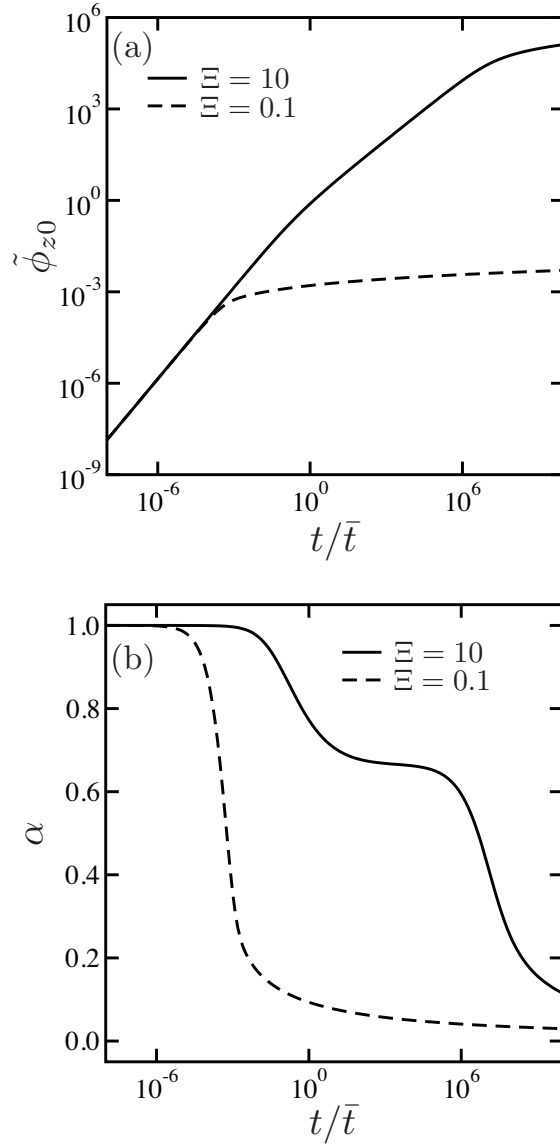
Figure 6.9: (a) Dimensionless mean squared displacement (MSD) of a tagged membrane segment $\tilde{\phi}_{z0} \equiv (\pi\kappa/4\eta\bar{\ell}S_z)\phi_{z0}$ in the presence of an active wall (see Eq. (6.47)) as a function of dimensionless time $t/\bar{t}$ where $\bar{t} = 4\eta\bar{\ell}^3/\kappa$. The solid and dashed lines represent $\Xi = \xi/\bar{\ell} = 10$ and 0.1, respectively. (b) Effective exponent α of the MSDs in (a) as defined in Eq. (6.34).
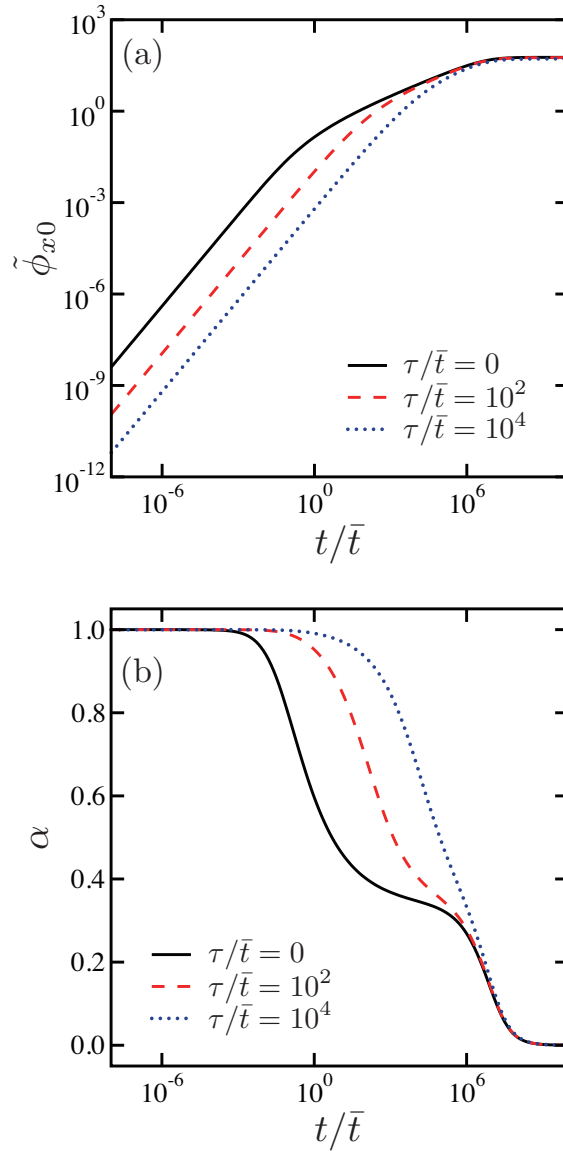
Figure 6.10: (a) Dimensionless mean squared displacement (MSD) of a tagged membrane segment $\tilde{\phi}_{x0} \equiv (\pi\kappa/4\eta\bar{\ell}S_x)\phi_{x0}$ in the presence of an active wall with an intrinsic time scale (see Eq. (6.59)) as a function of dimensionless time $t/\bar{t}$ where $\bar{t} = 4\eta\bar{\ell}^3/\kappa$. Different colors correspond to $\tau/\bar{t} = 0$ (solid black), 10^2 (dashed red), 10^4 (dotted blue) and we set $\Xi = 10$. (b) Effective exponent α of the MSDs in (a) as defined in Eq. (6.34).
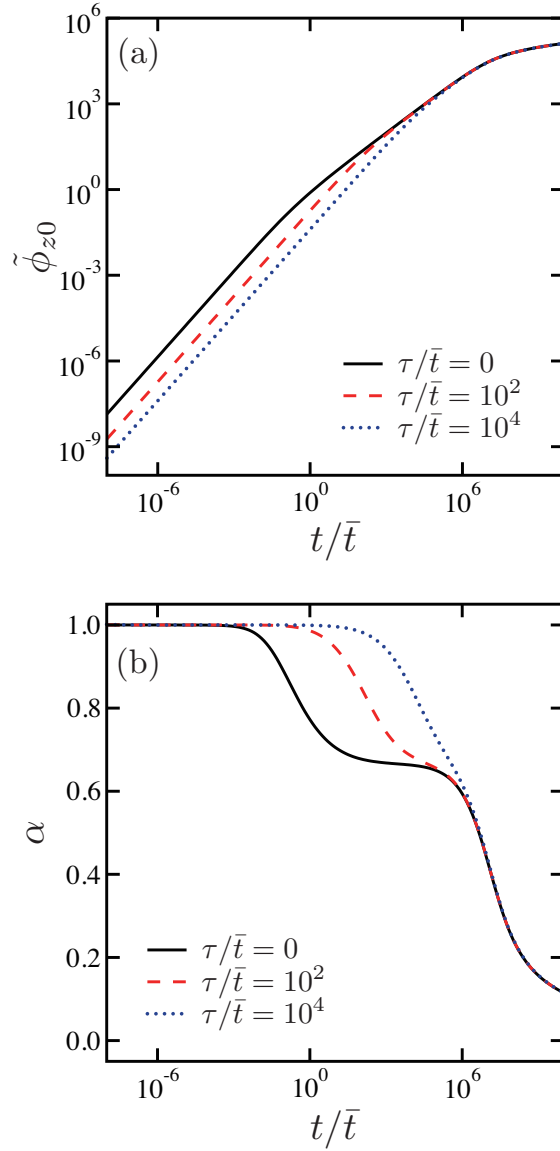
126

Figure 6.11: (a) Dimensionless mean squared displacement (MSD) of a tagged membrane segment $\tilde{\phi}_{z0} \equiv (\pi\kappa/4\eta\bar{\ell}S_z)\phi_{z0}$ in the presence of an active wall with an intrinsic time scale (see Eq. (6.60)) as a function of dimensionless time $t/\bar{t}$ where $\bar{t} = 4\eta\bar{\ell}^3/\kappa$. Different colors correspond to $\tau/\bar{t} = 0$ (solid black), 10^2 (dashed red), 10^4 (dotted blue) and we set $\Xi = 10$. (b) Effective exponent α of the MSDs in (a) as defined in Eq. (6.34).

Chapter 7

Dynamics of two-component membranes surrounded by viscoelastic media

We discuss the dynamics of two-component fluid membranes which are surrounded by viscoelastic media. We assume that membrane-embedded proteins can diffuse laterally and induce a local membrane curvature. The mean squared displacement of a tagged membrane segment is obtained as a generalized Einstein relation. When the elasticity of the surrounding media obeys a power-law behavior in frequency, an anomalous diffusion of the membrane segment is predicted. We also consider the situation where the proteins generate active non-equilibrium forces. The generalized Einstein relation is further modified by an effective temperature that depends on the force dipole energy. The obtained generalized Einstein relations are useful for membrane microrheology experiments.

7.1   Introduction

Biomembranes are thin two-dimensional fluids which separate inner and outer environments of organelles in cells. The fluidity of biomembranes is guaranteed

mainly due to the lipid molecules which are in the liquid crystalline state at physiological temperatures. Proteins and other molecules embedded in biomembranes undergo lateral diffusion which plays important roles for biological functions [7.1]. It should be noted, however, that biomembranes are not isolated 2D systems, but are coupled to the surrounding polar solvent such as water.

Moreover, the solvent surrounding biomembranes is viscoelastic rather than purely viscous. This is a common situation in all eukaryotic cells whose cytoplasm is a soup of proteins and organelles, including a thick sub-membrane layer of actin-meshwork forming a part of the cell cytoskeleton [7.1]. The extra-cellular fluid can also be viscoelastic because it is filled with extracellular matrix or hyaluronic acid gel. Recently, Granek discussed the dynamics of an undulating bilayer membrane surrounded by viscoelastic media [7.2]. He calculated the frequency-dependent out-of-plane (transverse) mean squared displacement (MSD) of a membrane segment and the linear response to external forces.

In this work, we discuss the dynamics and responses of two-component membranes containing proteins such as ion channels, ion pumps, or photo-active proteins like bacteriorhodopsin. These proteins can diffuse laterally within the membranes. We use a model that incorporates curvature-concentration coupling as well as hydrodynamics interactions. We calculate the MSD of a tagged membrane segment by taking into account the viscoelasticity of the surrounding media as well as the diffusivity of the proteins. Our aim is to derive a generalized Einstein relation for the membrane-protein system, which is useful for membrane microrheology experiments.

Furthermore, the state of the membrane proteins can be either passive or active [7.3]. In the latter case, the proteins consume the chemical energy and drive the membrane out of equilibrium. It was experimentally shown that active forces due to ion pumps enhance membrane fluctuations [7.4–7.7]. There exist two important theoretical models for active membranes; (i) Prost-Bruinsma (PB) model which takes into account the stochastic nature of the pumps [7.8, 7.9], and (ii) Ramaswamy-Toner-Prost (RTP) model which considers the coupling between the

129

protein density and membrane curvature [7.10]. In this paper, we use the simplified RTP model proposed by Sankararaman *et al.* [7.11], and investigate the effects of the surrounding viscoelastic media on the membrane dynamics. As discussed in Ref. [7.11], one of our important assumptions is that the membrane is impermeable to the solvent both for the active and passive states.

In the next Section, we describe the free energy of the membrane-protein system. In Sec. 7.3, we present dynamic equations which take into account the viscoelasticity of the surrounding media. On the basis of the model, we calculate the membrane MSD and obtain a generalized Einstein relation in Sec. 7.4. The case of active membranes will be discussed in Sec. 7.5. Finally, the obtained MSD is related to the response function in the last Section.

7.2 Free energy

A two-component fluid membrane is regarded as an infinitesimally thin two-dimensional (2D) surface embedded in three-dimensional (3D) space. In order to describe the membrane deformation, we use the Monge gauge which is valid for nearly flat surfaces. Here the membrane surface is specified by its height above the flat xy-plane, $h(\boldsymbol{\rho}, t)$, where $\boldsymbol{\rho} = (x, y)$ and t is time. In this representation, the mean curvature of the surface is given by $H = (\nabla^2 h)/2$ to the lowest order.

Next we denote the number density of the embedded membrane proteins by $\psi(\boldsymbol{\rho}, t)$. As shown in Fig. 7.1, these intercalated protein molecules are assumed to induce a local curvature of the membrane surface [7.12, 7.13]. To leading order in gradients of h, the free energy functional of the membrane-protein system is given by [7.5, 7.10, 7.11]

$$F[h, \psi] = \frac{1}{2} \int d^2\rho \, [\kappa (\nabla^2 h)^2 - 2\kappa \bar{H} \psi (\nabla^2 h) + \chi_0^{-1} \psi^2], \qquad (7.1)$$

where κ is the bending rigidity, $\bar{H}\psi$ the protein density dependent spontaneous curvature, χ_0^{-1} the susceptibility which is assumed to be positive here. The above

model is limited to a liner level, and we do not address nonlinear effects [7.9]. For the clarity of our presentation, we only discuss tensionless membranes and do not include the surface tension energy proportional to $(\nabla h)^2$. Effects of surface tension have been discussed in detail in the literature [7.14].
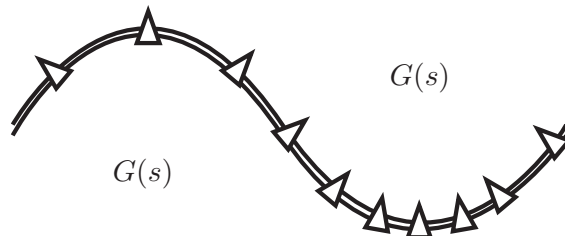

Figure 7.1: Asymmetric proteins (triangles) embedded in a fluid bilayer membrane. Accumulation of the proteins induces a local curvature of the membrane. The membrane is surrounded by a viscoelastic medium with a frequency-dependent modulus $G(s)$.

In the following, we introduce the 2D spatial Fourier transform of $h(\boldsymbol{\rho}, t)$ defined as

$$h(\boldsymbol{q}, t) = \int d^2\rho \, h(\boldsymbol{\rho}, t) e^{-i\boldsymbol{q}\cdot\boldsymbol{\rho}}, \tag{7.2}$$

and similarly for $\psi(\boldsymbol{q}, t)$. Using the free energy Eq. (7.1), one can easily show that the static (equal-time) correlation functions are given by

$$\langle h(\boldsymbol{q}, t) h(-\boldsymbol{q}, t) \rangle = \frac{k_{\mathrm{B}} T}{\kappa_{\mathrm{eff}} q^4}, \tag{7.3}$$

$$\langle h(\boldsymbol{q}, t) \psi(-\boldsymbol{q}, t) \rangle = -\frac{k_{\mathrm{B}} T \kappa \bar{H}}{\kappa_{\mathrm{eff}} \chi_0^{-1} q^2}, \tag{7.4}$$

$$\langle \psi(\boldsymbol{q}, t) \psi(-\boldsymbol{q}, t) \rangle = \frac{k_{\mathrm{B}} T \kappa}{\kappa_{\mathrm{eff}} \chi_0^{-1}}, \tag{7.5}$$

where k_{B} is the Boltzmann constant, T the temperature, and κ_{eff} the effective bending rigidity given by $\kappa_{\mathrm{eff}} = \kappa(1 - \kappa \bar{H}^2/\chi_0^{-1})$. Notice that $\kappa_{\mathrm{eff}} < \kappa$ irrespective of the sign of $\bar{H}$ because $\chi_0^{-1} > 0$. The stability of the free energy requires that the coupling parameter $\bar{H}$ needs to be small enough to satisfy the condition $\kappa \bar{H}^2/\chi_0^{-1} <$

1.

7.3 Dynamics

Next we discuss the dynamics of two-component membranes. We follow the argument in Ref. [7.11] and assume that the membrane is impermeable to the surrounding solvent. This is valid over the length scales of concern in the experiments [7.5]. When the membrane is surrounded by viscoelastic media, as considered by Granek [7.2], a generalized Langevin equation for the motion of the displacement filed $h(\boldsymbol{\rho}, t)$ is given by

$$\frac{\partial h(\boldsymbol{\rho}, t)}{\partial t} = - \int_0^t dt' \int d^2\rho' \, \Lambda(\boldsymbol{\rho} - \boldsymbol{\rho}', t - t') \frac{\delta F}{\delta h(\boldsymbol{\rho}', t')} + \xi(\boldsymbol{\rho}, t), \qquad (7.6)$$

where $\Lambda(\rho, t)$ is the retarded Oseen mobility. Its Laplace transform is given by

$$\Lambda(\boldsymbol{\rho}, s) = \int_0^\infty dt \, \Lambda(\boldsymbol{\rho}, t) e^{-st} = \frac{1}{8\pi\eta(s)\rho}, \qquad (7.7)$$

where $\rho = |\boldsymbol{\rho}|$ and $\eta(s)$ is the frequency-dependent viscosity of the surrounding viscoelastic media (s being the frequency in the Laplace domain). The 2D Fourier transform of Eq. (7.7) is

$$\Lambda(\boldsymbol{q}, s) = \frac{1}{4\eta(s)q}, \qquad (7.8)$$

with $q = |\boldsymbol{q}|$. The average of the thermal noise in Eq. (7.6) is $\langle \xi(\boldsymbol{\rho}, t) \rangle = 0$, whereas its correlation obeys the following fluctuation-dissipation theorem (FDT) [7.15, 7.16]

$$\langle \xi(\boldsymbol{\rho}, t)\xi(\boldsymbol{\rho}', t') \rangle = 2k_{\mathrm{B}}T\Lambda(\boldsymbol{\rho} - \boldsymbol{\rho}', t - t'). \qquad (7.9)$$

Since the proteins diffuse freely on the membrane surface, the conserved quantity $\psi(\boldsymbol{\rho}, t)$ should obey the continuity equation of the form

$$\frac{\partial \psi(\boldsymbol{\rho}, t)}{\partial t} = L\nabla^2 \frac{\delta F}{\delta \psi(\boldsymbol{\rho}, t)} + \nabla \cdot \boldsymbol{\zeta}(\boldsymbol{\rho}, t), \qquad (7.10)$$

132

where L is the transport coefficient which is assume to be constant. In this diffusion, however, the hydrodynamic interaction is neglected [7.17]. The last term is a conserving Gaussian noise with $\langle \boldsymbol{\zeta}(\boldsymbol{\rho}, t) \rangle = 0$ and its correlations are given by

$$\langle \zeta_i(\boldsymbol{\rho}, t) \zeta_j(\boldsymbol{\rho}', t') \rangle = 2k_{\mathrm{B}} T L \delta_{ij} \delta(\boldsymbol{\rho} - \boldsymbol{\rho}') \delta(t - t'). \tag{7.11}$$

Equations (7.6) and (7.11) are the set of equations to be investigated.

The above equations can be conveniently solved by using the Laplace transform of $h(\boldsymbol{q}, t)$ and $\psi(\boldsymbol{q}, t)$ (see Eq. (7.7)). Then Eqs. (7.6) and (7.11) can be written in the matrix form as

$$\begin{pmatrix} \Lambda(\boldsymbol{q}, s)\kappa q^4 + s & \Lambda(\boldsymbol{q}, s)\kappa \bar{H} q^2 \\ L\kappa \bar{H} q^4 & Dq^2 + s \end{pmatrix} \begin{pmatrix} h(\boldsymbol{q}, s) \\ \psi(\boldsymbol{q}, s) \end{pmatrix} = \begin{pmatrix} \xi(\boldsymbol{q}, s) + h_0 \\ i\boldsymbol{q} \cdot \boldsymbol{\zeta}(\boldsymbol{q}, s) + \psi_0 \end{pmatrix}, \tag{7.12}$$

where $D = L\chi_0^{-1}$, $h_0 = h(\boldsymbol{q}, t = 0)$ and $\psi_0 = \psi(\boldsymbol{q}, t = 0)$. After some calculations, we obtain the solution as

$$h(\boldsymbol{q}, s) =$$
$$\frac{(Dq^2 + s)h_0 - \Lambda(\boldsymbol{q}, s)\kappa \bar{H} q^2 \psi_0 + (Dq^2 + s)\xi(\boldsymbol{q}, s) - i\Lambda(\boldsymbol{q}, s)\kappa \bar{H} q^2 \boldsymbol{q} \cdot \boldsymbol{\zeta}(\boldsymbol{q}, s)}{(\Lambda(\boldsymbol{q}, s)\kappa q^4 + s)(Dq^2 + s) - \Lambda(\boldsymbol{q}, s)L\kappa^2 \bar{H}^2 q^6},$$
$$\tag{7.13}$$

$$\psi(\boldsymbol{q}, s) =$$
$$\frac{-L\kappa \bar{H} q^4 h_0 + (\Lambda(\boldsymbol{q}, s)\kappa q^4 + s)\psi_0 - L\kappa \bar{H} q^4 \xi(\boldsymbol{q}, s) + i(\Lambda(\boldsymbol{q}, s)\kappa q^4 + s)\boldsymbol{q} \cdot \boldsymbol{\zeta}(\boldsymbol{q}, s)}{(\Lambda(\boldsymbol{q}, s)\kappa q^4 + s)(Dq^2 + s) - \Lambda(\boldsymbol{q}, s)L\kappa^2 \bar{H}^2 q^6}.$$
$$\tag{7.14}$$

We use Eq. (7.13) to calculate the membrane MSD in the next section.

7.4   Membrane mean squared displacement

The important quantity from the experimental point of view is the MSD of a tagged membrane segment defined as

$$\phi(t) = \langle [h(\boldsymbol{\rho},t) - h(\boldsymbol{\rho},0)]^2 \rangle$$
$$= 2 \int \frac{d^2 q}{(2\pi)^2} \left[\langle h(\boldsymbol{q},t)h(-\boldsymbol{q},t) \rangle - \langle h(\boldsymbol{q},t)h(-\boldsymbol{q},0) \rangle \right]. \qquad (7.15)$$

The first term in the above integrand is the equal-time correlation function given by Eq. (7.3). The Laplace transform of the time correlation function $\langle h(\boldsymbol{q},t)h(-\boldsymbol{q},0) \rangle$ can be obtained from Eq. (7.13) as follows

$$\langle h(\boldsymbol{q},s)h(-\boldsymbol{q},t=0) \rangle = \frac{k_{\mathrm{B}}T}{\kappa_{\mathrm{eff}} q^4} \frac{(Dq^2 + s) + \Lambda(\boldsymbol{q},s)\kappa^2 \bar{H}^2 q^4 / \chi_0^{-1}}{(\Lambda(\boldsymbol{q},s)\kappa q^4 + s)(Dq^2 + s) - \Lambda(\boldsymbol{q},s)L\kappa^2 \bar{H}^2 q^6}. \qquad (7.16)$$

Here we have used Eqs. (7.3) and (7.4) for the equal-time correlation functions. Another important assumption to derive the above correlation function is that the stochastic thermal noise ξ and $\boldsymbol{\zeta}$ are uncorrelated with the initial condition of the height $h(\boldsymbol{q},t=0) = h_0$, which is somewhat non-trivial [7.15]. Using Eqs. (7.3) and (7.16) in Eq. (7.15), the Laplace transformed MSD of a membrane segment can be conveniently written as [7.2]

$$\phi(s) = 2 \int \frac{d^2 q}{(2\pi)^2} \frac{k_{\mathrm{B}}T}{\kappa_{\mathrm{eff}} q^4} \left(\frac{1}{s} - \frac{(Dq^2 + s) + \Lambda(\boldsymbol{q},s)\kappa^2 \bar{H}^2 q^4 / \chi_0^{-1}}{(\Lambda(\boldsymbol{q},s)\kappa q^4 + s)(Dq^2 + s) - \Lambda(\boldsymbol{q},s)L\kappa^2 \bar{H}^2 q^6} \right). \qquad (7.17)$$

Hereafter we use the general viscoelasticity relation for the frequency dependent modulus $G(s) = s\eta(s)$. Using Eq. (7.8) for $\Lambda(\boldsymbol{q},s)$, one can rearrange the integrand in Eq. (7.17) as

$$\phi(s) = \frac{1}{\pi} \frac{k_{\mathrm{B}}T}{4sG(s)} \int_0^\infty dq \left(\frac{\kappa q^3}{4G(s)} + 1 - \frac{D\kappa^2 \bar{H}^2}{4\chi_0^{-1}G(s)} \frac{q^5}{Dq^2 + s} \right)^{-1}. \qquad (7.18)$$

134

Although it is impossible to perform the above integral analytically, Eq. (7.18) can be regarded as a generalized Einstein relation for a segment of two-component membranes.

We recall here that the coupling parameter $\bar{H}$ should be small enough to satisfy the stability condition of the free energy Eq. (7.1). When $\kappa \bar{H}^2 / \chi_0^{-1} \ll 1$, Eq. (7.18) can be expanded in powers of $\bar{H}$, and the approximated form can be obtained as

$$
\begin{aligned}
\phi(s) \approx &\frac{1}{\pi} \frac{k_{\mathrm{B}} T}{4 s G(s)} \left[\int_0^\infty dq \left(\frac{\kappa q^3}{4 G(s)} + 1 \right)^{-1} \right. \\
&\left. + \frac{D \kappa^2 \bar{H}^2}{4 \chi_0^{-1} G(s)} \int_0^\infty dq \left(\frac{\kappa q^3}{4 G(s)} + 1 \right)^{-2} \frac{q^5}{D q^2 + s} \right].
\end{aligned}
\tag{7.19}
$$

Here both of the integrals can be performed analytically. Especially, by defining dimensionless quantities $\hat{q}^3 = \kappa q^3 / 4 G(s)$ and $\hat{s} = (s/D)(\kappa / 4 G(s))^{2/3}$, the second integral can be written in the form

$$
\int_0^\infty dq \left(\frac{\kappa q^3}{4 G(s)} + 1 \right)^{-2} \frac{q^5}{D q^2 + s} = \left(\frac{\kappa}{4 G(s)} \right)^{-4/3} \frac{I(\hat{s})}{D},
\tag{7.20}
$$

where

$$
\begin{aligned}
I(\hat{s}) = &\int_0^\infty d\hat{q} \, \frac{\hat{q}^5}{(\hat{q}^3 + 1)^2 (\hat{q}^2 + \hat{s})} \\
= &\frac{1}{(1 + \hat{s}^3)^2} \left[\frac{2\pi}{3^{5/2}} - \frac{2\pi \hat{s}}{3^{5/2}} - \left(\frac{1}{3} + \frac{\ln \hat{s}}{2} \right) \hat{s}^2 + \frac{14 \pi \hat{s}^3}{3^{5/2}} \right. \\
&\left. - \pi \hat{s}^{7/2} + \frac{10 \pi \hat{s}^4}{3^{5/2}} - \left(\frac{1}{3} - \frac{\ln \hat{s}}{2} \right) \hat{s}^5 \right].
\end{aligned}
\tag{7.21}
$$

The behavior of $I(\hat{s})$ is illustrated in Fig. 7.2. Performing the first integral in Eq. (7.19) and using Eq. (7.20), we obtain the Laplace transformed MSD as

$$
\phi(s) \approx \frac{2}{3^{3/2}} \frac{k_{\mathrm{B}} T}{D \kappa} \left(\frac{\kappa}{4 G(s)} \right)^{4/3} \frac{1}{\hat{s}} \left[1 + \frac{3^{3/2}}{2\pi} \frac{\kappa \bar{H}^2 I(\hat{s})}{\chi_0^{-1}} \right],
\tag{7.22}
$$

which is the (approximated) generalized Einstein relation for membrane-protein
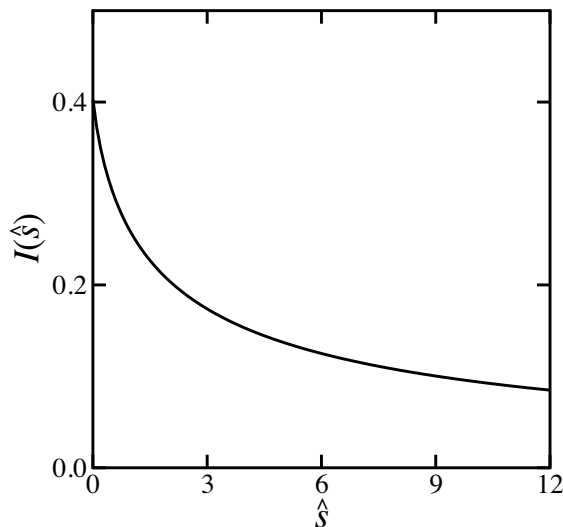
135

systems in the weak coupling limit.

Figure 7.2: The plot of the integral $I(\hat{s})$ defined in Eq. (7.21). Here the variable is $\hat{s} = (s/D)(\kappa/4G(s))^{2/3}$.

We denote the first and the second terms in Eq. (7.22) as $\phi_{\text{mem}}(s)$ and $\phi_{\text{diff}}(s)$, respectively, so that the total MSD is expressed as $\phi(s) = \phi_{\text{mem}}(s) + \phi_{\text{diff}}(s)$. The first term $\phi_{\text{mem}}(s)$ due to the membrane itself can be rewritten as

$$\phi_{\text{mem}}(s) = \frac{1}{3^{3/2}2^{1/3}} \frac{k_{\text{B}}T}{\kappa^{1/3}sG(s)^{2/3}}, \tag{7.23}$$

which coincides with the result by Granek [7.2], as it should. The second term $\phi_{\text{diff}}(s)$ is our new contribution due to the diffusion of proteins in the membrane;

$$\phi_{\text{diff}}(s) = \frac{1}{\pi} \frac{k_{\text{B}}T\bar{H}^2}{D\chi_0^{-1}} \left(\frac{\kappa}{4G(s)}\right)^{4/3} \frac{I(\hat{s})}{\hat{s}}, \tag{7.24}$$

where $\hat{s} = (s/D)(\kappa/4G(s))^{2/3}$ as before. We note here that ϕ_{diff} vanishes in the limit of $\bar{H} \to 0$.

As a working example, we consider the situation where both sides of the membrane are occupied by the same viscoelastic media with a frequency-dependent

136

modulus that obeys a power-law behavior [7.2, 7.18, 7.19];

$$G(s) = G_0 s^\alpha, \tag{7.25}$$

where $0 \leq \alpha \leq 1$. This behavior is commonly observed for various polymeric solutions at high frequencies. Examples are $\alpha = 1/2$ and $\alpha = 2/3$ for Rouse and Zimm dynamics, respectively [7.20], $\alpha = 3/4$ for semi-dilute solutions of semi-flexible polymers such as actin filaments [7.21]. The limits of $\alpha = 0$ and 1 correspond to the purely elastic and purely viscous cases, respectively.

For such power-law viscoelastic media, the membrane part of the time-dependent MSD can be readily obtained by performing the inverse Laplace transform [7.2]

$$\phi_{\mathrm{mem}}(t) = \frac{1}{3^{3/2}2^{1/3}\Gamma(1 + 2\alpha/3)} \frac{k_{\mathrm{B}}T}{\kappa^{1/3}G_0^{2/3}} t^{2\alpha/3}, \tag{7.26}$$

where $\Gamma(z)$ is the gamma function. In the purely elastic case of $\alpha = 0$, we have

$$\phi_{\mathrm{mem}}(t) = \frac{1}{3^{3/2}2^{1/3}} \frac{k_{\mathrm{B}}T}{\kappa^{1/3}G_0^{2/3}}, \tag{7.27}$$

which is independent of time. On the other hand, in the purely viscous case of $\alpha = 1$, Eq. (7.26) reduces to

$$\begin{aligned}
\phi_{\mathrm{mem}}(t) &= \frac{1}{3^{3/2}2^{1/3}\Gamma(5/3)} \frac{k_{\mathrm{B}}T}{\kappa^{1/3}G_0^{2/3}} t^{2/3} \\
&= 0.169 \frac{k_{\mathrm{B}}T}{\kappa^{1/3}\eta_0^{2/3}} t^{2/3},
\end{aligned} \tag{7.28}$$

where we have replaced G_0 with η_0 in the last expression. This result was previously obtained by Zilman and Granek for single component membranes [7.22, 7.23].

Next we discuss the time-dependence of the diffusive MSD $\phi_{\mathrm{diff}}(t)$ in the presence of power-law fluid media as given by Eq. (7.25). For this purpose, we first consider the asymptotic behaviors of $I(\hat{s})$ in Eq. (7.21). In the limit of $\hat{s} \to 0$, we

have

$$I(\hat{s}) \approx \frac{2\pi}{3^{5/2}} - \frac{2\pi}{3^{5/2}}\hat{s}, \tag{7.29}$$

whereas in the opposite limit of $\hat{s} \to \infty$, we get

$$I(\hat{s}) \approx -\left(\frac{1}{3} - \frac{\ln \hat{s}}{2}\right)\frac{1}{\hat{s}}. \tag{7.30}$$

In order to calculate $\phi_{\mathrm{diff}}(t)$, it is convenient to introduce a characteristic time scale defined by

$$\tau = \left(\frac{\kappa}{4G_0 D^{3/2}}\right)^{2/(3-2\alpha)}, \tag{7.31}$$

which is dependent on α. (Notice that the dimension of G_0 also depends on α.) In what follows, we shall use a dimensionless time defined by $\tilde{t} = t/\tau$. Using the above asymptotic expressions in Eq. (7.24) and performing the inverse Laplace transform, we obtain in the long time limit of $\tilde{t} \to \infty$ as

$$\begin{aligned}
\phi_{\mathrm{diff}}(\tilde{t}) &\approx \frac{1}{\pi}\frac{k_{\mathrm{B}}T\bar{H}^2}{D\chi_0^{-1}}\left(\frac{\kappa}{4G_0}\right)^{4/3}\tau^{4\alpha/3-1} \\
&\times \frac{2\pi}{3^{5/2}}\left[\frac{\tilde{t}^{2\alpha/3}}{\Gamma(1+2\alpha/3)} - \frac{\tilde{t}^{4\alpha/3-1}}{\Gamma[4\alpha/3]}\right].
\end{aligned} \tag{7.32}$$

Here the first term is proportional to $t^{2\alpha/3}$ as in Eq. (7.26), and can be also expressed as $(\kappa\bar{H}^2/3\chi_0^{-1})\phi_{\mathrm{mem}}(t)$, where $\phi_{\mathrm{mem}}(t)$ is given by Eq. (7.26). The same result would have been obtained simply by replacing κ in Eq. (7.26) by κ_{eff}. The second term, on the other hand, is proportional to $t^{4\alpha/3-1}$ showing a different exponent.

In the short time limit of $\tilde{t} \to 0$, we obtain

$$\begin{aligned}
\phi_{\mathrm{diff}}(\tilde{t}) &\approx \frac{1}{\pi}\frac{k_{\mathrm{B}}T\bar{H}^2}{D\chi_0^{-1}}\left(\frac{\kappa}{4G_0}\right)^{4/3}\tau^{4\alpha/3-1} \\
&\times \frac{\tilde{t}}{6}\left[(2\alpha-3)\ln\tilde{t} + (2\alpha-3)\gamma - 2\alpha + 1\right],
\end{aligned} \tag{7.33}$$

where $\gamma = 0.5772\cdots$ is Euler's constant. Since $\alpha \leq 1$, this MSD essentially grows

like $t \ln(1/t)$. Such a logarithmic correction leads to a time-dependent diffusivity. Equations (7.32) and (7.33) are the important results of this paper.

In Fig. 7.3, we plot the dimensionless MSD ϕ_{diff} due to the diffusion as a function of $\tilde{t} = t/\tau$ by performing the numerical inverse Laplace transform of Eq. (7.24) with full $I(\hat{s})$ when (a) $\alpha = 0$ and (b) $\alpha = 1/2$. We also compare it with the asymptotic expressions Eqs. (7.32) and (7.33) which are in good agreement with the numerical result. In both cases, we see a clear crossover from the almost liner behavior to the power-law behavior of $\tilde{t}^{2\alpha/3}$. In the case of purely elastic media of $\alpha = 0$, both the membrane and diffusive contributions to MSD become independent of time for large $\tilde{t}$ [7.2].

7.5 Active membranes

We now discuss the dynamic properties of a two-component membrane with active pumps which exert non-equilibrium forces on the surrounding fluid. As considered by Manneville *et al.* [7.5], each pump is represented as a force dipole, i.e., two force centers of opposite sign but equal magnitude separated by a distance w. This is justified because there should be no external force on the combined system of pump/membrane/solvent whose overall momentum is conserved. If the positive and negative force centers are located asymmetrically with respect to the midpoint of the membrane, the pumps exert nonzero active forces on the membrane and the surrounding media. When the force centers are located at $z = w_+$ and $z = -w_-$, as shown in Fig. 7.4, the active force is proportional to the protein density and can be written as [7.24]

$$\boldsymbol{F}_{\text{pump}} = f\psi(\boldsymbol{\rho}, t)[\delta(z - w_+) - \delta(z + w_-)]\hat{\boldsymbol{z}}, \qquad (7.34)$$

where f is the magnitude of the active force (taken to be constant) and $\hat{\boldsymbol{z}}$ is the unit vector along the z-direction.

Here we assume that pumps are always in the active state over the time scales

of interest, and the membrane feels the active forces only via the surrounding fluid [7.11]. The presence of the active force due to the pumps modifies Eq. (7.6) and can be conveniently expressed in the Fourier-Laplace domain. Corresponding to Eq. (7.12), we then have

$$
\begin{pmatrix} \Lambda(\boldsymbol{q},s)\kappa q^4 + s & \Lambda(\boldsymbol{q},s)[\kappa\bar{H}q^2 - f\Omega(\boldsymbol{q})] \\ L\kappa\bar{H}q^4 & Dq^2 + s \end{pmatrix} \begin{pmatrix} h(\boldsymbol{q},s) \\ \psi(\boldsymbol{q},s) \end{pmatrix} = \begin{pmatrix} \xi(\boldsymbol{q},s) + h_0 \\ i\boldsymbol{q}\cdot\boldsymbol{\zeta}(\boldsymbol{q},s) + \psi_0 \end{pmatrix},
$$
(7.35)

where

$$
\begin{aligned}
\Omega(\boldsymbol{q}) &= -(1 + qw_-)e^{-qw_-} + (1 + qw_+)e^{-qw_+} \\
&\approx \frac{q^2}{2}(w_-^2 - w_+^2) + \frac{q^2}{3}(w_-^3 - w_+^3) + \cdots
\end{aligned}
$$
(7.36)

is the "structure factor" for the force dipole calculated in Refs. [7.5, 7.11]. Here we take into account only the first quadratic term in q and approximate as $f\Omega(\boldsymbol{q}) \approx -Pwq^2$, where $w = w_+ + w_-$ is the size of the pump and $P = f(w_+^2 - w_-^2)/2w$ represents the force dipole energy.

The calculation of the membrane MSD closely follows that of the previous section. In the small coupling limit of $\kappa\bar{H}^2/\chi_0^{-1} \ll 1$, we obtain

$$
\phi(s) \approx \frac{2}{3^{3/2}} \frac{k_B T_{\text{eff}}}{D\kappa} \left(\frac{\kappa}{4G(s)}\right)^{4/3} \frac{1}{\hat{s}} \left[1 + \frac{3^{3/2}}{2\pi} \frac{\kappa\bar{H}^2 I(\hat{s})}{\chi_0^{-1}} \left(1 + \frac{Pw}{\kappa\bar{H}}\right)\right],
$$
(7.37)

where T_{eff} is the effective temperature defined by

$$
T_{\text{eff}} = T\left(1 - \frac{\kappa\bar{H}Pw}{\kappa_{\text{eff}}\chi_0^{-1}}\right).
$$
(7.38)

This effective temperature decreases when $\bar{H}P > 0$, while it increases when $\bar{H}P < 0$ [7.25]. The other difference between Eqs. (7.22) and (7.37) is that the second term in Eq. (7.37) has an additional correction due to the pumps. Notice that these non-equilibrium contributions vanish when $w_+ = w_-$, implying that an asymmetry in the positions of the force centers ($w_+ \neq w_-$) is necessary for finite active forces.

140

Nevertheless, since the s-dependence is the same between Eqs. (7.22) and (7.37), the MSD of membranes containing passive pumps and those containing active pumps exhibit the same scaling behavior. A similar result was also obtained by Lacoste and Lau [7.26] who showed that these two cases lead to a sub-diffusive behavior when membrane permeation is negligible and the surrounding fluid is purely viscous. For highly permeable membranes, on the other hand, a super-diffusive behavior was predicted by Granek and Pierrat [7.27] for membranes described by the PB model, and later by Lacoste and Lau [7.26] for those represented by the RTP model. Hence the permeability is crucial for the membrane dynamics, whereas the stochastic nature of the pumps could also lead to short time super-diffusion, as discussed before [7.8, 7.26–7.28]. The latter effect in the presence of viscoelastic media will be discussed in a separate publication. We also note that the effective temperature in Eq. (7.38) is different from that obtained by Manneville *et al.* in Ref. [7.5]. This is because we have calculated Eq. (7.38) from the lowest-oder diffusive terms as in Ref. [7.11], while they neglected these diffusive terms in favor of higher-order terms.

7.6 Summary and discussion

In this paper, we have discuss the dynamics of two-component fluid membranes that are surrounded by viscoelastic media. We have assumed that membrane proteins diffuse laterally and induce a local curvature of the membrane. We obtained the MSD of a tagged membrane segment by taking into account the viscoelasticity of the surrounding media. When the elasticity of the surrounding media obeys a power-law behavior, $G \sim (i\omega)^\alpha$, the MSD due to protein diffusion shows a crossover from $t \ln(1/t)$ to $t^{2\alpha/3}$ behaviors. We have also discussed the situation when the proteins generate active non-equilibrium forces. The generalized Einstein relation is further modified by an effective temperature that depends on the force dipole energy. The generalized Einstein relations that we obtained for two-component membranes [see Eqs. (7.22) and (7.37)] are useful to measure the

141

viscoelastic properties of cytoplasm and/or extracellular matrix.

The obtained membrane MSD (in the Laplace domain) can be used to express the response of a membrane to transverse forces when it is surrounded by viscoelastic fluids. Within the linear response theory, one can write

$$h_\omega = \alpha^*(\omega)F_\omega, \qquad (7.39)$$

where h_ω is the Fourier transform of the mean membrane deformation profile under the action of an external point force $F(t)$ at the origin $\boldsymbol{\rho} = 0$, F_ω is the Fourier transform of $F(t)$, and $\alpha^*(\omega) = \alpha'(\omega) + i\alpha''(\omega)$ is the complex response function. In terms of the response function, the FDT can be written as [7.15, 7.16]

$$(h^2)_\omega = \frac{2k_{\rm B}T}{\omega}\alpha''(\omega), \qquad (7.40)$$

where $(h^2)_\omega$ is the power spectral density. Hence the membrane response function can be related to the membrane MSD by

$$\alpha^*(\omega) = \frac{i\omega}{2k_{\rm B}T}\phi^*(\omega), \qquad (7.41)$$

where $\phi^*(\omega)$ is obtained from $\phi(s)$ by substituting $s = i\omega$, i.e., an analytic continuation. Since $\phi^*(\omega) = \phi^*_{\rm mem}(\omega) + \phi^*_{\rm diff}(\omega)$, the mechanical response of two-component membranes differs from that of single-component membranes.

In our future work, we shall consider an active membrane containing proteins with two internal conformational states [7.29, 7.30], and the effects of viscoelasticity of the surrounding media. This can be a natural model for ion channels because they undergo random transitions between "on" and "off" states. The case of two-component membranes in a quasispherical shape (vesicles) [7.31] is also worth considering in order to study the rheology of cells.

Bibliography

[7.1] B. Alberts, A. Johnson, P. Walter, J. Lewis, and M. Raff, *Molecular Biology of the Cell* (Garland Science, New York, 2008).

[7.2] R. Granek, *Soft Matter* **7**, 5281 (2011).

[7.3] D. Lacoste and P. Bassereau, *Liposomes, Lipid Bilayers and Model Membranes: From Basic Research to Application*, edited by G. Pabst, N. Kučerka, M.-P. Nieh, and J. Katsaras (CRC Press, Abington, 2014) p.271.

[7.4] J.-B. Manneville, P. Bassereau, D. Lévy, and J. Prost, *Phys. Rev. Lett.* **82**, 4356 (1999).

[7.5] J.-B. Manneville, P. Bassereau, S. Ramaswamy, and J. Prost, *Phys. Rev. E* **64**, 021908 (2001).

[7.6] P. Girard, J. Prost, and P. Bassereau, *Phys. Rev. Lett.* **94**, 088102 (2005).

[7.7] M. D. El Alaoui Faris, D. Lacoste, J. Pécréaux, J.-F. Joanny, J. Prost, and P. Bassereau, *Phys. Rev. Lett.* **102**, 038102 (2009).

[7.8] J. Prost and R. Bruinsma, *Europhys. Lett.* **33**, 321 (1996).

[7.9] J. Prost, J.-B. Manneville, and R. Bruinsma, *Eur. Phys. J. B* **1**, 465 (1998).

[7.10] S. Ramaswamy, J. Toner, and J. Prost, *Phys. Rev. Lett.* **84**, 3494 (2000).

[7.11] S. Sankararaman, G. I. Menon, and P. B. S. Kumar, *Phys. Rev. E* **66**, 031914 (2002).

[7.12] S. Leibler, *J. Physique* **47**, 507 (1986).

[7.13] S. Leibler and D. Andelman, *J. Physique* **48**, 2013 (1987).

[7.14] B. Loubet, U. Seifert, and M. A. Lomholt *Phys. Rev. E* **85**, 031913 (2012).

[7.15] R. Kubo, M. Toda, and N. Hashitsume, *Statistical Physics II* (Springer-Verlag, New York, 1991).

[7.16] L. D. Landau, E. M. Lifshitz, and L. P. Pitaevskii, *Statistical Physics* (Pergamon Press, Offord, 1980).

[7.17] S. Ramachandran, S. Komura, K. Seki, and M. Imai, Soft Matter **7**, 1524 (2011).

[7.18] S. Komura, S. Ramachandran, and K. Seki, *EPL* **97**, 68007 (2012).

[7.19] S. Komura, S. Ramachandran, and K. Seki, *Materials* **5**, 1923 (2012).

[7.20] M. Doi and S. F. Edwards, *The Theory of Polymer Dynamics* (Oxford University Press, New York, 1986).

[7.21] F. Gittes, B. Schnurr, P. D. Olmsted, F. C. MacKintosh, and C. F. Schmidt, *Phys. Rev. Lett.* **79**, 3286 (1997).

[7.22] A. G. Zilman and R. Granek, *Phys. Rev. Lett.* **77**, 4788 (1996).

[7.23] A. G. Zilman and R. Granek, *Chem. Phys.* **284**, 195 (2002).

[7.24] In Refs. [7.5, 7.11], the difference between the densities of pumps transferring ions in the up and down direction is denoted by ψ.

[7.25] Our effective temperature differs from that in Ref. [7.11] because the correction term has an opposite sign.

[7.26] D. Lacoste and A. W. C. Lau, *Europhys. Lett.* **70**, 418 (2005).

[7.27] R. Granek and S. Pierrat, *Phys. Rev. Lett.* **83**, 872 (1999).

[7.28] N. Gov, *Phys. Rev. Lett.* **93**, 268104 (2004).

[7.29] H.-Y. Chen, *Phys. Rev. Lett.* **92**, 168101 (2004).

[7.30] H.-Y. Chen and A. S. Mikhailov, *Phys. Rev. E* **81**, 031901 (2010).

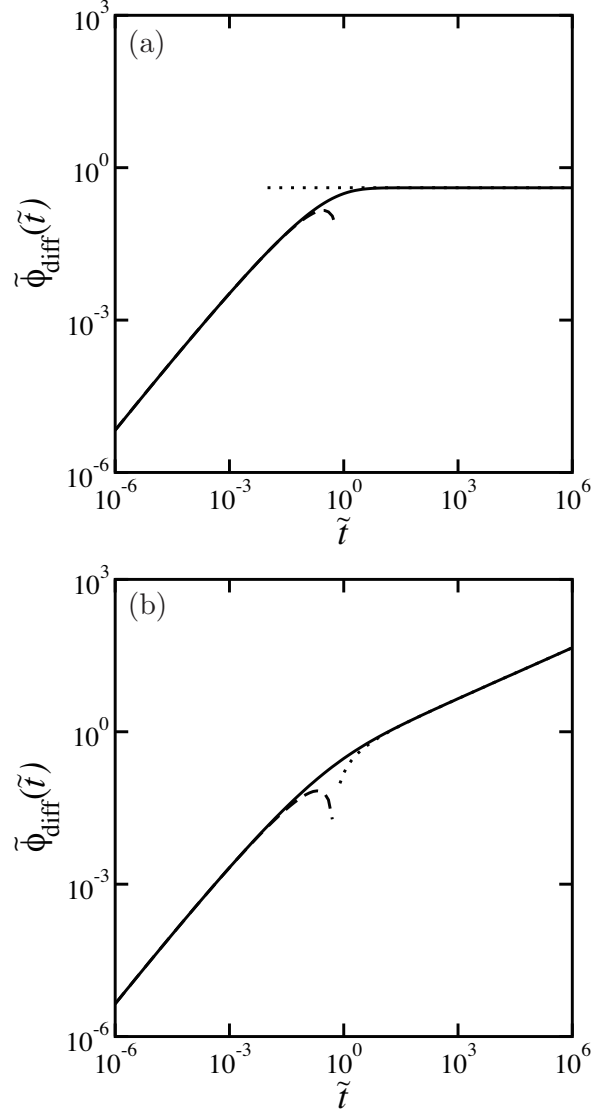[7.31] M. A. Lomholt, *Phys. Rev. E* **73**, 061914 (2006).

Figure 7.3: Dimensionless MSD due to the diffusion as a function of time when (a) $\alpha = 0$ and (b) $\alpha = 1/2$. Here $\tilde{\phi}_{\text{diff}} = \phi_{\text{diff}} / [(k_{\text{B}} T \bar{H}^2 / \pi D \chi_0^{-1})(\kappa/4G_0)^{4/3} \tau^{4\alpha/3-1}]$ and $\tilde{t} = t/\tau = t/(\kappa/4G_0 D^{3/2})^{2/(3-2\alpha)}$. The dotted and the dashed lines are asymptotic expressions given by Eqs. (7.32) and (7.33).
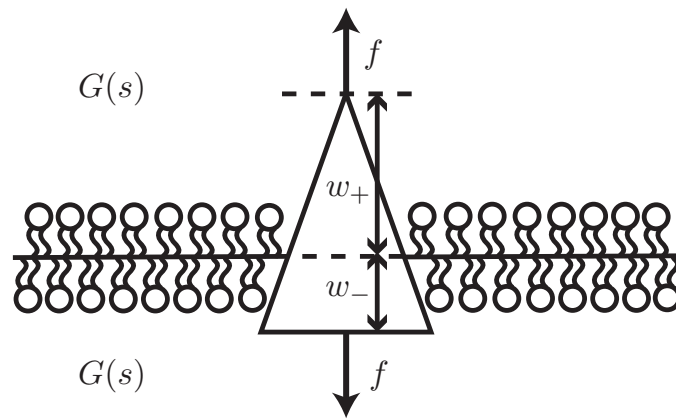
146

Figure 7.4: The asymmetric dipole model for a membrane protein. The force centers are located at distances w_+ and w_- from the bilayer midpoint. The magnitude of the active force is denoted by f. The membrane is surrounded by a viscoelastic medium with a frequency-dependent modulus $G(s)$.

Acknowledgements